Author:
Cole, Jim

Title:
Active Thermal Management in FRP Composites via Embedded Vascular Networks

Active Thermal Management in FRP Composites via Embedded Vascular Networks

James Cole

Department of Aerospace Engineering

University of Bristol

A dissertation submitted to the University of Bristol in accordance with the requirements for award of the degree of Doctor of Philosophy in the Faculty of Engineering

September 2020

Word count: 45909

Abstract

The current temperature limitations of Fibre Reinforced Polymer (FRP) composites may restrict their adoption in future lightweight vehicles. The effects of elevated temperature are complex, depending on the magnitude and duration of thermal exposure. In the short-term, glass transition causes thermo-mechanical performance reductions. In the medium term, the fibre-matrix interface can be irreparably damaged, while long exposures cause thermal ageing which may limit service life. A novel mitigating approach is active cooling of the material by circulating coolant fluid through embedded vascules. The fluid absorbs heat energy from the matrix and transports it to be rejected elsewhere. This novel concept may extend the FRP composite thermal performance envelope and improve service life. Carbon/epoxy specimens were exposed to short- and long-term thermal exposures. At 37 °C below T_g, non-vascular specimens suffered 10 % and 21 % reductions in in-situ flexural modulus and ultimate strength respectively, and after thermal ageing for 120 hours at 47 °C above T_g, they suffered residual flexural strength losses of 86 %. In identical specimens containing basic parallel vascule arrays, using moderate coolant flow rates of ambient temperature air, virgin material performance was almost completely retained in all cases. Surface temperatures were significantly reduced, and physical and chemical signs of thermal damage were both lessened. A finite volume model in MATLAB simulated the thermal performance of arbitrary vascular cooling networks. This was validated with good agreement to experimental specimen temperatures. This was then implemented into a basic genetic algorithm optimiser, demonstrating generation of an optimal design. This project validated the use of vascular cooling with air coolant in FRP composites, demonstrating performance retention in specimens across a range of thermal environments and time scales. It also added valuable evidence of the effects of elevated temperature on carbon/epoxy laminates.

Author's Acknowledgements

The author would like to acknowledge the Engineering and Physical Sciences Research Council (EPSRC) and Rolls-Royce plc for their support of this research through the Bristol Composites Institute (ACCIS) and the Composites University Technology Centre respectively, at the University of Bristol, UK.

The fractography work of Prof. Emile Greenhalgh and Dr. Tomas Katafiasz from the Department of Aeronautics, Imperial College London provided very valuable data in support of this project, for which the author is extremely thankful.

The assistance of Dr Richard Brooker in use of the FTIR-ATR spectroscope lab in the School of Earth Sciences at the University of Bristol, Bristol, UK was greatly appreciated.

Thanks are also due to Mr Ian Chorley and Mr Mike Williams for their time and guidance in the manufacture of composite specimens and machining of custom test fixtures.

Lastly the author is very grateful for the motivation, reassurance and technical advice of his supervisors Prof. Ian Bond and Dr. Andrew Lawrie.

Author’s Declaration

I declare that the work in this dissertation was carried out in accordance with the requirements of the University's *Regulations and Code of Practice for Research Degree Programmes* and that it has not been submitted for any other academic award. Except where indicated by specific reference in the text, the work is the candidate's own work. Work done in collaboration with, or with the assistance of, others, is indicated as such. Any views expressed in the dissertation are those of the author.

SIGNED: JAMES COLE  DATE: 30/09/2020

Table of Contents

List of Figures

List of Tables

Chapter 1: Introduction

1.1 Societal motivation

1.1.1 Proliferation of FRP composites

The 20th century brought technological advances that have transformed our world and the way we live in it. Transportation, communication, medicine and agriculture are just a few of the industries which experienced this rapid development, which continues into the 21st century. In recent decades, however, we have become more aware and concerned with the impact such rapid advancement is having, and will continue to have, upon our planet and its resources.

In 2015, world leaders met to discuss these concerns, and agreed upon 17 Sustainable Development Goals for a better world by 2030 [1]. *Goal 13: Climate Action* recognises the effects human activity is having on our climate, in the forms of rising temperature, changing weather patterns and rising sea levels. Along with other international climate agreements, it calls for action to limit climate change by reducing emissions of greenhouse gases into the atmosphere by burning fossil fuels. *Goal 7: Affordable and Clean Energy* identifies the need for greater adoption of renewable energies, and more efficient use of all energy types, including fossil fuels to reduce waste of finite resources.

The transport sector is both a large consumer of energy and emitter of greenhouse gases. With a growing global population and greater social mobility, the demand for transportation will continue to increase. It is the task of today's engineers, guided by sustainability goals and environmental policies, to develop new, more efficient modes of transportation, and to reduce the impact of existing methods.

The energy required to transport people or goods is proportional to vehicle mass. Thus, one way to make transportation more sustainable is to develop lighter vehicles. In this pursuit, engineers have sought lightweight materials to replace heavier metallic structures. A materials group in use for many decades, but only recently experiencing a surge in utilisation, is Fibre-Reinforced Polymer (FRP) composites. These materials have excellent specific properties; their mechanical performance as a function of their mass. Using these materials, much lighter structures can be designed with equivalent mechanical performance to conventional metallic materials.

This advantage is a result of their hierarchical microstructure; very strong, stiff reinforcement fibres are bundled and embedded in a polymeric matrix. Importantly, the composite material itself and the structural geometry are created simultaneously, as layers of fibres in different orientations can be stacked up and moulded with the matrix to the required shape. This allows a design flexibility that is

not possible with isotropic materials; the distribution and orientations of the reinforcement layers can be tailored to provide the required properties in the direction of applied stress, without extra unnecessary material in other directions, thereby creating a very lightweight, efficient structure.

Today's modern airliners, thanks to a structure comprising around 50 % composite materials, can fly further with a greater payload, while burning less fuel than their predecessors. The automotive sector is following this trend, with the parallel development of electric vehicles placing great importance on weight reduction. Composite materials have also revolutionised the energy sector; the proportion of energy produced by renewable means is ever-increasing, thanks to wind turbines using ever-larger composite blades.

1.1.2 The thermo-mechanical performance problem

In light of all the advancements they have enabled, one could view composite materials as an unparalleled material on which much of our future will depend. However, like all materials, FRP composites have drawbacks and limitations, which will be necessary to understand and overcome to allow their further proliferation. It is a simple fact that current composite materials are unsuited to some applications due to operating conditions outside of their range of capability.

One particularly limiting operating condition is above-ambient temperature. A composite based on a typical aerospace-grade epoxy matrix may be limited to just 150 °C before its mechanical performance begins to decrease markedly, or less if long-term thermal ageing is a concern. The temperature-performance relationship is known as thermo-mechanical performance, and this limitation arises from various physical and chemical mechanisms within the polymer matrix, discussed in Chapter 2.

Compare this to a Titanium alloy, which may be used up to 600 °C, or ceramics which can withstand temperatures over 1,000 °C, and FRP composites suddenly appear rather limited. This explains why certain applications simply cannot make use of them; in modern airliners the non-composite structure remains focused around the gas turbine engines, which experience very high temperatures and are therefore almost exclusively of metallic or ceramic construction.

Expanding the thermo-mechanical performance envelope, even marginally, would offer significant benefits, bringing FRP composites into consideration for a wider range of applications where operating environment currently necessitates different material choices. This would enable further weight reductions and efficiency improvements, helping to alleviate the energy and climate change crises and bringing sustainable development goals a little closer to realisation.

1.1.3 Thermo-mechanical performance improvement technologies

To research and develop means of improving the thermo-mechanical performance of FRP composites, a strategic view of the problem is helpful; the overall aim being an FRP composite component that can operate in elevated temperatures above current limits. This will be the result of various systems-level testing and research. Feeding into this research are enabling technologies, developed through smaller-scale testing and research on different concepts that may achieve this overall aim. There are three main enabling technologies identified that are applicable to this challenge, each with its own avenue of research.

The first is to either adapt the polymer matrix used in the matrix to increase its thermo-mechanical performance, or replace it with a system with improved thermo-mechanical performance. These routes typically incur additional financial cost, manufacturing complexity, or force a compromise with other desirable properties such as toughness.

A second approach is to apply an external coating material that slows the rate of heat transfer between the environment and the component, thereby reducing the temperatures experienced. Application of so-called thermal barrier coatings (TBCs) to FRP composites is not common, however, and will require much further research to address the many issues of adhesion and compatibility.

A third approach, and the one investigated in the present work, is to provide a mechanism to actively lower matrix temperatures to a more acceptable level. This may be achieved via an embedded network of coolant-carrying vessels within the composite laminate. Thermal energy can be extracted from the laminate into the coolant, then transported elsewhere to be rejected, lowering matrix temperatures and extending thermo-mechanical performance. If this concept proves effective, it should be possible to increase the upper operating temperature limit of conventional FRP systems, satisfying the strategic aim and broadening their use in applications that are currently the domain of metals and ceramics.

1.2 Vascular FRP composites and multi-functionality

vascular

(*adj.)* Having the character or properties of a conveying vessel or vessels. From the Latin *vas*, meaning vessel.

A vascular system comprises a network of vessels carrying a fluid, which may perform a wide variety functions. When such a network is embedded in an existing material or structure that performs some other function, it may be classified as multi-functional. Plants and animals rely heavily on multi-functional tissues containing vascular networks to perform functions such as transport of water,

oxygen and nutrients around their anatomy. In mammals, the cardio-vascular system is also utilised to help thermal regulation; blood can very effectively transport heat energy. In hot environments, increased blood flow to the extremities can reject excess heat, and in cold environments this flow can be restricted to conserve heat in the vital organs.

Man-made vascular multi-functionality is much less commonplace, but thermal management is already one of the primary applications. Gas temperatures in modern gas turbines exceed the melting temperature of the nickel super-alloy blades and stators, so they are cooled by air flowing through internal vascules. In expander-cycle rocket engines, cryogenic propellant is circulated through jackets and vascules in the combustion chamber walls and nozzle. This is called regenerative cooling; as well as cooling the engine components, the heated and pressurised fuel can be used to drive turbo-pumps to inject propellant into the combustion chamber.

Multi-functionality can be advantageous in combining multiple functions into one material or structure, adding functionality, reducing weight and increasing packaging efficiency where discrete systems would otherwise be required. FRP composites are prime candidates for multi-functionality, as the final structure is often fabricated directly via lamination of reinforcement layers, permitting the inclusion of secondary materials or systems.

1.3 Research aims

The concept of embedded vascular cooling networks in FRP composites is a relatively novel field of research, receiving attention only in the past five or so years, as of writing. After a brief review of the existing literature, fully discussed in Chapter 2, a number of project aims and objectives were established. These are illustrated in Figure 1.1 and discussed below.

1.3.1 Use of air coolant

Almost all previous studies of this concept have used water as the coolant fluid, due to its favourable thermodynamic properties, as will be expanded on in Chapter 2. There are several factors that would, however, make it less practical in industrial applications, such as its expansion upon freezing and, where electrical isolation may be an issue. The use of air, which avoids these and other drawbacks, has been investigated for its efficacy, but there has been no work at the time of writing on thermo-mechanical performance retention of FRP composites using air as a coolant. Due to the practical benefits of using air, it was deemed an important aim to investigate its suitability further. A specific objective was also set to determine a means to accurately meter the cooling air flow in a vascular arrangement, along with parametric assessment of flow conditions.

1.3.2 Thermo-mechanical performance retention

The second aim was an investigation of vascular cooling and its influence on the elevated temperature mechanical performance of FRP composite materials. Specific objectives were to trial and develop a simple, cost-effective vascular specimen manufacturing method. This should be repeatable and adaptable to any required geometry, and compatible with a range of composite material systems, manufacturing processes and facilities.

Following this would be an exploration of the short-term, in-situ effects of elevated temperature relating to glass transition in a thermo-setting polymer matrix. A test methodology and experimental apparatus to perform simultaneous elevated temperature exposure and mechanical testing were to be developed. The maximum environmental temperature would ideally exceed the glass transition temperature of the material under test, in order to full explore this highly non-linear thermo-mechanical performance regime. The ability of a simple vascular cooling network to lower the specimen temperature and limit any performance degradation would then be assessed at a range of environmental temperatures. The effect of varying basic vascule parameters of diameter, pitch and coolant flow rate would also be investigated at a fixed temperature condition.

Duration of thermal exposure is also of great importance when operating FRP composites at elevated temperatures. While the short-term effects of exceeding T_g were expected to be apparent through macroscopic changes in laminate performance, the less obvious, longer-term micro-scale effects of thermal ageing were no less important to assess. Again, an appropriate test methodology and apparatus would be required to create the correct thermal environment. After ascertaining the effect on non-vascular baseline specimens, the performance retention capabilities offered by vascular cooling could be evaluated via testing of residual mechanical performance.

In both cases, as a precursor, any inherent change in mechanical performance due to embedding of vascules in-situ would need to be characterised. As a vascule represents a relatively large disturbance intentionally created in the laminate architecture, some detrimental influence was expected.

1.3.3 Numerical modelling

In order to more easily assess the performance of different vascular network designs in different component geometries and thermal environments, a simple and versatile numerical model was desirable. As a secondary focus of the overall project, this aim was limited to an accurate and reasonably efficient model of the fluid and thermal aspects of the problem. If time was available, a basic optimiser routine utilising this model would be written to help identify an optimal network topology for a given set of design requirements and constraints.

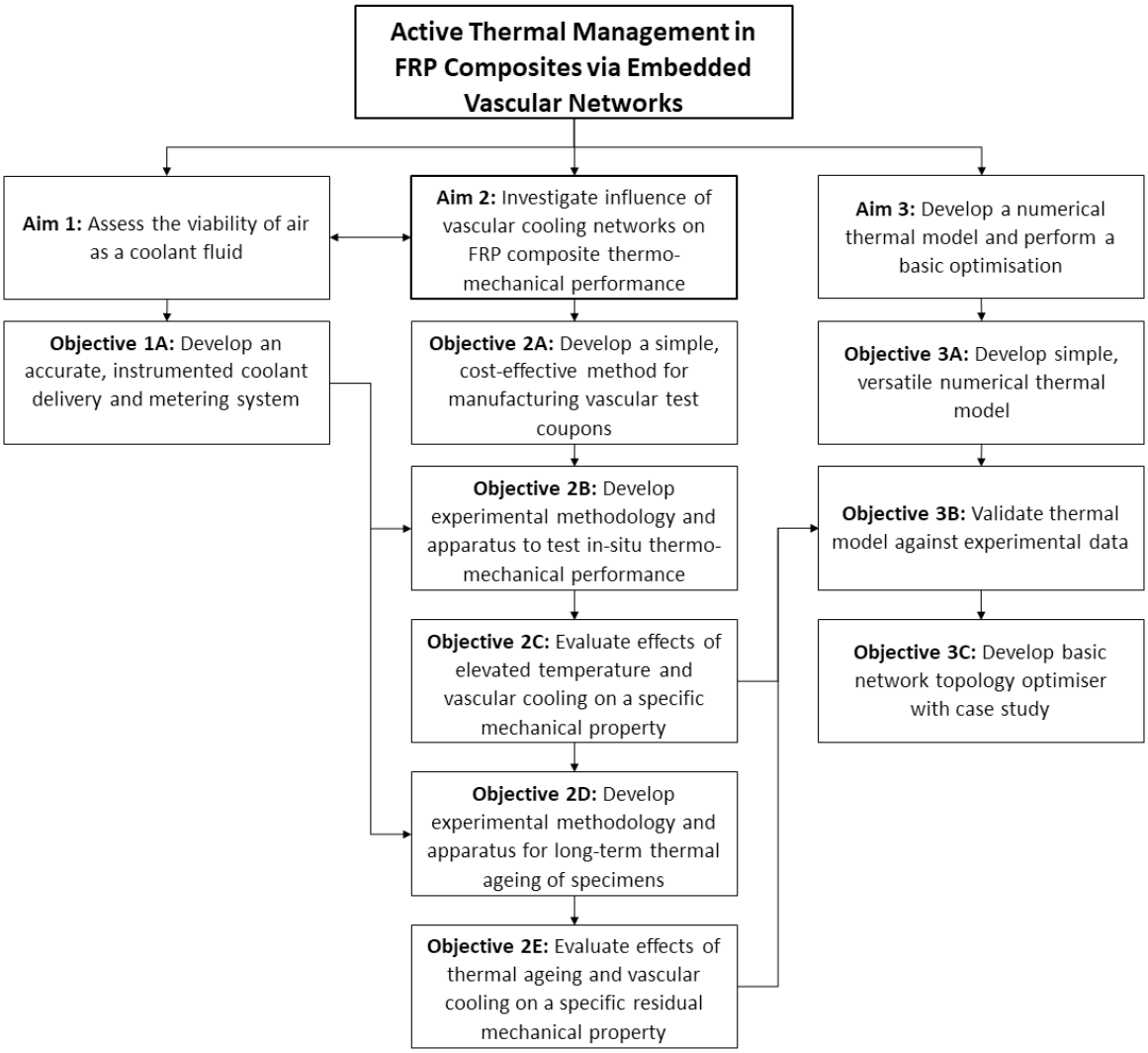

Figure 1.1: Diagram of project aims and objectives. Interdependencies are indicated by arrows.

1.4 Thesis overview

This introduction is followed by a literature survey and review in Chapter 2, discussing the existing and absent understanding within this field, and providing the background knowledge for the present work. This includes the effects of elevated temperature on FRP composite materials, various vascule fabrication methods and the effects of vascules on laminate properties, and finally the thermal and thermo-mechanical performance of FRP composites containing vascular cooling networks.

Chapter 3 covers work on Objectives 1A and 2A-C, establishing the viability of air coolant in retaining in-situ flexural performance under short-term thermal exposures near the matrix T_g. As part of this endeavour a novel method for simultaneously heating the test environment, supplying coolant to the specimen within and performing a mechanical test was developed, and the challenges faced therein may be of interest to the reader wishing to experiment further.

Longer-term thermal ageing is investigated in Chapter 4, tackling Objectives 2D-E by exposing specimens to high levels of heat input for extended periods, assessing vascular cooling performance by testing residual flexural properties at ambient temperature. The relatively new field of incipient heat damage is introduced, and its effects and mitigation explored in detail via a range of physical and chemical analysis techniques.

Chapter 5 concerns the numerical modelling efforts of the project, covering Objectives 3A-C. The development of the thermal model is discussed first, followed by its validation using gathered experimental data. Then the optimisation strategy is discussed, and the case study presented to demonstrate the process.

The project conclusions are then drawn in Chapter 6, followed by proposed avenues of future work to further develop this approach.

Chapter 2: Background and Literature Review

This literature review comprises multiple sections that deal with pertinent previous work related to the studies herein. It begins with an explanation of the effects of temperature on the constituents of fibre reinforced polymer (FRP) composites. It then separates the impact of elevated temperature on FRP composite laminates into short-, medium- and long-term effects based on exposure time. A summary of the current manufacturing methods for creating vascular FRP composites follows, with an exploration of effects of these vascules on laminate performance. Finally, an investigation into the thermal and thermo-mechanical benefits when used for active thermal management will concludes the review.

2.1 Effects of elevated temperature on FRP composites

Many components may be exposed to elevated temperatures for various reasons. Nearby electrical equipment such as batteries or transformers may produce heat through normal operation or faults. Hot fluid may impinge on the material as a design intent or due to failure of ducting or pipework. In space applications, solar radiation, re-entry heating and extra-terrestrial atmospheres are all potential sources of heat. In marine and civil applications, a specified survival time under fire conditions is often required to allow the evacuation of occupants. These are just a few examples of situations in which FRP composites may be exposed to elevated temperatures beyond their usual expected capability.

Temperature and mechanical performance have a close and complex affinity in this class of materials, and good design should always consider both factors; so-called *thermo-mechanical* performance. The magnitude and duration of elevated temperature conditions are important variables (time-temperature dependence); a material may be required to endure moderate exposure continuously, or extreme exposure for a prescribed time before failure. Thermo-mechanical analysis is complicated by the presence of multiple constituent materials, which have very different thermo-mechanical responses. Literature on thermal stability and ageing in polymers is abundant due to their extensive and established uses in many industries, but this Section examines the thermo-mechanical performance of FRP composites across different loading modes, temperatures time scales. The literature cited represents a small proportion of the totality on the topic, and focusses mainly on carbon and glass reinforced epoxies (a thermo-setting polymer), which are popular partly due to their good high-temperature performance and ease of manufacture. For other fibre and matrix combinations, including bismaleimides, polyimides and thermo-plastics such as polyethertherketone (PEEK), a good literature review was performed by Hancox [2].

2.1.1 Thermo-mechanical responses of FRP composite constituents

FRP composites are, by definition, composed of reinforcing fibres contained within a polymer matrix. Commonly employed reinforcement fibres are carbon, glass and aramid. Carbon is most popular in high-performance applications for its superior stiffness, while glass fibres are favoured where cost is a restriction. Carbon fibres retain virtually all of their room-temperature strength up to 500 °C in air, and to at least 1500 °C in an inert atmosphere [3], [4]. Less costly glass fibre has slightly poorer thermo-mechanical performance, but still retains 60 % of its strength at 500 °C [3]. Aramid fibres have the poorest thermo-mechanical performance, but they are typically limited to niche applications due to their very high tensile strength. Even so, they have sufficient performance even at high temperatures for the polymer matrix to be the limiting factor.

There is a wide range of polymers used as matrices in FRP composites, the choice being based properties including mechanical performance, ease of manufacture and cost. All exhibit significant transitions in physical properties at much lower temperatures than the reinforcement fibres discussed above. They also suffer from various mechanisms of thermally-driven physical degradation and chemical decomposition over time. Therefore, the capability of the matrix is the main restriction in high temperature operation of FRP composites.

2.1.2 Short term: stiffness, strength, toughness and failure

The short-term effects of elevated temperature are associated with the immediate thermo-physical transitions that occur as a function of the material's current temperature, and are time-independent. The primary transition in properties for thermo-setting polymers is known as glass transition, and the temperature at which it occurs is the glass transition temperature, T_g. In thermo-plastic polymers the primary transition is melting into the liquid phase at T_{melt}. These are vital characteristics to understand when considering polymers for high temperature applications.

Below T_g, thermo-setting polymers are said to be in a 'glassy' state, and they behave rigidly with acceptable mechanical properties. Many exist in this state at ambient temperatures, and as a matrix they can perform the functions of supporting the reinforcement fibres and transferring loads between them. As temperature increases through T_g, polymers transition to the 'rubbery state', where they become more flexible, and mechanical and interfacial properties are reduced. In this state their suitability as the matrix in a composite material is severely diminished, and any FRP composite operated at or above this temperature will suffer. It is important to note that glass transition actually occurs over a temperature range, and the reported value of T_g can be the upper, lower or mid-point of this range, depending on the method used to measure it.

The mechanism of glass transition is related to the molecular structure, which is composed of linear hydrocarbon-based chains. In a thermoset polymer these molecular chains are chemically bonded to one another, or cross-linked, by covalent bonds. The hydrocarbon chain bonds and cross-links are categorised as primary bonds and have a high dissociation energy (the energy require to break the bond). There are also secondary bonds between chains including hydrogen bonds, dipole interactions and van der Waals forces. Heating increases the freedom of the chains to move, pivot and rotate by breaking the weaker secondary bonds. As T_g is reached, this reaches a critical level and polymer chain mobility increases significantly. Unlike melting this is not a phase change; the polymer remains solid throughout, but exhibits greater flexibility and reduced mechanical properties. This is a reversible process, as cooling through T_g will restore the secondary bonds, reducing polymer chain mobility and restoring mechanical properties. If heating is continued past T_g, decomposition, burning, charring and severe oxidisation will occur as the primary bonds are also broken.

Thermoplastic polymers do not contain cross-links, the only bonding between chains being secondary bonds which are broken at T_{melt}. Above this temperature the polymer exists as a liquid, and cooling through T_{melt} will restore the secondary bonds and the polymer will solidify.

2.1.2.1 Tensile, compressive & shear

Some simplified laminate analyses may assume that properties normal to the fibres are entirely determined by matrix properties, neglecting the fibres. Conversely, fibre-direction properties are entirely determined by the fibre properties, neglecting the matrix. By this assumption, fibre-direction properties ought to be temperature insensitive. In reality, laminate properties in both directions are influenced by the properties and volume fraction of each constituent, and the fibre orientations. The matrix also performs a vital interfacial role in transferring load between fibres and maintaining their arrangement with respect to the load. The reality is therefore more complex, and the matrix cannot be neglected even in fibre-dominated loading modes. Several authors have confirmed that properties in the fibre direction are, in fact, temperature sensitive.

Tensile specimens of glass/epoxy (T_g = 75 °C) were tested by Chowdhury *et al*. [5] from ambient to 200 °C. At T_g, reductions were observed of 23 % and 52 % in tensile modulus and strength respectively, attributed to matrix softening and reduced load sharing between fibres. A transition in failure mode was also noted, from sudden fibre rupture below T_g to longitudinal splitting and more gradual failure at T_g and above.

Tensile tests of single plies of carbon/epoxy (lower bound T_g = 38 °C) were conducted at temperatures from 16 °C to 200 °C by Cao *et al*. [6]. A linear reduction in tensile strength occurred up to 55 °C, beyond which strength plateaued at around 65 % of the 16 °C value. Interestingly, tests

of equivalent dry fibre specimens yielded a much lower residual strength of 48 % compared to the cured carbon/epoxy ply. This demonstrates that, even when well above the T_g, the matrix residual mechanical properties are still contributory to overall laminate performance.

Pultruded samples of glass/polyester (T_g = 110 °C) were tested in tension, compression and shear up to 220 °C by Bai & Keller [7]. Residual in-plane shear strength dropped to 55 % at T_g, and reached a minimum of 13 % at 220 °C, with increasing ductility indicative of matrix softening. Tensile specimens showed a failure mode transition at 100 °C from fibre tensile failure to interlaminar shear near the grips, again indicating matrix property reduction. Below 100 °C the residual tensile strength dropped by less than 18 %. Residual compressive strength of tubular specimens reduced to around 20 % at T_g, and stabilised at just 9 % from 180 °C, with failure by local buckling in all cases. Very similar tests were performed by Correia *et al*. [8], also using glass/polyester material, with near-identical results. Tensile fibre failure occurred at all temperatures due to keeping the test machine grips at ambient temperature, with residual strength reaching around 20 % at 220 °C.

2.1.2.2 Flexure

When FRP composites are loaded in bending, a combination of tensile, compressive and shear stresses are generated. A good understanding of flexural performance of FRP composites is vital for the design of structures such as beams and panels. As elevated temperature can influence performance in all three stress states, it follows that bending performance will also be affected.

The work of Coppola *et al.* [9] on vascular flexural specimens will be discussed later, but their non-vascular control specimens provide relevant data. A sharp drop of 40 % in flexural modulus occurred at the matrix T_g of 152 °C. Residual flexural modulus above T_g was approximately 45 %, and above 275 °C the material was completely degraded. Very similar results were obtained by Kandare *et al.* [10].

Woven carbon, glass and hybrid specimens with epoxy matrix (T_g = 130 °C to 137 °C) were tested in flexure by Rathore *et al*. [11] up to 110 °C. All specimens showed more rapid reductions in flexural strength and modulus at higher temperatures, attributed to a weakened fibre-matrix interface, also evidenced via fractography. Interestingly, the greater the proportion of carbon reinforcement, the sharper the decrease in properties at the higher temperatures, due to the greater CTE mismatch between carbon fibres and the matrix compared with glass fibres. This increased thermal interfacial stresses around the carbon fibres, providing less margin for the interfacial strength and promoting failure.

2.1.2.3 Inter-laminar failure

One primary disadvantage of laminated FRP composites over isotropic materials is their poor through-thickness and inter-laminar performance. Due to lack of reinforcement in this direction, relatively small through-thickness tensile or inter-laminar shear stresses can cause cracks to initiate and propagate between the plies, known as delamination. The susceptibility to this failure mode depends on the ability to absorb strain energy, rather than release it in forming new fracture surfaces. High fracture toughness is desirable to supress crack initiation and propagation, as is stable crack propagation to prevent sudden and catastrophic failure.

Carbon/epoxy specimens (T_g unknown) were tested in pure Mode I (crack opening), Mode II (in-plane shear) and mixed-mode loading by Asp [12]. A 13 % to 24 % increase in Mode I crack initiation strain energy release rate (SERR) between room temperature and 100 °C was observed, depending on the data reduction method. A 15 % to 29 % increase in crack propagation SERR was also found. This was attributed to increased bridging of fibres across the fracture interface, which can be caused by reduced fibre-matrix interfacial properties. In Mode II tests, crack initiation SERR was reduced by 17 % to 21 %, again depending on the calculation method. This result is to be expected as Mode II loading generates in-plane, inter-laminar shear stresses in the matrix, which is weakened by elevated temperature.

Using a novel Asymmetric Cut-Ply (ACP) specimen, Charalambous *et al*. [13] investigated mixed-mode interlaminar fracture toughness (IFT) in Hexcel® HexPly® IM7/8552 carbon/epoxy (T_g ≈ 200 °C). Quasi-static tests at 80 °C revealed a 39 % increase in crack propagation IFT compared to at 20 °C, which was attributed to increased matrix ductility due to the thermoplastic toughening additive. Failure morphology was characterised by cohesive failure of the matrix at all temperatures, indicated by nodules of matrix material and cusp features on the fracture surface when inspected via SEM.

2.1.3 Medium term: incipient heat damage

The process of matrix thermal ageing, which is discussed in Section 2.1.4, is generally considered to be a long-term effect. It typically takes months or years to yield measurable property reductions at moderate elevated temperatures typical of in-service conditions and is often indicated by clear visual signs of degradation. This pre-conception is recently challenged by a relatively new research area is known as ‘incipient heat damage’. Studies have proven that at higher temperatures even short exposures on the order of minutes or hours can permanently degrade the fibre-matrix interface without any visual signs of damage.

The effect on Mode II IFT of exposures of 30 to 60 minutes at 250 °C on specimens of IM7/8552 was assessed by Gaile [14]. Despite considerable scatter, results proved even short exposures to high temperature can cause irreversible, invisible damage to the matrix and fibre-matrix interface. This was evidenced in crack initiation fracture toughness, which was decreased by up to 40.4 %, and in fracture surface morphology, which showed a transition from matrix cohesive failure to fibre-matrix interface adhesive failure after exposure.

Specimens of IM7/8552 were tested well above T_g by Ng *et al*. [15], using temperatures of 343 °C to 454 °C for 30 minutes to simulate jet engine efflux impingement. Physical damage was limited to charring at the lowest temperature, but matrix cracking, delamination and disintegration occurred as temperature increased. Tensile strength reductions of 5 % to 46 % were observed in uni-directional (UD) specimens over the temperature range, while quasi-isotropic (QI) specimens suffered reductions of 46 % to 68 %. This highlights the dependency of thermo-mechanical performance on both constituent behaviour and laminate structure, which is likely to be design-specific.

UD and QI specimens of Cytec Cycom® IM7/977-3 (maximum service temperature = 177 °C) carbon/epoxy were exposed to temperatures from 180 °C to 280 °C for 1 hour by Ong & Wang [16]. Short Beam Shear (SBS) strength dropped by approximately 40 % at 280 °C compared to 25 °C control specimens. Mode I IFT initially reduced in QI specimens, but rose sharply above 230 °C, while UD specimens showed a constant IFT until a sharp increase at the same temperature, due to increased fibre bridging as noted elsewhere. Mode II IFT showed large scatter and no significant trends. As no damage was visible following thermal exposure in any case, matrix decomposition and thermal ageing of the fibre-matrix interface were the proposed causes.

Such high temperatures, especially when reached in such short periods, can cause damage if excessive internal thermal expansion stresses are generated. The coefficient of thermal expansion (CTE) of carbon fibre is very low and negative, at around -0.9×10^{-6} K^{-1}, while the polymer matrix typically has a larger, positive CTE of around 43×10^{-6} K^{-1} [17] (aluminium has a CTE of 24×10^{-6} K^{-1} for comparison). This inhomogeneity can cause complex stress states in multi-directional laminates at elevated temperature, even with no external applied load. The fibres would preferentially contract while the surrounding matrix would preferentially expand, if not for their mechanical bond and constraint from surrounding plies at different orientations. The mismatch is instead absorbed as internal stress at the fibre-matrix and ply-ply interfaces. If stress exceeds the strength of the interface, then fibre de-bonding, matrix micro-crack initiation and propagation will occur that weaken the laminate under subsequent loading, or even directly cause catastrophic delamination.

2.1.4 Long term: thermal ageing

While short-term exposure to elevated temperatures can drastically and immediately affect mechanical performance, longer-term exposure at lower temperature can have subtle, but serious, effects. Due to their time-dependency they are referred to as 'ageing' and may be physical or chemical in nature. Ageing affects the durability and service life of a component, with cost, safety and environmental sustainability implications.

The physical processes of thermal ageing can be categorised as 'degradation' as they have a negative impact on material properties without changes in chemical composition. Mass loss through volatilisation, matrix micro-cracking and visco-elastic effects are all examples, and thermal cycling can induce fatigue damage over time.

The chemical processes of thermal ageing are often referred to as degradation but are better categorised as 'decomposition' as the chemical composition of the polymer is changed. Various reactions can occur when a polymer is exposed to elevated temperatures, depending on the composition and exposure environment. These involve breakdown of the polymer chain molecules, including depolymerisation, chain scission, side-group elimination and oxidation. All are exacerbated by elevated temperature due to increased activation energy and polymer chain mobility.

2.1.4.1 Isothermal ageing

A series of works by Tsotsis *et al*. [18]–[20] exposed specimens of Hexcel® R922-1 and R6376 epoxies, both containing Celion G30-500 12K carbon fibre reinforcement, to 177 °C (above the recommended operational temperature for both systems) for up to 10,000 hours (417 days). Tension, compression, interlaminar fracture and compression after impact (CAI) were tested at several intervals. Physical observations included a brown tinge after 1,000 hours, an increasingly powdery surface texture and matrix micro-cracking on the specimen surfaces, attributed to matrix embrittlement due to post-curing. In general, mechanical properties reduced with ageing duration, with matrix-dominated properties such as ±45° tensile and CAI strengths dropping more rapidly than fibre-dominated properties such as 0° tension and compression strengths. Overall, moduli were found to decrease less rapidly than strengths, due to residual cure increasing resin stiffness in the linear elastic regime before failure occurred. In R922-1 a few properties showed increases with ageing duration, such as 0° tensile strength, which was attributed to initial rapid residual cure increasing matrix stiffness, and possibly reduction in fibre-matrix interfacial strength that reduced local stress concentrations around the fibres. Mode I interlaminar fracture toughness also showed increases with ageing duration in some cases. This was due to extensive fibre bridging between the fracture surfaces, which induces intra-laminar cracking and fibre pull-out that can both absorb strain

energy and increase toughness. Increased fibre pull-out is another indicator of reduced fibre-matrix interfacial strength. It was concluded that the correlations of mechanical properties with mass loss were not sufficiently consistent to make mass loss alone a good indicator of residual mechanical properties. Additionally, large changes in properties occurred with relatively small changes in mass that would be difficult to measure accurately. It was argued that a mass loss merely indicates an unacceptable material choice for that operating condition and cannot provide insight into potential service life estimates.

Long-term thermal exposures of Hexcel® HexPly® IM7/8552 (T_g ≈ 200 °C) and G939/M18-1 (T_g = 196 °C) carbon/epoxy specimens were conducted by Wolfrum *et al*. [21], at temperatures of 180 °C, 190 °C and 200 °C for up to 450 days. Mass loss due to volatilisation of the matrix was measured, and this proceeded rapidly in the first 10 to 20 days in all cases. Slower, linear mass loss behaviour followed, with maximum values of approximately 4 % and 6 % for IM7/8552 and G939/M18-1 respectively after 450 days at 200 °C. Both material systems experienced reductions in tensile, compressive and interlaminar shear strengths with increasing ageing duration. Interestingly, performance reduction as a function of mass loss was temperature insensitive in all cases. Significant separation, or 'brooming', of fibres upon tensile failure was noted in IM7/8552 samples, but not in G939/M18-1 due it its woven fabric construction. In both materials, matrix micro-cracking and delamination following thermal ageing was revealed via Scanning Electron Microscopy (SEM). Fourier Transform Infrared Spectroscopy (FTIR) was conducted to identify changes in chemical composition with ageing temperature and duration. The characteristic spectral bands for these resin systems were determined in [22]–[24]. As ageing duration increased the relative intensity of the epoxy resin component decreased with respect to the thermoplastic hardener, which had a much higher decomposition temperature in both systems. An increase in intensity for oxidation products containing carbonyl groups such as carbonic acids was observed, although less strongly. In IM7/8552 this was accompanied by decreases in peaks related to side groups of the epoxy molecules. These effects were more pronounced with higher temperatures and closer proximity to the specimen surfaces, indicating limited oxygen diffusion from the atmosphere into the specimen bulk. After mechanical testing, fracture surfaces of un-aged specimens showed attached nodules of resin and cusp features on the fibres, indicating good fibre-matrix adhesive strength and matrix cohesive failure. After thermal ageing, fibre surfaces appeared smooth and resin-free, indicating a transition to fibre-matrix interface adhesive failure.

Failure initiation and propagation was investigated further in [25] in tensile specimens of IM7/8552 exposed to the same temperature range for up to 195 days. Matrix micro-cracking was observed very near the surfaces, due to the close contact with the heat and oxygen of the surrounding

atmosphere and increased in concentration with ageing duration and temperature. Cracks were observed to propagate parallel to the fibres, due to the larger thermal expansion in the transverse direction. The presence and growth of these surface ply cracks under tension caused a shift in damage behaviour, as damage in un-aged specimens was initiated by transverse tensile cracking in 90° plies throughout.

A subsequent study by Wolfrum & Eibl [26] performed similar thermal ageing exposures on specimens of IM7/8552, extending the temperature range well above the T_g to 340 °C. As before, mass loss and the relative epoxy/thermoplastic toughener IR intensities were measured, then residual interlaminar shear strength tested. All three metrics decreased with ageing duration, at more and more rapid rates as ageing temperature increased. For example, ILSS reached 60 % of the un-aged value after approximately 30 days at 220 °C, but after just 5 hours at 260 °C. The latter temperature was noted as a threshold above which very rapid degradation of the matrix occurred, leading to delamination and drastically reduced residual mechanical performance. This aligns well with the incipient heat damage findings presented in Section 2.1.3. As before, the extent of thermal decomposition of epoxy was much higher near the specimen surface than in the bulk. An empirical correlation for mass loss, IR intensity ratio and ILSS based on exposure temperature and duration was developed for the range 100 °C to 240 °C and 0.3 to 400 days. Residual ILSS was found to have a linear correlation with IR band intensity ratio, regardless of ageing temperature up to 240 °C. Using these correlations, the authors proposed a method of non-destructively determining thermal history and integrity of a component based on its IR spectrum.

Specimens of Hexcel® HexPly® IM7/8552, HexPly® G939/M18-1, HexFlow® G939/RTM6 and Cycom® IM7/977-3 (all carbon/epoxy) were tested by Eibl [27], using the same ageing temperatures and durations as [26]. Gathered IR spectra and ILSS trends for G939/M18-1 and IM7/977-3, both also thermoplastic toughened pre-pregs, were in agreement with those for IM7/8552 in this and previous studies. As a pure epoxy resin without thermoplastic toughener intended for resin transfer moulding (RTM), the previous IR band intensity comparison was not possible for G939/RTM6, but a change in the ratio of epoxy and oxidation product intensities did indicate decomposition. The lack of toughener in G939/RTM6 also caused a more drastic reduction in ILSS at medium temperatures where the thermoplastic was unaffected in the toughened material systems.

Neat resin samples of a blended epoxy/polyamide system (T_g = 126 °C) were thermally aged at up to 170 °C for up to 120 days by Pei *et al*. [28]. FTIR spectra revealed oxidation of methylene and amine groups to carbonyl-containing compounds such as amide or diphenylketone. Via dynamic mechanical thermal analysis (DMTA) an initial T_g increase was observed at all temperatures, due to

post-cure cross-linking reactions. Below T_g, a gradual decrease in T_g followed, due to chain scission and other thermal decompositions. Above T_g, the original T_g began reducing while a second T_g appeared and increased, reaching 126 °C and 191 °C respectively after 90 days at 150 °C. This phenomenon occurred earlier in the ageing process at higher ageing temperatures. The cause was revealed to be an outer 'skin' of thermo-oxidatively aged material, having a higher T_g due to increased cross-link density. While this study did not involve fibrous reinforcements, it highlights the possibility of misleading results if the laminate surface is assumed to be representative of the entire thickness.

Fatigue tests were conducted on IM7/8552 as part of [13], at 70 % of the quasi-static crack initiation stress and an R = 0.1, lasting for 10^6 cycles at 5 Hz. This exposed specimens to up to 80 °C for around 55 hours, which accelerated interlaminar crack growth rate considerably compared to at 20 °C. Proposed causes were increased matrix ductility, the low influence of matrix toughness on high-cycle fatigue, and decreased matrix yield strength promoting plastic deformation and crack initiation. Fractography of the failure surfaces also revealed smoother fibres and indentations with fewer less attached resin as temperature increased. This indicates that fibre-matrix interfacial adhesive failure was dominant, and the interfacial bond was weakened.

To investigate the mitigation of thermal ageing via embedded vascular cooling networks, Boba [29], [30] thermally aged various specimens (T_g = 126 °C) for extended periods. It was found that, in non-vascular specimens, a decrease in inter-laminar shear strength (ILSS) and an increase in Mode I inter-laminar fracture propagation toughness (G_{IP}) occurred after 2 weeks at 150 °C. When aged at 110 °C, these same property changes occurred after 10 weeks. This was attributed to thermal decomposition-induced T_g reduction over time; once the T_g reduced below the ageing temperature, mechanical performance suffered, and ageing temperature controlled the T_g reduction rate.

2.1.4.2 Thermal cycling & fatigue

Repeated temperature cycling over long periods will generate cyclic thermally-induced stresses via the CTE mismatch mechanism described in Section 2.1.3. Even if these stresses are below the quasi-static material ultimate strength, they may lead to fatigue damage over time, in the same manner as applied cyclic mechanical loading. A wealth of literature on thermal cycling in FRP composites is reviewed by Hancox [31], but common observations are reductions in flexural and transverse tensile properties, which are both affected by inter- or intra-laminar matrix cracking, which was also reported in most studies.

2.1.4.3 Visco-elasticity

Over short periods of time, polymer behaviour can be considered perfectly elastic up to the yield point. However, if stress is applied and maintained for a much longer period, a polymer will exhibit viscoelasticity; a form of physical ageing that is a combination of elastic and viscous behaviour. The viscous portion is due to molecular rearrangement of the polymer chains over time, which dissipates energy as heat.

If a constant stress is applied, a continuous time-dependent deformation will occur beyond the initial elastic deformation. This increasing strain under constant stress is creep, and could eventually lead to rupture if the material stretches too far, or buckling if its shape is altered significantly. If, instead, the strain is held constant the molecular rearrangement will gradually relieve the stress in the material over time. This is stress relaxation, which may lead to unexpected load redistribution in a structure and subsequent failure elsewhere.

These mechanisms are dependent on factors such as temperature, cycle duration and strain rate. Viscoelasticity complicates analysis by yielding different strains for a given applied stress depending on loading rate and direction. This effect can be significant for high-temperature components loaded cyclically over long periods, where dimensional stability is required. FRP composites intended for elevated temperature operation must be designed with viscoelasticity of the matrix in mind, otherwise they may not fulfil the structural and service life requirements placed on them.

Flexural creep tests were performed as part of [11] at up to 20 °C below T_g for 180 minutes. Stress was fixed at 30 MPa, which was around 10 % of the quasi-static strength of the weakest specimen type. Glass/epoxy specimens showed a time-dependent creep strain of 31 % of the total strain, whereas in carbon/epoxy specimens the proportion was 52 %. The difference was attributed to greater CTE mismatch-related fibre debonding in carbon/epoxy.

Tensile and flexural creep tests conducted by Goertzen & Kessler [32] were used to develop a master creep curve for a carbon/epoxy composite (T_g = 82 °C). Long-term predictions at 30 °C and 50 °C yielded a modulus reductions after 50 years of 18 % and 58 % respectively, and stresses required to cause rupture after this period at 84 % and 42 % of the quasi-static ultimate strength respectively.

Tensile and compressive creep rupture of glass/polyester specimens was investigated by Dutta and Hui [33]. Tests temperatures were 25 °C, 50 °C and 80 °C, and although the T_g of the polyester resin used was not stated, this was likely around 95 °C. Results for both tests showed that room temperature specimens could sustain a load of 60 % to 80 % of the room temperature static strength

almost indefinitely. Specimens at elevated temperatures sustained the same load for less than 1 hour.

2.2 Vascular manufacturing methods

A number of methods have been employed to create vascular networks within composite materials. A detailed taxonomy of these is provided in [34], and Table 3 in that work excellently summarises the vascule diameter ranges, advantages and disadvantages of each method. A summary is provided in the following sections for context. Most of the current techniques take advantage of the lamination process, whereby layers of reinforcement fibres, whether uni-directional or woven, are layered progressively to achieve the required stacking sequence. This enables the inclusion of various additional materials between the layers to serve as preforms for a vascular network as desired.

2.2.1 Integration of hollow fibres/tubes

Perhaps the most obvious way to manufacture an FRP composite with an embedded vascular network is to include hollow fibres or tubes in the lamination process. These remain in place during cure and in service, forming a physical barrier between the laminate and fluid. This method has most in common with the biological vascular networks discussed previously, which rely on dedicated wall tissues to support the vascule profile and provide separation between fluid and surrounding tissue.

Two hollow fibre materials have been commonly employed in the literature; glass [35]–[40] and metal [41], [42]. Diameters as low as 5 μm have been produced with glass fibres, while metallic tubes are generally larger. This method produces very smooth internal surfaces, important for fluid flow, and vascule dimensions can be controlled and varied very easily. The fibres also isolate the fluid from the laminate, which can be necessary if they are incompatible. Disadvantages include a limitation on bend radius due to fibre kinking, inability to form branches, and the fibre-laminate interface, which can alter overall mechanical performance.

2.2.2 Manual wire extraction

Another straightforward method, manual wire extraction involves embedding a solid wire or mandrel pre-form into the laminate where the desired network will be. The pre-form is removed manually after cure by pulling on the exposed ends. To make this possible, and to avoid internal laminate damage, there must be no mixing or bonding between the wire material and surrounding laminate. The wire surface energy must be low, yielding a low coefficient of friction to permit extraction by hand. Wires or mandrels used in the literature include silicone [38], [39], coated nylon wire [43], coated metallic wire [41], [42], [44], [45], or insulated metallic wire [29], [46]. A common coating or insulation material for wires is polytetrafluoroethylene (PTFE), due to its low surface

energy and high melting point, enabling it to withstand the cure process of most resins. After the wire is extracted, it leaves behind a void where the vascule boundary is formed by the laminate itself.

Although this leaves no physical barrier between fluid and laminate, it maximises the available diameter for fluid flow by eliminating the vascule wall. It is a very simple and low-cost method, and vascule diameter can be varied easily by using different wire gauges. Curved vascules are possible, although this greatly increases the extraction force required. Disadvantages include an inability to form junctions, the risk of internal damage during wire extraction, and the possibility of wire breakage during extraction, which is likely to ruin the component.

2.2.3 Solder melt

Solder is an alloy of tin and lead that melts at a relatively low temperature, based on the composition. This makes it ideal for making connections in electrical and plumbing work, but it has also been employed as a vascule preform in FRP composite manufacture [47], [48]. A solder is selected with a melt temperature just above the cure temperature, and embedded between layers during the lamination process. The solder wire remains solid during cure, but is then extracted by heating the laminate above the solder melt temperature under vacuum.

This method has the advantage of using low-cost materials, and vascule diameter is easily varied by changing the solder wire diameter. It also does not rely on the tensile strength of the wire to achieve extraction, as with manual wire extraction. Cure pressure has been found to squash the solder wire slightly during cure, forming elliptical vascules. The high-temperature post-cure phase is also a limitation; it takes around 24 hours to extract the molten solder, and during this time the matrix is exposed to temperatures which may accelerate thermal ageing and reduce mechanical properties.

2.2.4 Vaporisation of sacrificial components (VaSC)

This is arguably the most complex method for creating vascular networks within FRP composites, but is very popular in the literature due to its great flexibility [9], [43], [49]–[56]. Fibres of poly-lactic acid (PLA), a thermoplastic derived from biological sources, are treated in a solution of trifluoroethanol, water and tin oxalate for 24 hours. This causes the PLA to de-polymerise at around 200 °C, transitioning straight from a solid to a gaseous state. The fibre can then be manually included between pre-preg layers or woven into a fabric for resin transfer moulding (RTM). It remains solid during cure, but a 24-hour post-cure step at 200 °C under vacuum vaporises the fibres to leave a corresponding network of vascules.

This method is highly versatile as it permits complex branched networks with curves and diameter transitions. Its applicability to the weaving and RTM processes makes it a promising candidate for further development into an automated manufacturing method, which will be required for high-volume production. It currently has limitations, primarily the post-cure vaporisation step that, like the solder melt method, could cause thermal degradation of the matrix material. Conducting this under vacuum limits the opportunity for thermo-oxidative ageing, but as Section 1 discusses, there are other forms of thermal ageing that do not require presence of oxygen.

A novel hybrid method that aims to solve the post-cure thermal exposure issue was developed by Boba [29], [57]. Nichrome wire was coated with PLA by dipping it in a solution containing the thermoplastic. These wires were then embedded to form a vascular network as per the manual wire extraction technique. After cure, the wires were resistively heated to de-polymerise and remove the PLA coating, after which the wires could be extracted manually. Residual PLA was washed out with a solvent. This method removes the need for the lengthy high-temperature exposure of the VaSC method, protecting the matrix from degradation. It does, however, suffer limitations of the manual wire extraction method, such as inability to create branches and risk of wire breakage.

2.3 Impact of vascular networks on host material

The mechanical performance of a composite material has close but complex relationship with the properties and proportions of all constituent materials, their spatial arrangement and any irregularities in properties or laminate structure. Introducing an additional material to the composite in the form of glass, metallic or polymer tubes may require reassessment of the laminate mechanical properties, depending on the tube material properties, orientations and density. The interfacial properties between the tube and matrix will also be important in determining the load distribution around and within the tubes, and their potential to become damage initiation sites. The inclusion of hollow tubes, temporary wires or sacrificial fibres into a laminate will also cause local micro-structure disturbances.

This raises an important issue; the presence of a vascular network may be detrimental to the mechanical performance of the host material or adversely alter its failure behaviour. If the vascular structure no longer meets the original load-bearing requirements it is not fit for purpose, regardless of its multi-functionality. It is vitally important to properly understand the effect that vascules have on stiffness, strength, damage initiation and propagation in all stress states, so that a sound and structurally efficient design can be generated while meeting all original requirements.

2.3.1 Vascule-induced disturbances in laminated FRP composites

While the traditional lamination method of manufacture is not the only method that allows for embedding of vascules (weaving of sacrificial fibres is also possible, for example in [9]), it is the most common in the literature. There are two approaches to embedding the vascule regarding the layers surrounding the vascules. The preform/tube can simply be sandwiched between two layers as desired. This approach maintains the continuity of all layers, though through-thickness disturbances in the form of fibre waviness and lenticular resin pockets can result. The impact of vascule diameter on the characteristics of these disturbances were investigated by Huang [58] and Huang *et al*. [59]. Alternatively, the surrounding layers can be cut to provide a recess of the required shape and path, into which the preform/tube is placed. If the depth of cut matches the vascule diameter, then the plies outside of this zone will lie flat. Layer, and potentially reinforcement fibre, continuity is sacrificed in order to limit through-thickness disturbances, though small resin pockets often still occur. These manufacturing routes were directly compared by Norris *et al*. [45], [48], as illustrated in Figure 2.1.

2.3.2 Effects of vascules on host laminate mechanical performance

As with the effects of elevated temperature discussed in Section 1, a wide range of tests are required to fully characterise the performance of an FRP composite, vascular or not. A recent extensive review of experimental results from the literature is provided by Saeed *et al.* [60], with Table 1 of that work giving an excellent overview. What follows is a summary of the key findings in a range of different loading modes.

2.3.2.1 Tensile & compressive

Kousourakis *et al.* [39], [40] investigated the tensile and compressive performance of carbon/epoxy laminates with sandwiched longitudinal and transverse vascules of various diameters; 0.58 mm to 2.98 mm via silicone mandrels and 0.17 mm to 0.68 mm via hollow glass tubes. Longitudinal vascules had very little effect on tensile or compressive modulus. Very small reductions in tensile and compressive strength were noted, attributed to slightly reduced load-bearing area, and failure mechanisms were identical to non-vascular specimens. Transverse vascules had a larger impact on modulus, and the largest strength reductions were observed with transverse vascules of larger diameters, at around 17 % to 18 % for hollow glass tubes of 0.68 mm diameter. This was caused by reduced load-bearing area, reduced fibre volume fraction due to laminate swelling, and fibre waviness which induced through-thickness stresses that promoted failure. The results were later verified computationally by Nguyen and Orifici [61].

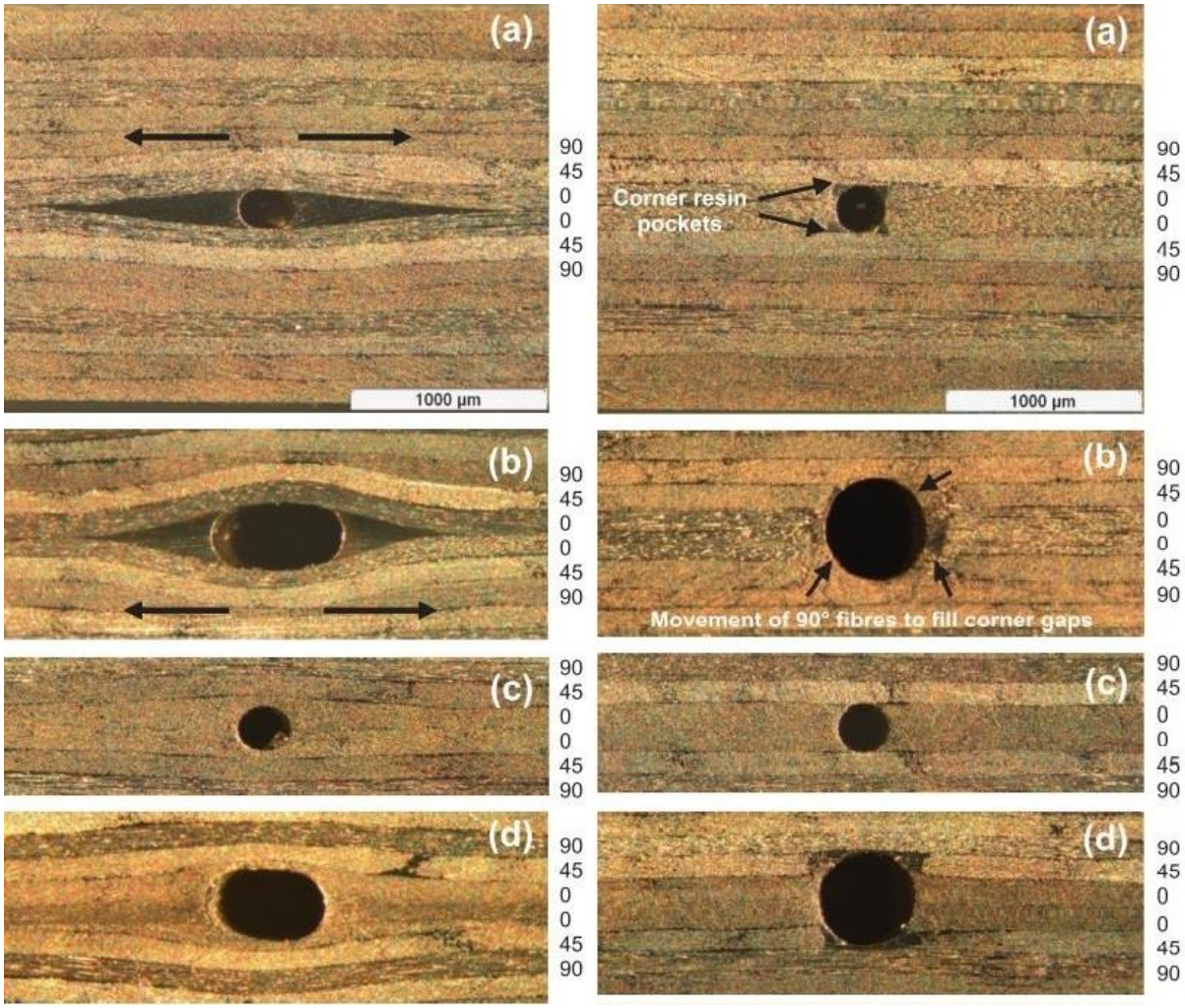

Figure 2.1: Direct comparison of laminate architecture disturbances caused by various vascule embedding configurations. Left column: sandwiching, right column: ply cutting. In each column: a) vascule perpendicular to 1D thickness of surrounding plies. b) vascule perpendicular to 0.5D thickness of surrounding plies. c) vascule parallel to 1D thickness of surrounding plies. d) vascule parallel to 0.5D thickness of surrounding plies. D = vascule diameter. [45,48].

The compressive performance of laminates containing sandwiched vascules transverse to the fibre and loading direction was further investigated by Huang [58] and Huang *et al*. [59]. They found that ultimate compressive strength was reduced by between 13 % and 70 % for vascules between 80 µm and 560 µm in diameter. Failure mode consistently occurred by cracking initiating in the resin pocket, propagating through it and leading to eventual fibre failure via micro-buckling. This was in good agreement with 2D finite element analysis results, when resin fracture toughness was less than the laminate crack initiation fracture toughness. FEA simulations revealed that if the resin were tougher than the laminate, the fibre-matrix interfaces along the resin pocket boundaries would be the crack initiation sites.

Hartl *et al*. [62] computationally studied the combined bi-axial tensile and compressive performance of carbon/epoxy laminates with vascules of 300 µm diameter. Laminates were modelled with vascules running parallel and perpendicular to the surrounding fibres, with the lenticular resin

pocket in the latter case typical of the sandwiching manufacturing method discussed previously. They investigated the influence of three design variables; vascule spacing, vascule aspect ratio (to account for elliptical vascules) and laminate thickness. For uni-axial loading, the greatest performance reductions were experienced when the orientation of the surrounding fibres and the loading direction were both perpendicular to the vascule direction. Loading in the vascule direction, regardless of surrounding fibre orientation, had much less impact. Under combined loading, reductions were similar for all vascule/fibre direction combinations. Elliptical vascules yielded slightly lower stress and modulus reductions compared to circular vascules. Increased channel spacing improved modulus and failure initiation stress reductions but worsened those for ultimate failure. Increasing the laminate thickness had the largest impact of all design variables, decreasing all reduction factors considerably.

In glass/epoxy specimens with straight and wavy vascules created by 3D weaving of VaSC fibres, Coppola *et al.* [63] noted relatively small reductions of < 10 % in tensile and compressive moduli and strength values in both longitudinal and transverse directions. This suggests that, unlike those produced via the 2D ply lamination process, 3D woven FRP composites using the VaSC method may be less sensitive to embedding of vascular networks for multi-functionality, and therefore more applicable to future industrial application of the concept.

2.3.2.2 Flexure

Vascules of 500 µm diameter were created inside woven glass/epoxy specimens by Coppola *et al*. [9] via 3D weaving, with longitudinal vascules placed either at, or offset from, the mid-plane. During control tests it was found that the presence of the vascules in both configurations had no significant impact on flexural modulus during four-point bend tests. Flexural strength was not measured in order to re-use specimens.

Trask *et al*. [64] sandwiched hollow glass fibres containing uncured resin for self-healing purposes into CFRP and GFRP laminates. Glass fibre internal diameter was 40 µm in both cases, but in CFRP laminates they were placed regularly at 70 µm and 200 µm intervals, while in GFRP laminates they were included in a separate 42 gsm epoxy ply. Compared to control specimens, CFRP vascular specimens showed an 8 % and 2 % reduction in flexural strength for each fibre spacing respectively, while the strength of GFRP specimens was reduced by 16 %. Fibre architecture disturbance, resin pockets and reduction in fibre volume fraction were all posed as contributing factors.

2.3.2.3 Interlaminar shear

A linear reduction in inter-laminar shear strength (ILSS) of carbon/epoxy specimens was found with vascule diameter by Kousourakis *et al.* [38], who embedded vascules of 0.4 mm to 1.8 mm via sandwiched silicone mandrels and 0.17 mm to 0.68 mm via sandwiched hollow glass tubes. They proposed a reduction of 1.1 % to 1.8 % for each 0.1 mm increase in vascule diameter.

2.3.2.4 Interlaminar fracture toughness

The discontinuities and additional interfaces introduced by embedded vascules have the potential to influence the crack initiation and propagation behaviour of the material. Understanding this is critical to predicting damage tolerance and fatigue performance when delamination-inducing inter-laminar forces are significant.

Kousourakis *et al.* [38], [40] performed Mode I interlaminar fracture toughness tests on carbon/epoxy DCB specimens containing vascules manufactured by inclusion of hollow glass fibres of 170 µm to 680 µm diameter. Vascules were oriented at 90° to the crack propagation direction, embedded via sandwiching on the mid-plane. The vascule diameter exceeded the thickness of the adjacent 90° plies, causing waviness in surrounding 0° and 90° plies. An increase in fracture toughness was observed with increasing vascule diameter, with toughening mechanisms of crack tip blunting or crack deflection noted depending on whether the crack breached the glass fibres. The occurrence of both of these mechanisms indicates the strain energy release rates of both modes are similar, so neither is energetically preferable. An increase in Mode I fracture toughness of up to 40 % was measured in specimens with the largest vascule diameter.

Uni-directional glass/epoxy specimens were manufactured by Norris *et al*. [45], containing arrays of 500 µm vascules either parallel or perpendicular to the adjacent fibres (which were aligned with the crack propagation direction). Mode I (crack opening) and Mode II (shearing) fracture toughness was investigated with double cantilever beam (DCB) and end-loaded split (ELS) specimens respectively. With vascules oriented parallel to the fibres, either sandwiched or recessed, no significant change in fracture toughness was observed in either mode. Vascules oriented transverse to the fibres, and manufactured by the sandwiching method, caused a large increase in fracture toughness of 160 % in Mode I and 80 % in Mode II. In Mode I, propagating cracks were blunted when they entered a vascule, requiring significantly more energy to form a new crack interface beyond the vascule. In Mode II, the crack path was redirected to a new interface by the tough resin pocket. When transverse vascules were manufactured by recessing the surrounding plies, the toughening was much less at 32 % and 6 % for Mode I and Mode II respectively. In both cases the toughening mechanism was crack blunting. While toughness was increased by all transverse vascules, the

delamination behaviour was worsened. Crack propagation in control specimens was stable and predictable, which is conducive to progressive, non-catastrophic failure. Delamination between vascules occurred unstably in rapid bursts, even traversing several vascules before being arrested in a so-called 'un-zipping' fashion. This unpredictable and potentially catastrophic failure mechanism is highly undesirable.

Identical Mode I behaviour was observed by Pierce [42] and Pierce *et al*. [41] in carbon/epoxy DCB specimens with sandwiched metal tubes and wires of 101 µm to 406 µm diameter. No significant difference in fracture toughness was observed between these vascule manufacturing methods. With 90° transverse vascules, they found that increased vascule diameter increased the measured fracture toughness by between 58 % and 180 % over samples with 0° aligned vascules. Toughening mechanisms were crack tip blunting and crack deflection, with unstable crack propagation as in [45]. In addition, they tested specimens with vascules at 45° to the surrounding fibres and crack propagation direction. These resulted in similar laminate architecture disturbances and resin pockets as 90° transverse vascules, but crack propagation behaviour was different. As the crack front spanned several vascules at any instant, parts of it were blunted while others were not. This produced a less saw-tooth shaped load-deflection curve, suggesting more stable crack propagation.

2.3.2.5 Fatigue

Kousourakis *et al.* performed cyclic tensile and compressive loading of specimens containing transverse vascules as part of [40], at 5 Hz and R = 0.6. After 10^6 cycles the residual strengths were found to be within 10 % of the non-vascular control specimens.

Glass/epoxy specimens containing a single 0.58 mm diameter vascule were manufactured by Luterbacher *et al.* [65], via embedding of a PTFE-coated nichrome wire into a cut recess. No change in tensile fatigue strength was reported at 4 Hz and R = 0.1, over 10^5 cycles.

2.3.2.6 Impact tolerance & energy absorption

In investigating the use of embedded vascules for self-healing applications, Trask and Bond [47] and Norris *et al.* [48] measured the compression after impact (CAI) strength of carbon/epoxy specimens. In [47], vascules were fabricated via sandwiching of 0.25 mm solder wires between the central plies, at 0°, 45° and 90° to the local fibre direction and loading axis, and at 10 mm pitch. Vascules parallel to the local fibre direction and applied load yielded little to no measurable influence on compressive strength in undamaged specimens. In undamaged specimens, transverse vascule reduced the compressive strength by 12 %.

In [48], the same stacking sequence and vascule pitch as [47] were used, but vascules were manufactured by both sandwiching and recessing of 0.25 mm and 0.5 mm solder wires at the centreline. Again, aligned vascules did not significantly affect compressive strength in undamaged specimens. For transverse vascules, a 30 % reduction in strength was observed using the sandwiching method, due to induced ply waviness and resin pockets. The recessing method also yielded a 30 % reduction in strength, attributed to periodic termination of a portion of the primary load-bearing 0° plies. For specimens damaged by a 10 J impact, the same overall trend was observed, but the magnitudes of strength reductions were larger. It was concluded that vascule orientation with respect to the local fibre and loading directions is the most important factor in compressive performance. A small reduction in stiffness was noted even in the configurations that had negligible influence on strength. Parallel vascules created via ply termination required removal of 1 % to 2 % of the primary load-bearing 0° plies, and in some cases termination of off-axis plies at regular intervals, leading to compressive stiffness reductions of 6 % to 16 %. When vascules were oriented transversely, the periodic termination of plies caused reductions of 9 % to 18 %.

As part of [38], Kousourakis *et al.* exposed specimens to impacts of 21 J. Ultrasonic inspection revealed that the larger vascule diameters restricted damage propagation in a direction normal to their direction due to crack tip blunting. This resulted in elliptical damage zones, as crack propagation parallel to the vascules remained unrestricted.

Specimens of carbon/epoxy containing 40 µm hollow glass tubes aligned with the loading direction, and sandwiched at various ply interfaces and pitches, were manufactured by Williams *et al.* [66] for self-healing. The presence of the vascules, despite causing transverse fibre waviness, did not have any measurable influence on compressive strength compared to non-vascular specimens before impact damage.

Corrugated panels of carbon/epoxy containing vascules embedded via sandwiching and the VaSC process were fabricated by Pety *et al.* [54], and crushed in compression. Different stacking sequences yielded longitudinal and transverse vascules parallel to the surrounding fibres, and longitudinal vascules perpendicular to the surrounding fibres. 400 µm diameter circular channels were spaced by 10 mm, while 430 µm × 330 µm oval channels were spaced by 1.2 mm. Good fibre packing and vascule dimensional stability was observed around vascules aligned with surrounding fibres. Vascules perpendicular to surrounding fibres created the typical lenticular resin pockets seen by other authors, being discrete at 10 mm spacing but continuous at 1.2 mm spacing, and vascule profiles were significantly ‘squashed’ in both cases. Compared to non-vascular control specimens, vascules transverse to the loading direction did not significantly change the failure mode or reduce

energy absorption in any cases, though vascules were noted as crack initiation sites due to stress concentrations. For specimens with longitudinal vascules misaligned with the surrounding fibres, failure mode and energy absorbed were not significantly changed at 10 mm spacing, while the continuous resin pocket at 1.2 mm spacing led to increased splaying and 10 % reduced energy absorption. As vascules aligned with both the load and surrounding fibres caused little disturbance to the laminate architecture, failure mode and energy absorption were not significantly changed in this specimen configuration. This indicated that vascular, multi-functional FRP composites would not be compromised in crashworthiness, which is particularly important for vehicle occupant safety and containment structures. Flat vascular panels had vastly improved energy absorption compared to non-vascular panels without a chamfered failure trigger, as the disturbed load path initiated crushing damage before buckling could occur.

2.4 Active thermal management via embedded vascular cooling networks

As discussed in Chapter 1, vascular cooling networks embedded in FRP composites offer one approach to addressing the thermal performance restrictions of this material group. This multi-functional concept is still in the research stages of development, at technology readiness level (TRL) 3 to 4 (experimental proof of concept and lab validation). The body of research on thermal performance of vascular FRP composites is small, and the sub-set that consider the thermo-mechanical benefits even smaller. This section reviews the current experimental and modelling efforts, their findings, and the remaining gaps in the understanding that require further research.

2.4.1 Thermal performance

A number of authors have studied the thermal performance of embedded vascular networks in FRP composites.

Panels of carbon/epoxy and glass/epoxy containing 800 µm diameter straight and branched four-vascule arrays were manufactured by Boba [29]. These were exposed to temperatures of 50 °C, 60 °C and 70 °C, with chilled water coolant flowing at 30 $mL \cdot min^{-1}$. The branched design performed marginally better in glass/epoxy, with temperature reductions of over 10 °C observed in some conditions after 300 s of coolant flow, compared to < 5 °C for straight vascules. In carbon/epoxy the higher fibre thermal conductivity yielded the best performance even with straight vascules, and reductions of > 15 °C were achieved. A numerical model of the fluid and heat flow processes was built in COMSOL Multiphysics®, with good agreement at 70 °C. Poorer agreement at other conditions was attributed to variations in vascule positioning caused during manufacture, to which point temperature measurement via thermocouples was highly sensitive.

Kozola *et al*. [67] embedded arrays of 12 and 24 vascules in a pure epoxy specimens, with diameters of 410 µm and 200 µm respectively. When placed on a heated substrate at 80 °C, using just 10 $mL \cdot min^{-1}$ total flow of water coolant at 20 °C, temperature reductions of up to 12 °C on the exposed surface and 30 °C mean field were observed. Despite having approximately the same vascule wall surface area, the 24-vascule array achieved a lower steady-state temperature in less time than the 12-vascule array, demonstrating the scale effect of vascule diameter on thermal performance. Compared to a non-vascular specimen, which was cooled purely by natural convection on the exposed face, a 53-fold increase in the overall heat transfer coefficient was noted.

Vascular arrays were embedded in carbon/epoxy panels by Pety [52], [53], who investigated the concept of electric vehicle battery containment/cooling structures. Panels were subjected to 500 $W \cdot m^{-2}$ heat flux, with water/ethylene glycol coolant mix pumped at 21 °C and various flow rates. With six straight vascules of 500 µm diameter and 34.7 mm spacing, average surface temperature was reduced by 19.5 °C at a flow rate of 28.2 $mL \cdot min^{-1}$. Higher flow rates yielded little extra improvement, and cooling efficiency plateaued also. At a fixed heat flux and coolant flow rate, panels with fewer, widely-spaced vascules performed poorer than panels with more, closely-spaced vascules, in line with the findings of [67]. This is due to greater vascule surface area and greater network density, both of which improve heat transfer. Similar experiments were conducted on more complex 2D vascular networks; parallel, bifurcating, serpentine and spiral. Thermal performance was found to be related to the distribution of coolant flow across the panel; the parallel network developed a hotspot where coolant flow was lowest in the centre vascules, an issue solved by the bifurcating design. The serpentine network performed even better due to counter flow in adjacent vascules, while the spiral network had best performance as coolant flowed right around the periphery. However, the serpentine and spiral networks required higher coolant inlet pressure due to their unbranched nature, while more distributed flow in the parallel and branched designs reduced the pressure and pumping power required to achieve a given flow rate.

Pierce [42] produced carbon/epoxy panels with arrays of 24 straight, parallel vascules formed by metal tubes. Panels were tested at 110 °C, and water coolant with an inlet temperature of 40 °C was pumped through the vascules. The maximum tested flow rate of 24 $mL \cdot min^{-1}$ yielded surface temperature reductions of 50 °C, with a heat removal rate of almost 3 $kW \cdot m^{-2}$.

The average surface temperature of woven glass/epoxy specimens was measured by Coppola *et al*. [9], based on thermocouple measurements. Depending on environmental temperature, coolant flow rate and vascule configuration, reductions from the environmental temperature of up to 174 °C were observed. This corresponded to a maximum heat removal rate of 123.8 W, which is significant

given the input pumping power reached a maximum of just 0.21 W. Results were compared to a coupled computational fluid dynamics (CFD) and finite volume numerical model created in ANSYS Fluent, with good agreement.

Hybrid panels of shape memory alloy (SMA) and glass/epoxy (T_g = 152 °C) composite were fabricated by Coppola *et al.* [51], containing 500 µm vascules in both materials created via 3D weaving and VaSC. Heat flux up to 300 kW·m^{-2} was supplied to the SMA side, room temperature water circulated through the vascules, and surface temperatures measured. With the highest vascule density and a total coolant flow of 140 mL·min^{-1}, FRP composite surface temperature was reduced by up to 155 °C at 300 kW·m^{-2} heat flux. The actively cooled panel at this coolant flow rate was comfortably able to maintain sub-T_g temperatures up to 300 kW·m^{-2}, while the un-cooled panel took only 10 kW·m^{-2} before T_g was exceed. A dielectric polyalphaolefin (PAO) oil coolant was also trialled, but cooled much less effectively and required more power to pump.

McElroy *et al.* [46] were the first to investigate the feasibility of air as a coolant fluid rather than water. A carbon/epoxy panel with four individual vascules was tested in a hot airstream. Reductions in surface temperature of between 10 °C and 20 °C were observed at some locations, although the vascule morphology was not optimised and resulted in significant 'hot-spots'. A 2D finite-difference numerical model was also developed, and showed good agreement with the experimental results. It is this initial work that formed the basis of the author's project, and a discussion of the merits of air coolant is found in Section 2.5.

2.4.2 Short-term thermo-mechanical performance retention

While a good understanding and predictive capability of thermal performance is important, the purpose of active cooling is to retain or improve mechanical performance at high operating temperatures. The following studies investigated the thermo-mechanical performance of FRP composites with embedded vascular cooling networks.

The flexural specimens of Coppola *et al*. [9] were tested in four-point bending at temperatures between 175 °C and 325 °C, with measured force and deflection data yielding flexural modulus. Room temperature water was circulated through the vascules at various flow rates. At a coolant flow rate of 160 mL/min the retained flexural modulus was around 95 % at 175 °C (T_g + 23 °C), whereas the non-vascular specimens retained just 45 % modulus. This excellent performance retention continued to 325 °C, with retained modulus of 80 % to 90 % depending on the vascule configuration. At this temperature the control specimens were completely degraded.

Coppola *et al*. [50] also tested the survivability of carbon/epoxy specimens under compressive load and intense heating. The specimens contained arrays of 360 µm diameter vascules with various spacing, through which water at 20 °C was circulated. The time to failure was recorded at a stress of 24 % of the room-temperature strength. Specimens containing vascules survived up to 200 % longer at heat fluxes up to 500 % higher than control specimens. Increased coolant flow and reduced vascule spacing both increased survival time, with the latter having most influence.

2.4.3 Long-term thermal ageing mitigation

A vascular water cooling system in carbon/epoxy specimens (T_g = 126 °C) was developed by Boba *et al.* [29], [30], and ageing at 150 C for 2 weeks (340 hours) was conducted. Mode I interlaminar fracture propagation toughness was maintained at the same level as unaged specimens, and fracture surface analyses were identical, proving that the vascular cooling was sufficient to slow the rate of thermal ageing. The ILSS of cooled specimens remained closer to that of uncooled specimens aged at 110 °C at durations of 170 hours and 340 hours, proving the thermal ageing mitigation capability of the simple vascular network. These findings suggest that extra service life could be gained, or higher operating temperatures tolerated without reducing service life, by using active cooling via vascular networks.

2.5 Coolant fluid

It is clear from the previous Sections that, with the exception of McElroy *et al.* [46] who used air, water has been the coolant fluid of choice in the entire literature on the subject. To understand why, some theoretical understanding of the thermodynamic properties of the two fluids, and the relevant heat transfer processes, is necessary. Derivations of the following equations and further information can be found in [68].

Heat transfer between a solid and fluid medium occurs via convection. This is the transfer of heat energy by the movement of molecules within the fluid, in contrast to conduction within solids which involves transfer of internal energy between stationary atoms. Convection can be split into two mechanisms, the first being a diffusion process due to random Brownian motion within the fluid. The second is advection, caused by large-scale currents in the fluid. Advective convection can occur naturally due to buoyancy forces and changes in density due to heating, or forcefully due to induced fluid flow.

According to Newton's Law of Cooling, the rate of heat transfer from a solid surface, in this case the vascule wall, to the coolant fluid is proportional to the temperature difference between the wall and the fluid:

$$\dot{\boldsymbol{Q}} = \boldsymbol{h} \cdot \boldsymbol{A} \cdot \left(\boldsymbol{T}_{\boldsymbol{fluid}} - \boldsymbol{T}_{\boldsymbol{surface}}\right) \tag{2.1}$$

where $\dot{Q}$ is the rate of heat transfer in W, h is the convective heat transfer coefficient (a function of the flow conditions) in $W \cdot m^{-2} \cdot K^{-1}$, A is the area through which heat is transferred in m^2 and T is temperature in K. Consequently, effective absorption of heat energy from the laminate is dependent on a high heat transfer coefficient, a large surface area (increased vascule density) and a large temperature difference. h is related to the vascule diameter, D, fluid thermal conductivity, k, and a property known as Nusselt number, Nu, via the following equation:

$$\boldsymbol{h} = \frac{\boldsymbol{Nu} \cdot \boldsymbol{k}}{\boldsymbol{D}} \tag{2.2}$$

The value of Nu varies depending on aspects of the flow regime, such as whether it is laminar or turbulent, developing or fully-developed. It is determined by a range of empirical models, some of which are dependent on other fluid parameters such as velocity and viscosity, but for laminar, fully-developed flow in a circular pipe, Nu is constant and equal to 3.66 for uniform heat flux at the wall, and 4.36 for uniform temperature at the wall. This means h is increased by increasing the fluid conductivity and decreasing the vascule diameter. A reduction in A from Equation 1 caused by reducing D would have to be balanced by increasing vascule density, much like the capillary beds found in the extremities of the human body, where heat rejection is most effective.

Another important characteristic of any coolant fluid is its specific heat capacity, which is a measure of the heat energy required to raise the temperature of a unit volume of material by one Kelvin. It is expressed in the following formulas, divided by time to give rates:

$$\dot{\boldsymbol{Q}} = \dot{\boldsymbol{m}} \cdot \boldsymbol{C}_{\boldsymbol{P}} \cdot \Delta \boldsymbol{T} \tag{2.3}$$

$$\dot{\boldsymbol{m}} = \boldsymbol{\rho} \cdot \dot{\boldsymbol{V}} \tag{2.4}$$

where $\dot{Q}$ is the rate of heating in W, $\dot{m}$ is the mass flow rate in $kg \cdot s^{-1}$, C_P is the specific heat capacity at constant pressure in $J \cdot kg^{-1} \cdot K^{-1}$, ΔT is the temperature change in K, ρ is the fluid density in $kg \cdot m^{-3}$, and $\dot{V}$ is the volumetric flow rate in $m^3 \cdot s^{-1}$. Therefore, a coolant fluid with high C_P and ρ, flowing at high $\dot{V}$, will be able to accept more heat energy more rapidly before it nears the temperature of the vascule wall and ΔT tends to zero.

Upon inspection of all the parameters discussed above that are fluid properties, it possible to make a comparison between water and air as coolant fluids, as found in Table 2.1 using data from [68].

Table 2.1: Basic properties of water and air at 300 K and atmospheric pressure.

Property	Units	Water	Air
Thermal conductivity, k	$mW \cdot m^{-1} \cdot K^{-1}$	613	26.3
Specific heat capacity at constant pressure, C_P	$(J \cdot kg^{-1} \cdot K^{-1})$	4179	1007
Density, ρ	$(kg \cdot m^{-3})$	1003	1.161
Dynamic viscosity, μ	$(N \cdot s \cdot m^{2})$	855	18.5

Air, in comparison to water, appears to be a poor coolant fluid. For a given vascule diameter, h will be around 23 times lower due to its lower value of k, limiting the rate of heat transfer from the vascule wall. The heat energy absorbed per Kelvin of temperature rise, at a fixed volumetric flow rate, will be around 3,585 times less due to its drastically lower ρ and C_P. The lower viscosity of air does allow a greater $\dot{V}$ for a given pumping power input, as the pressure drop along a length of pipe in fully-developed laminar flow is given by the Darcy-Weisbach equation:

$$\Delta \boldsymbol{p} = \frac{\boldsymbol{128}}{\boldsymbol{\pi}} \cdot \frac{\boldsymbol{\mu \cdot \dot{V}}}{\boldsymbol{D^4}} \tag{2.5}$$

where Δp is the pressure drop in Pa, μ is the fluid dynamic viscosity in $N \cdot s \cdot m^{-2}$, and L is the vascule length in m. The power, P, required to drive this flow, ignoring pump efficiency, is:

$$\boldsymbol{P} = \boldsymbol{\dot{V}} \cdot \Delta \boldsymbol{p} = \frac{\boldsymbol{128}}{\boldsymbol{\pi}} \cdot \frac{\boldsymbol{\mu \cdot \dot{V}^2 \cdot L}}{\boldsymbol{D^4}} \tag{2.6}$$

As power is proportional to $\dot{V}^2$, however, the increase volumetric flow rate is only by a factor of 6.8, insignificant compared with the drastically lower specific heat capacity. The reduction in $\dot{m}$ due to the density of air being only 2 % of that of water only serves to further increase the huge disparity in cooling performance.

Based on this analysis, any vascular cooling system with constrained available pumping power can never be as effective using air coolant as it would with be water coolant. However, the choice of air makes much more sense when considering the associated system-level benefits. Air is abundantly and naturally available from the Earth's atmosphere, so the opportunity exists to use an open circuit, inducing from and exhausting to the surrounding environment, negating any requirement for storage tanks, re-circulation piping and heat exchangers that would be needed for closed circuit systems using other gases or any liquid coolant. The low density also means the coolant itself would add negligible mass to the system. Liquid coolant circuits must be primed fully to eliminate air bubbles and achieve their full flow and thermal effectiveness, which is not an issue when using air. Air will not freeze in cold climates (though moisture condensation could be an issue) nor boil under high thermal load, eliminating the problems of freeze-thaw damage to the surrounding laminate or bursting due to contained vapour. If a leak does occur, air cannot short-circuit nearby electronic

systems, nor pool in inaccessible areas and create a maintenance burden. Lastly, when un-lined vascules are used, water coolant can easily absorb into the matrix, a process which is accelerated by elevated temperature and causes permanent damage to the matrix. Swelling that could generate damaging internal stresses, exceed dimensional tolerances and constrict internal vascules may also occur. Additional mass and displacement of composite material due to a vascule liner would be necessary to avoid these issues. Contact with air, by comparison, has none of these effects.

2.6 Summary

Clearly thermo-mechanical performance of FRP composites is a complex topic, with temperature and time as important factors. Elevated temperature can instantaneously cause performance reductions in practically all loading modes, with those dominated by the matrix or fibre-matrix interface being most sensitive. Very short exposures can cause permanent incipient heat damage without visual indication, and this phenomenon certainly requires further investigation. Long term thermal ageing causes physical and chemical damage, reducing matrix and fibre-matrix interface dominated properties. Thermal cycling can produce fatigue damage due to the mismatch of CTE between fibre and matrix, which stresses the fibre-matrix interface that is simultaneously weakened by thermal ageing. All of these effects place limits on the operating temperature and service life of FRP composite components.

A whole host of methods for embedding vascules within FRP composite laminates have been employed, ranging from the crude to the complex, and each with its own pros and cons. For simple networks in laboratory specimens, a pre-form pull-out technique is satisfactory. Hollow tubes are more complex but offer a barrier between coolant fluid and laminate. The VaSC process, perhaps combined with 3D weaving, would seem the most industry-ready process, but the high-temperature post-cure exposure poses thermal ageing concerns. The method of integration with the surrounding laminate has been proven very influential in failure initiation and propagation.

Results show that vascules aligned with the surrounding fibres and the primary loading direction have very little impact on mechanical properties, and so this should be the configuration of choice if possible. Vascules oriented off the primary loading axis are more problematic, especially if also misaligned with respect to the surrounding fibres. The laminate architecture disturbances introduced by sandwiched vascules in this configuration have been thoroughly proven to be deleterious, due to the resulting resin pockets. Recessing the vascule may help, but not if continuity of the main load-bearing reinforcement layers is interrupted. Inter- and intra-laminar failure modes are more impacted than fibre-dominated, in-plane failure modes, due to out-of-plane stresses as a

result of vascule-induced defects. As more complex vascular networks will necessitate both configurations, careful design with the full laminate stress state in mind will be vital.

Substantial cooling performance and mechanical property retention has been demonstrated using simple vascular cooling networks within FRP composite specimens. This has implications in extending the operating temperature envelope and service life in harsh thermal environments. Water has been thoroughly proven as a good coolant fluid in terms of thermal performance, but a host of operational, system-level drawbacks mean air may be a better choice in some applications. Air has been tentatively proven to be thermally effective in the short-term, but thermo-mechanical data across a range of time scales is currently not available.

Chapter 3: In-situ thermo-mechanical testing

3.1 Introduction

As discussed in Chapter 2, a primary benefit of embedded vascular cooling networks in FRP composites is the instantaneous reduction in matrix temperatures, and the 'real-time' or in-situ mechanical performance advantages this can bring. Yet despite their positive experimental results, the works of Coppola *et al.* [9], [50] remain the only experimental demonstration at the time of writing, and their results were limited to flexural modulus with no data on strength or failure behaviour. Outside of the thermal performance testing of McElroy *et al.* [46] there currently exists no information on the use of air as a coolant (a discussion of coolant fluid performance is found in Chapter 2). It was, therefore, deemed vital to investigate this topic further, via some form of thermo-mechanical testing. Primary aims were the investigation of strength and failure (part of Aim 2), and to determine the feasibility of air cooling in vascular FRP composites (Aim 1). At the current stage in technological development, a first approximation of the magnitude of performance gains was desirable, with some initial qualitative exploration of the design space through coarse variation of a few design parameters. Based on this initial data, the path of subsequent research and design of further experiments could be informed. It was also expected that valuable design and manufacture experience would be gained and experimental techniques developed, that will be useful to those researching this topic in future.

This chapter addresses Objectives 1A and 2A-C, first explaining the choice vascular specimen manufacturing process, which is common to the following chapters. It then justifies the test methodology and details the development of custom-made experimental equipment required to perform the testing, followed by an outline of the test procedure. Experimental results are presented and discussed, and lastly the conclusions of this phase of work are drawn.

The work presented in this chapter was also presented at the 2019 American Society of Mechanical Engineers (ASME) conference for Smart Materials, Adaptive Structures and Intelligent Systems (SMASIS), and published in the ASME Digital Collection as [69]. Some figures and text in this chapter have been directly copied from that publication.

3.2 Experimental methodology

3.2.1 Test method selection

In order to make meaningful comparisons of the data, it was necessary to decide on a standard test specimen and procedure. The literature reviewed in Chapter 2 clearly indicates that vascules oriented transverse to both the loading and adjacent fibre directions have a particularly detrimental

impact on mechanical performance. The unique damage mechanisms caused by this vascule configuration were beyond the scope of this work, so it was desirable to avoid them to isolate the performance changes due to the cooling influence of the vascular network. Whatever test was chosen, it was decided that vascules should be parallel to the direction of loading, and surrounded by a unidirectional block of plies with a thickness equal to the vascule diameter. In this way, laminate architecture disturbance and resin pocket-induced failure modes should be minimised.

Testing at elevated temperature and supplying cool air to the vascule inlets were added complexities that narrowed the range of suitable test methods. The use of longitudinal vascules placed the inlet and outlet at the specimen ends, eliminating an axial compressive test method. Tensile specimens require end tabs, which adds extra manufacturing stages and creates an issue of accounting for the changes in performance of the adhesive at elevated temperatures. Any method requiring visual monitoring of the specimen during loading would also be impractical, as the test would have to take place in a heated enclosure, and providing a transparent, high-temperature capable window would be challenging. Given these factors, and the benefit of commonality with [9], flexure was chosen as the most suitable test method. It left the specimen ends unobstructed and required no end tabbing. The data to be measured was simple; force measured by the load cell of a typical universal test machine, and deflection measured by a single linear position transducer in contact with the specimen.

Flexure can be conducted in three- or four-point bending, with both supporting the specimen at two locations on support noses. The former applies load centrally through one loading nose, while the latter uses two loading noses inside the support span and symmetrical about the centre point. For FRP composite materials, these methods are standardised in ASTM D7264-15 [70].

3.2.2 Specimen design

To produce valid results and permit meaningful comparisons with potential future phases of experimental testing, a standard specimen design was required. The ASTM standard specimen dimensions stipulated are 13 mm width and 4 mm thickness, with an ideal support span-to-thickness ratio of 32:1 giving a support span of 128 mm, with the specimen length being about 20 % longer. Deviations from these values are acceptable within certain limits, providing these are reported.

The material system selected for the experiments was Hexcel® HexPly® IM7/8552, due to its availability and wealth of characterisation data. This carbon/epoxy system is supplied as a unidirectional pre-preg with a nominal cured ply thickness of 125 µm. To achieve a thickness of 4 mm, 32 plies would be required, eight plies each at 0°, 90°, +45° and -45° to maintain a balanced,

symmetrical and quasi-isotropic layup. To reduce material usage and cost, the specimen thickness was reduced to 3 mm, with six plies in each orientation.

As four-point bending produces a constant bending moment along the load span, this variation was chosen. A smaller support span of 100 mm was selected, due to packaging constraints within the thermal chamber discussed later.

3.2.3 Specimen manufacture

The various manufacturing methods reviewed in Chapter 2 were compared based on the requirements of simplicity, low cost and reliability. Manual wire extraction was deemed most suitable, using polytetrafluoroethylene (PTFE) coated nichrome wire sandwiched between plies during lamination. This method required no extra cutting or processing of the pre-preg plies. The wire was supplied ready to embed, and could be purchased inexpensively with various diameters available. While McElroy *et al.* [46] had good success with removal of 1.1 mm diameter wire from their specimens, Boba [29] experienced wire failures at smaller diameters. Failure rates of 100 % and 17 % were experienced for wire of 0.32 mm and 0.50 mm diameter respectively, during extraction from a 200 mm long laminate.

To meet the requirement of embedding the vascule within a block of plies with the same fibre direction, and with thickness equal to the vascule diameter, a wire of 0.75 mm (6 × 0.125 mm) would be required. Based on the available wire diameters, and the risk of wire failure causing scrappage of large panels of material and delays, it was elected to use larger 1.1 mm wire, as used in [46]. This required a change in stacking sequence, adding two more 0° plies and placing them in a single 8-ply block at the laminate mid-plane, for a stacking sequence of $[(+45,-45,90)_3,0_4]_S$. While the thickness of eight plies didn't quite equate to this wire diameter, adding a further two 0° plies was deemed to excessively reduce the support-span-to-thickness ratio of the specimen. The new nominal thickness was 3.25 mm giving a support-span-to-thickness ratio of 30.8:1, slightly less than the recommendation. While this stacking sequence makes little sense for a practical component under flexural load, with the stiffest and strongest 0° plies so close to the neutral axis, its primary purpose was to prevent vascule-induced defects and performance reductions, and permit valid comparisons when varying parameters such as coolant flow and vascule pitch.

The specimen width was increased to 30 mm, which would provide sufficient width for four straight, parallel vascules at the mid-plane with a pitch of 6 mm, with some margin for lateral deviation of the vascule over the specimen length. This specimen geometry mirrored the mid-plane cooled specimens tested in [9], although the manufacturing method used was different.

As found by previous authors, the PTFE-coated nichrome wire was springy and did not adhere to the uncured pre-preg surface, making it very difficult to position accurately. To create multiple large panels with arrays of wires sandwiched at the mid-plane, a jig was required. Two aluminium bars of 370 mm length were machined and drilled with an array of staggered holes at a 3 mm lateral pitch, which were tapped with an ISO M4 metric thread. Inserts with ISO M4 external and ISO M2 internal thread were inserted, which featured a slot into which the wire could be clamped using an ISO M2 bolt. This is illustrated in Figure 3.1.

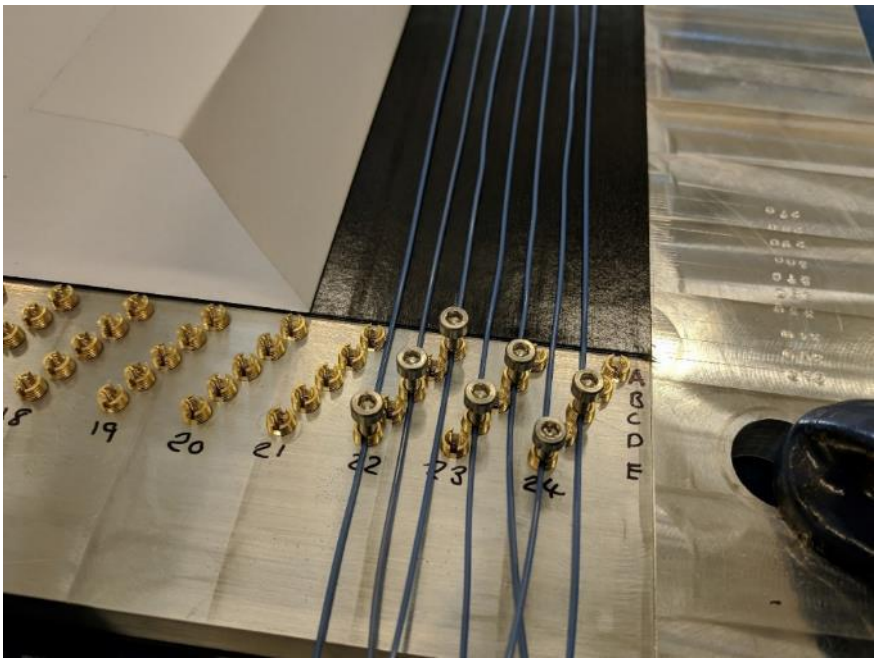

Figure 3.1: Wire placement jig, showing the staggered array of slotted inserts, and wires clamped by M2 bolts across the consolidated lower half of the laminate.

The bars were positioned opposing each other, separated by 300 mm and held parallel with a piece of MDF, and clamped in position. This would accommodate specimens of up to 290 mm finished length (the modification to specimen length is discussed in Section 3.2.4.1), with around 14 to 15 specimens per panel. Wires were cut to leave approximately 100 mm excess each end of the panel. The portion of the laminate below the wire interface, and the four plies above it, were laid up in the standard fashion, consolidating every four plies under vacuum for around ten minutes. The lower portion was placed on the MDF block, which raised its upper surface to the height of the aluminium bars. The wires were placed into the inserts as required and clamped lightly.

Between each group of wires an appropriate gap was left to account for the required specimen width and cutting blade thickness. Once all of the wires were in place, the bolts were tightened sufficiently to hold the wires taught between the inserts, but not too tight as to squash them or

damage the insulation material. The four plies above the wire interface were placed over the wires and aligned with the plies beneath.

An initial consolidation was achieved using silicone sheets covering the laminate, onto which a large aluminium plate was placed. Force was applied by a 22 kg iron weight placed on the aluminium plate. When the plies were well consolidated between the wires, the bolts were removed, and the partial laminate carefully removed from the jig to avoid displacing any of the wires. Further consolidation under vacuum of −28 inHg for at least 30 minutes ensured the wires were well sandwiched. The remaining plies were laid on top to complete the layup according to the stacking sequence. Final consolidation under vacuum for at least one hour completed the process.

Completed laminates were vacuum bagged onto aluminium tool plates via standard practices, using aluminium caul plates on the upper surface to create a flat finish. To create the resin dam, strips of adhesive cork were used on the sides free of protruding wires. Where wires were present, the resin dam was constructed as per Figure 3.2 and Figure 3.3, using layers of cork and vacuum bagging tape to provide a seal, preventing resin flow along the wires that would affect the laminate fibre volume fraction. Multiple layers of breather cloth were placed above and below the excess wire to protect the vacuum bag from puncture.

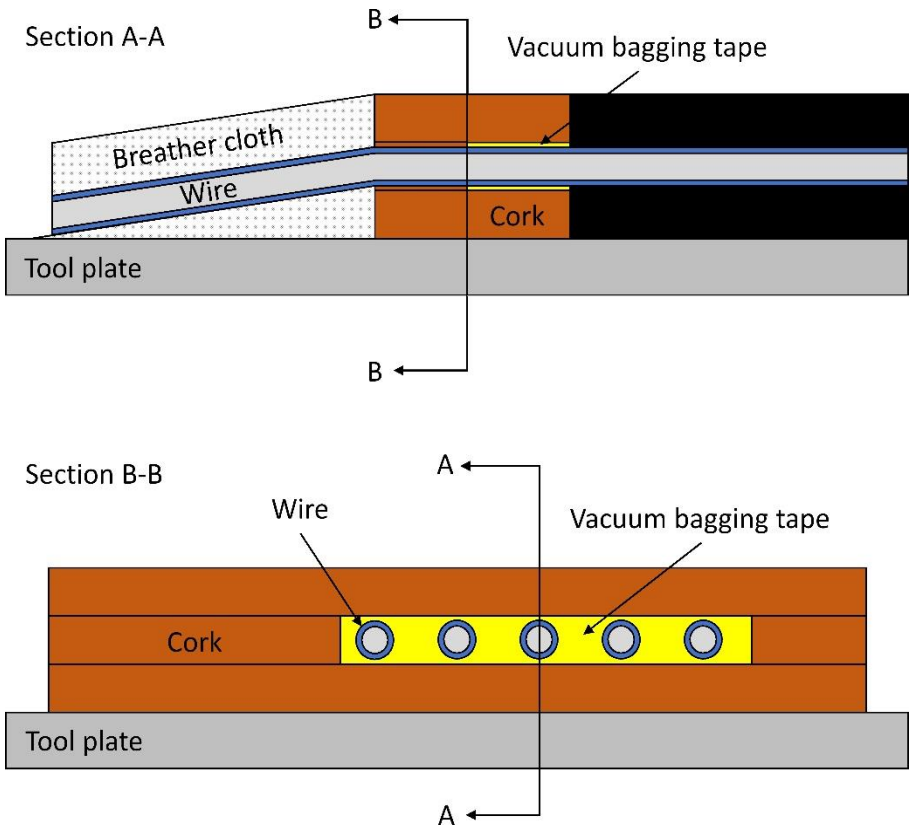

Figure 3.2: Diagram of the resin dam construction where wires protruded from the uncured laminate.

The panels were cured to the manufacturer's recommended curing cycle and de-bagged in the normal way. The layers of cork and vacuum bagging tape adhering to the cured laminate were carefully peeled away with a sharp blade, making sure not to damage the wires. The excess wire was cleaned with acetone to remove debris, and the wires were pulled out manually. One end was clamped and wrapped around a pair of pliers, and drawn straight out with firm, steady pull.

After removing as much remaining tacky tape as possible, the panels were trimmed and cut into specimens using a Compcut automated water-cooled diamond grit saw. The vascules were flushed with water to remove any debris, and the specimens were allowed to dry over at least two days in ambient conditions. Syringe needles were used to provide an interface to connect the air supply tubing to the vascules. 25 mm long Luer-Lok type needles of the appropriate gauge were selected to closely match the nominal outer diameter to the vascules. They were prepared by roughening the steel needle with sandpaper and cleaning with acetone. Araldite® 2015 two-part epoxy was lightly coated on the outside of each needle, taking care not to get any inside, and the needle was pushed into the open vascule end to 10 mm depth. This was repeated for all vascule inlets and outlets on each specimen. The epoxy was allowed to cure for 48 hours, after which the needles were carefully bent outward to separate the plastic Luer-lock connections from each other.

The connections were checked for air-tightness by connecting the air supply tubing, which is discussed later, to the vascule inlets, and a length of outlet tubing to the outlets. The specimen was briefly immersed in water, so that any air leaks would be shown by a stream of bubbles. Leaks were sealed by application of extra epoxy adhesive.

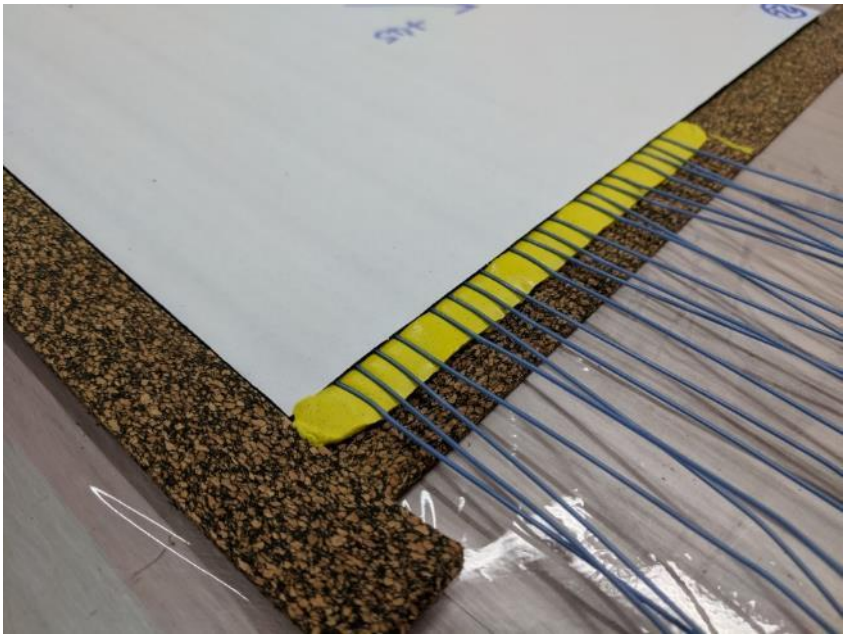

Figure 3.3: Photo of the construction of a resin dam around protruding wires, showing use of vacuum bagging tape.

3.2.4 Thermal chamber development

3.2.4.1 Limitations of traditional thermal test chambers

In the initial phases of the experimental work a thermal chamber attached to a typical universal test machine was trialled. This had the appropriate openings to connect the machine crossheads outside to grips inside, and sufficient internal volume to accommodate most test grips and fixtures. The chamber was heated via an electrical heating element, air was circulated with a fan, and the temperature was maintained at the chosen value by cycling the heater power. This option was attractive as it used existing equipment, provided a consistent and accurate environmental temperature, and could easily achieve temperatures above the dry T_g of IM7/8552 of around 200 °C [71], [72].

However, after performing trial runs, a number of drawbacks were found. The chamber had no side openings, meaning that all of the tubing and wiring had to pass through one of the existing holes alongside the machine crosshead. This was very difficult to set up, and the upward movement of the specimen ends during bending caused the air supply tubing to become strained. Upon reviewing the coolant inlet temperature measured by thermocouples placed in the inlet connections, it was found that the coolant reached the specimen at just a few Kelvin below the environmental temperature.

In practice it was found that the heat absorbed in the supply tubing was sufficient to neutralise almost all of the thermal potential of the coolant to accept further heat energy from the laminate once it entered the vascules. The level of insulation required to sufficiently reduce the heating would be prohibitive given that the tubing must remain flexible.

This issue required a different approach to the chamber, specimen and coolant supply configuration. Instead of transporting the coolant *into* the hot environment, it was proposed to extend the specimen *out of* the hot environment. As the length of excess material outside of the specimen support span was unloaded, it had no effect on the results in flexural tests. Therefore, the design of the specimen length was increased to 280 mm. A bespoke thermal chamber was needed to enclose the central portion of the specimen and achieve the required temperature, while isolating the ends which would protrude into the ambient lab atmosphere. In this way, none of the coolant supply tubing would be exposed to high temperatures, and the coolant should enter the vascules at approximately ambient temperature with more capacity to facilitate heat transfer internally.

3.2.4.2 Custom thermal chamber design and fabrication

The thermal chamber design began by setting out a number of requirements:

1. The chamber must be constructed of materials able to withstand the temperatures required for testing, which may reach 200°C to 250°C.
2. The chamber must provide sufficient internal volume to contain the four-point bend fixture.
3. The chamber must have openings to allow the protrusion and upward movement of the specimen ends, and these openings must provide a good seal to prevent leakage of hot air.
4. The chamber must have an upper opening to allow the test machine crosshead or grip to pass inside the hot environment to carry the upper fixture.
5. The chamber must have additional openings to accommodate wiring for various sensors.
6. The chamber and fixture must interface with existing test machine fittings.

A thick aluminium plate was machined to 300 mm by 300 mm, and holes drilled to match the circular bolt hole pattern of an existing test machine platen. Locating studs were placed around the perimeter. A galvanised steel tapered square duct was purchased, with a lower opening of 270 mm by 270 mm and an upper opening of 220 mm by 220 mm. This duct had a 15 mm wide flange at both ends, the lower of which was drilled to match the locating studs on the base plate. Square openings in two opposing sides were cut to allow the specimen ends to protrude, with a height and position to allow the upward movement of the ends under flexure. Provisions for hot air inlet and return hoses were added to the side (the heat source is discussed in Section 3.2.6). The duct was coated on each side using aluminium foil-covered mineral wool insulation to reduce exposed surface temperatures and retain heat internally. A diagram of the chamber exterior is given in Figure 3.4.

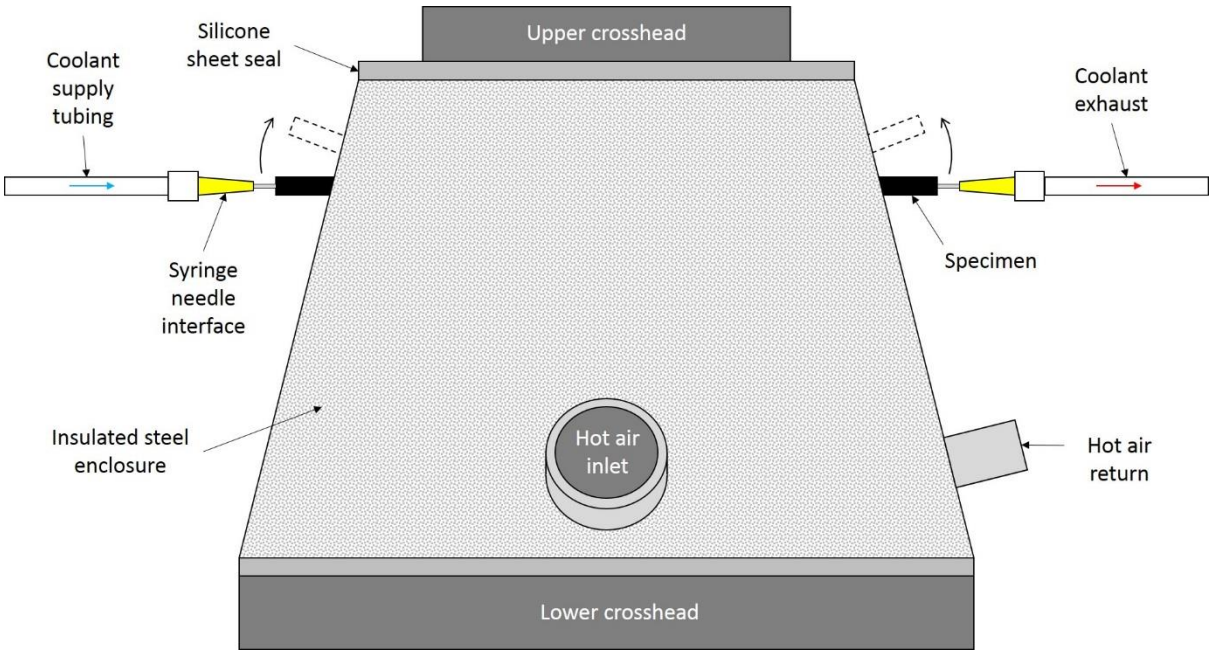

Figure 3.4: Simplified diagram of the thermal chamber exterior. Upward deflection of the specimen ends is shown by dashed outlines.

A custom, adjustable span four-point bend fixture was fabricated from mild steel channel section and plate. Support noses were made from 10 mm diameter silver steel rod. Holes were machined into the web of the channel to align with the bolt pattern in the platen and baseplate. Additional holes provided for cooling air tubing and thermocouple wires.

The lower fixture was supported above the baseplate by a length of aluminium tube, machined to the appropriate length to set the height of the fixture in relation to the slots in the chamber walls. This tube also served as an enclosure to isolate the lower part of the potentiometer from the hot environment, with a fitting for a supply of cooling air. The lower fixture was secured with M16 threaded steel rods fastened into the platen through the baseplate with nuts. Nuts and washers above and below the web of the channel clamped it firmly without applying downward force that would misalign the fixture. A mounting boss was bolted centrally to the channel web, supporting the linear potentiometer at the correct height.

The linear potentiometer was selected as the deflection-measuring device due to its simplicity. It did not require complex calibration or temperature compensation; a 10 V DC excitation potential was applied to the positive and negative leads, and the voltage on the wiper lead monitored by external equipment. The wiper voltage as a proportion of the excitation voltage was linearly proportional to the position of the shaft within its range of movement. The particular model of linear potentiometer used was selected for its measurement range (25 mm), high linearity (< 1 %) and temperature resistance (up to 125 °C). As this was still lower than the target test temperatures, another aluminium enclosure was fitted around the upper part of the potentiometer, again cooled by compressed air, with a hole in the top for the shaft. A steel dome nut on the end of the shaft provided a low-friction point of contact with the underside of the specimen, and was held in light contact with the specimen by a light spring.

The upper fixture was also adjustable and constructed from mild steel blocks. It featured loading noses of 10 mm diameter. A cutaway diagram of the complete fixture within the thermal chamber is given in Figure 3.5.

To provide a flexible seal between the specimen and the slots in the chamber walls, several materials were trialled, including silicone, PTFE mesh and paper, but polyamide vacuum bagging film was most practical. This was cut into rectangular strips, slightly wider than the slots, and significantly longer than their height. A rectangular slot of the same size as the specimen cross-section was cut in the middle of the film. This was attached to the chamber interior with heat-resistant PTFE tape. The excess length was folded in such a way that the small slot could freely move through the height of

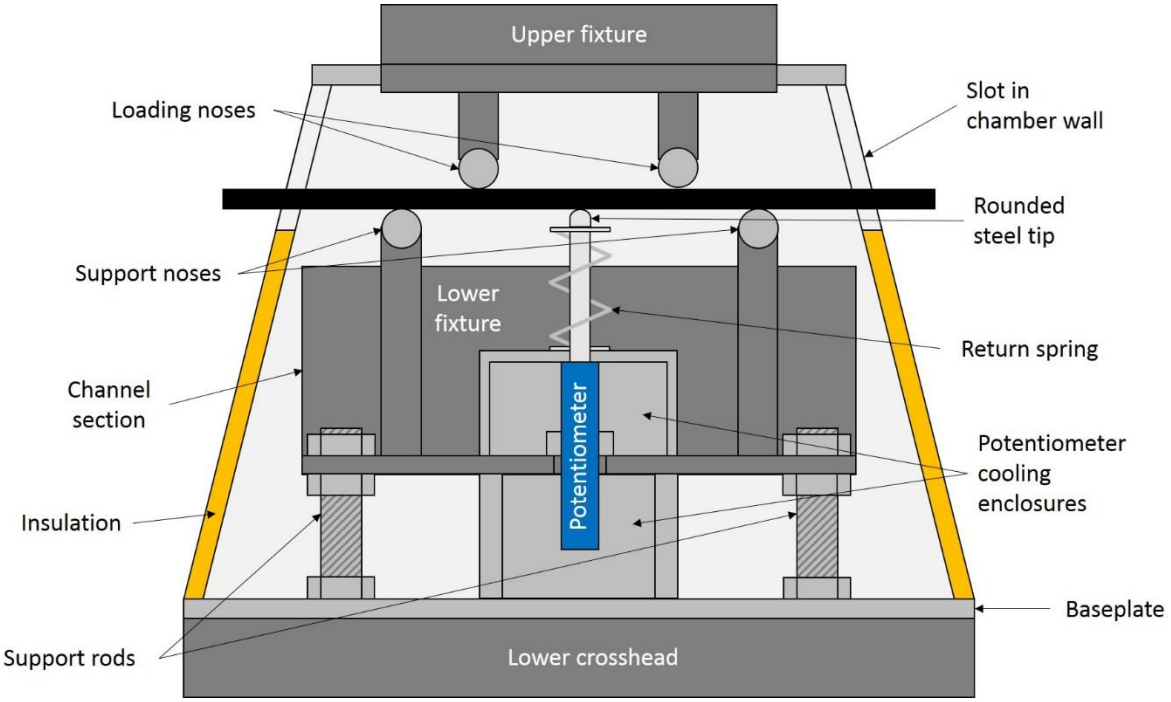

Figure 3.5: Simplified diagram of the thermal chamber interior.

the larger slot in the chamber wall. More PTFE tape was used to fix the sealing film to the specimen. The internal pressure created when the hot air supply was running pushed the film against the chamber interior, forming a good seal that minimised the loss of hot air. The full setup is depicted in Figure 3.6.

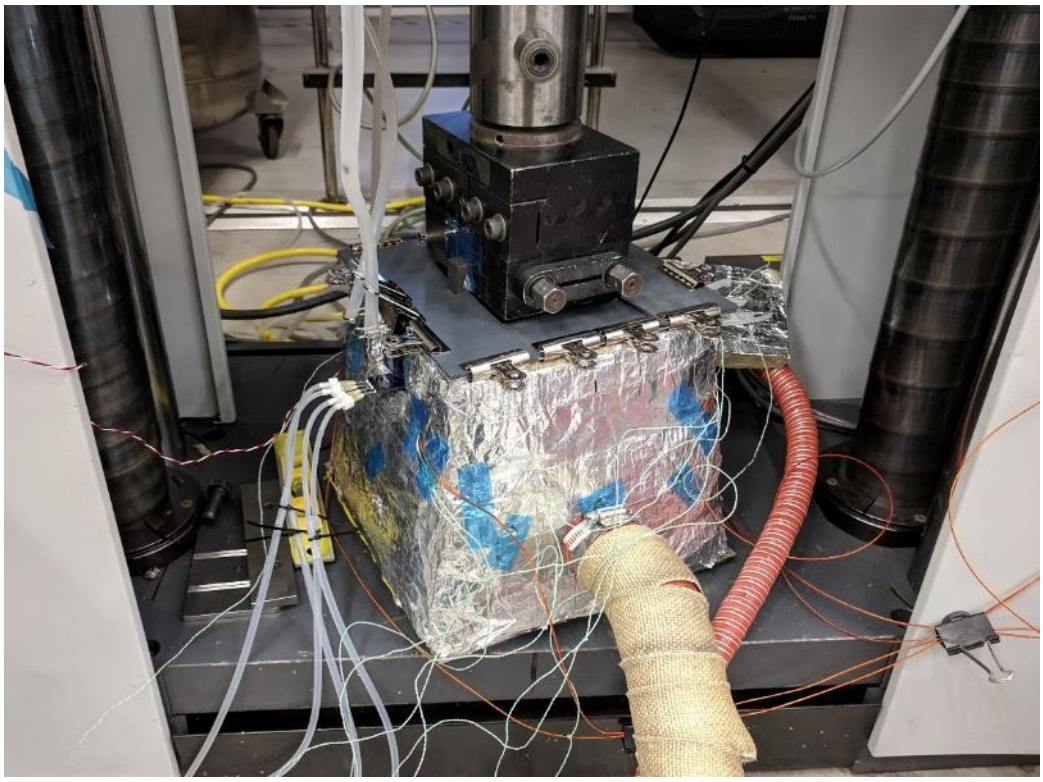

Figure 3.6: Thermal chamber mounted in the test machine, complete with hot air hoses, instrumentation, flexible seals and specimen connected to coolant air supply tubing.

3.2.5 Coolant supply

Coolant was supplied by the compressed air system in the laboratory. This was regulated from the supply pressure to just above 1 bar, and any contaminants removed by a filter. A hose delivered the air to a control and distribution panel, where it first passed through a floating ball type flowmeter measuring between 4 L·min-1 and 50 L·min^{-1}, whose valve provided flow control. This was connected to a distribution manifold, with eight identical hose barb fittings allowing for up to 8 vascules per specimen. An additional port contained an analogue pressure gauge measuring 0.0 bar to 1.0 bar gauge pressure. The apparatus is shown in Figure 3.7.

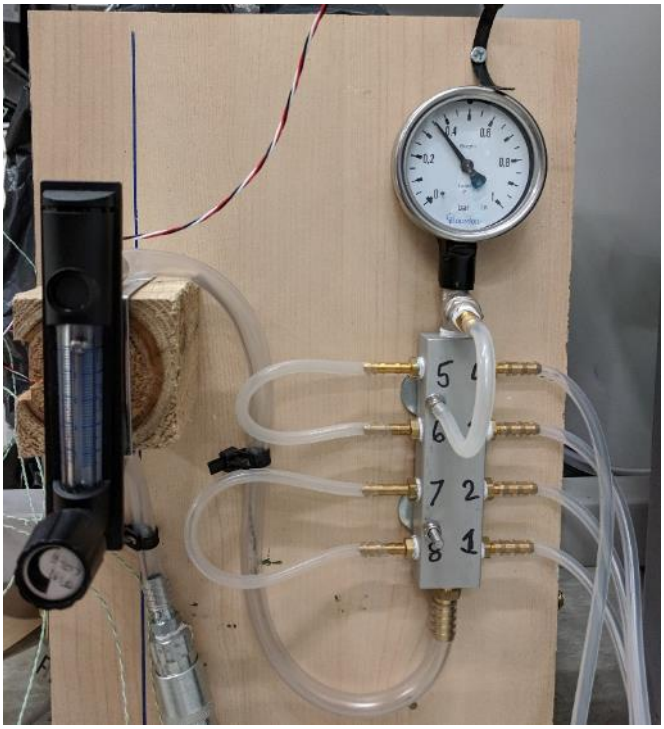

Figure 3.7: Photo of coolant air distribution panel, showing flowmeter, manifold and pressure gauge.

From the hose barb connectors, lengths of silicone tubing were routed toward the thermal chamber, taking care to avoid kinks. These were terminated with hose barb to Luer-Lok adapters. These enabled an airtight connection between the tubing and the hypodermic needles bonded into the vascule inlets, as shown in Figure 3.8. A similar arrangement was used in reverse on the vascule outlets, but only a short length of silicone tubing was used.

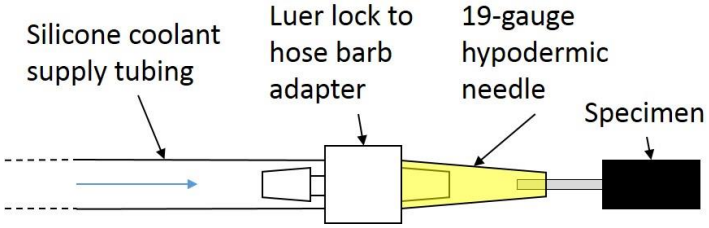

Figure 3.8: Diagram of the coolant supply interface.

3.2.6 Environmental control

A number of heat sources were considered, achieving heat transfer through conduction, convection and radiation. Conductive sources such as electrical heater mats were discounted due to the need for direct contact with the specimen surface by the fixture and potentiometer. While a radiative source such as an infra-red (IR) lamp would not require contact, obstruction by the loading fixture would prevent uniform heat absorption. Convectively heating the specimen by heating the surrounding air was deemed the most practical option, and most relevant for the majority of potential applications where the component would be surrounded by a hot gaseous atmosphere.

Heating the air within the chamber would require extra components to provide heat and circulate the air inside an already restricted space, so an external heat source was sought. Existing equipment in the laboratory included a Heatcon® Composite Systems HCS9200B Dual Zone Hot Bonder and HCS2041-03 Portable Hot Air Curing System, rated at 6000 W and shown in Figure 3.9. This system is designed for the in-situ cure of composite repair patches where complex geometries make electrical heater mats impractical. It passes a supply of high pressure air over an electrical heater element before delivering it via a flexible hose to a diffuser mounted over the part and under a shroud. The single-phase AC, 240 V electrical supply to the HCS2041 is pulsed by the HCS9200B to regulate the temperature in the shroud, using a number of J-type thermocouples to form a feedback loop. A cure cycle comprising numerous ramps and dwells can be programmed into the HCS9200B. Hot air can be

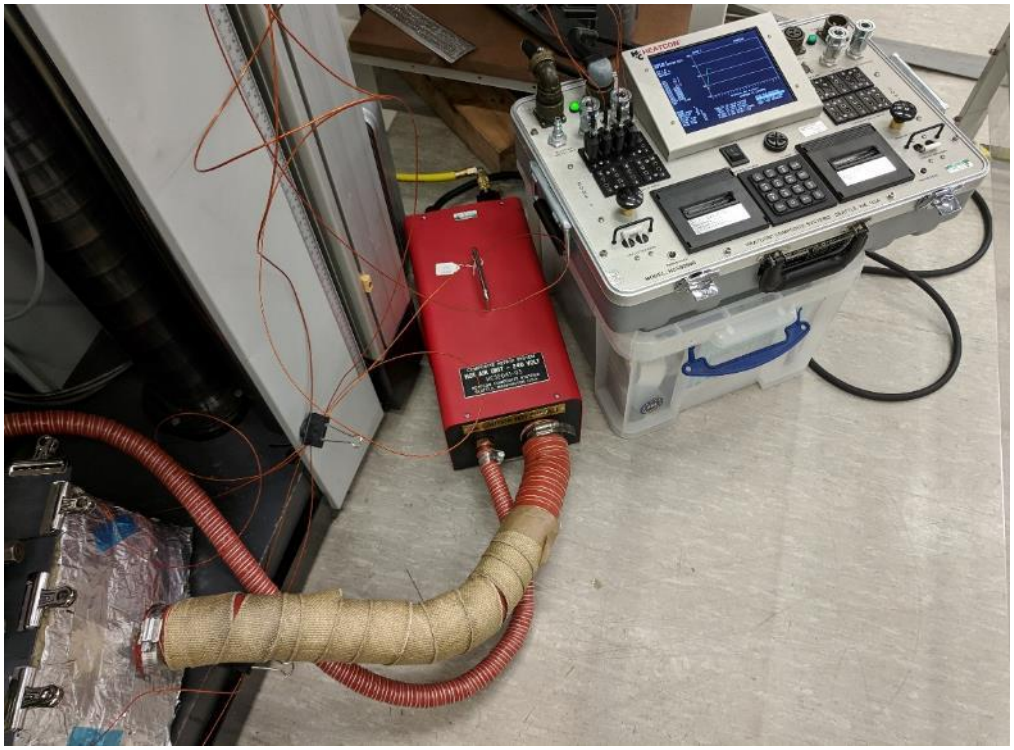

Figure 3.9: Photo of the Heatcon hot bonder and hot air curing systems connected to the thermal chamber.

recirculated from the shroud to the HCS2041 to reduce the power demand. By substituting the diffuser and shroud for the custom thermal chamber, it would be possible to accurately control the air temperature inside the chamber.

3.2.7 Data acquisition

In addition to those in the coolant inlets and outlets, K-type thermocouples were placed on the upper specimen surface, and on the potentiometer body to ensure it was not overheated. These temperatures were monitored and data recorded using an array of Pico® Technology TC-08 data loggers. The potentiometer excitation voltage and output signal monitoring were provided by a Micro-Measurements System 8000 data acquisition system, recording at 10 Hz. This system also recorded the applied load via an analogue output from the test machine load cell, again at 10 Hz.

3.2.8 Flexural test procedure

After recording its dimensions, each specimen was placed into the four-point bend fixture and the flexible seals attached as described. The specimen was positioned symmetrically about, and aligned perpendicular to, the support noses using a square and ruler, ensuring the potentiometer shaft was positioned at the centreline. The upper machine crosshead was lowered to bring the loading noses into contact with the specimen. The deflection and load values on the test machine controller and the data logger were zeroed. Sheets of silicone were placed over the gaps between the test machine grip and the chamber upper opening to create a flexible seal, and secured using metal clips.

The cooling air supply to the potentiometer enclosure was started, as was the flow of air through the vascules. Once all of the data acquisition systems were armed correctly, the hot bonder and hot air supply system were powered up, and its air supply started. A temperature cycle was programmed into the hot bonder to the required temperature. Below 150 °C a 3 °C·min^{-1} ramp rate was used, and after 1-minute dwell at 150 °C this was reduced to 2 °C·min^{-1}. During the ramp all data was monitored, especially the potentiometer temperature to prevent damage. When the final test temperature was reached a long dwell allowed sufficient time for thermal equalisation of the test fixture, which was important due to thermal expansion applying measurable flexure loads and deflections to the specimen. This equalisation took around 10 minutes, after which the mechanical test was started.

As per ASTM D7264-15, the test used displacement control with a crosshead speed of 1.0 mm·min^{-1}. The test was stopped upon the first significant load drop indicating a major failure event, or just before the limit of the potentiometer travel, whichever occurred sooner. Once all of the data was saved successfully, the specimen was unloaded, and the hot bonder cycle was stopped. The cooling air supply was maintained, and a desk fan was directed at the thermal chamber to aid cooling. Once

thermocouples indicated temperatures below 40 °C inside the chamber, the cooling air was shut off, the upper crosshead raised, and the specimen removed and stored for analysis.

Between each test the flexible end seals were replaced as they became brittle after heat exposure. The data acquisition systems were reset, and thermocouples transferred to the next specimen, which was loaded into the fixture and prepared as described.

A total of five or six specimens were tested at most test conditions to obtain a reliable average. Non-vascular specimens were tested first at the ambient lab temperature of 23 °C, 121 °C (the manufacturer's stated maximum service temperature for IM7/8552) and 170 °C, which was the highest temperature attainable with the equipment. While the upper temperature was still 30 °C below the material dry T_g, it does represent operation well above the manufacturer's recommendation, and the T_g at ambient levels of moisture absorption is typically lower. After determining the effect of temperature alone, vascular specimens with no coolant flow were tested at 23 °C and 170 °C to measure any influence on performance of the vascules themselves. Finally, vascular specimens were tested at 170 °C with coolant flowing at a total of 15 $L \cdot min^{-1}$ (0.9 $m^3 \cdot h^{-1}$).

3.3 Experimental results & discussion

3.3.1 Thermo-mechanical properties

Flexural modulus was determined from the slope of the stress-strain curve between 0.2 % and 0.4 % strain, which was well within the linear elastic region for all tests. Ultimate flexural strength was calculated as the peak stress at the specimen surface in the direction of bending under the assumption of beam theory, as per ASTM D7264.

3.3.1.1 Non-vascular specimens

Average flexural modulus of non-vascular specimens at ambient temperature showed good agreement with classical laminate analysis, at 29.9 GPa and 31.0 GPa respectively. Reductions of 4.2 % and 10.2 % were experienced at 121 °C and 170 °C, respectively. This corresponds well with the findings of [9], who observed a 5 % to 10 % reduction in modulus between 50 °C and 30 °C below T_g. This result was as expected, because the strain range over which modulus was calculated fell well within the linear elastic regime. This was below the damage threshold where matrix and fibre-matrix interfacial properties become dominant, and behaviour was dominated by the reinforcement fibre properties. Due to the relative insensitivity of fibre performance to temperatures in the range tested, it was unsurprising that modulus also exhibited low sensitivity to temperature.

Flexural strength experienced a more rapid reduction of 11.4 % at 121 °C and 21.2 % at 170 °C. These reductions are shown in Figure 3.10. Again, this agrees with expectations, as ultimate failure

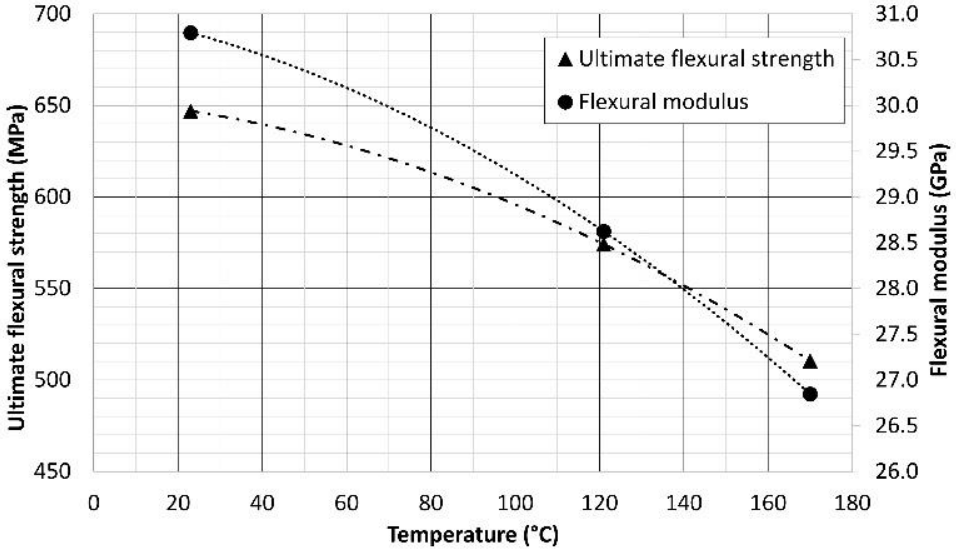

Figure 3.10: Variation of flexural modulus and ultimate flexural strength with temperature in non-vascular specimens.

occurred at higher strains that were in the plastic deformation regime for specimens at elevated temperatures. Here the damage mechanisms dominate the behaviour, and ultimate strength is determined by the most critical failure mode. Damage modes are discussed further in Section 3.3.2, but the critical failure mode in these experiments was matrix and fibre-matrix interface dominated. Given the much greater thermo-mechanical sensitivity of the matrix and fibre-matrix interfaces, it follows that ultimate flexural strength drops more rapidly with increasing temperature than flexural modulus.

These results demonstrate that even at a temperature stated as acceptable for service by the manufacturer, the performance knock-down for this material was significant, and assumption of reported ambient temperature properties would be non-conservative. It was also clear that, despite being around 30 °C below the nominal material dry T_g, at 170 °C the material was approaching the temperature range where glass transition and thermally-induced damage cause properties to decrease non-linearly. Even if conditions reached this temperature only momentarily, failure of the structure may still occur depending on the safety margin of any design.

3.3.1.2 Vascular specimens

Compared with non-vascular specimens, those containing vascules showed an increase in modulus and strength even without coolant flow. At 23 °C these increases were 15.2 % and 5.6 % for modulus and strength, respectively, as detailed in Table 3.1. At 170 °C the increases were more pronounced at 17.6 % and 15.4 %. This artefact was attributed, at least in part, to a feature of the laminate structure introduced by the manufacturing process. Instead of all 0° fibres trapped above and below the embedded wires migrating to the inter-vascule regions during cure, some fibres were trapped,

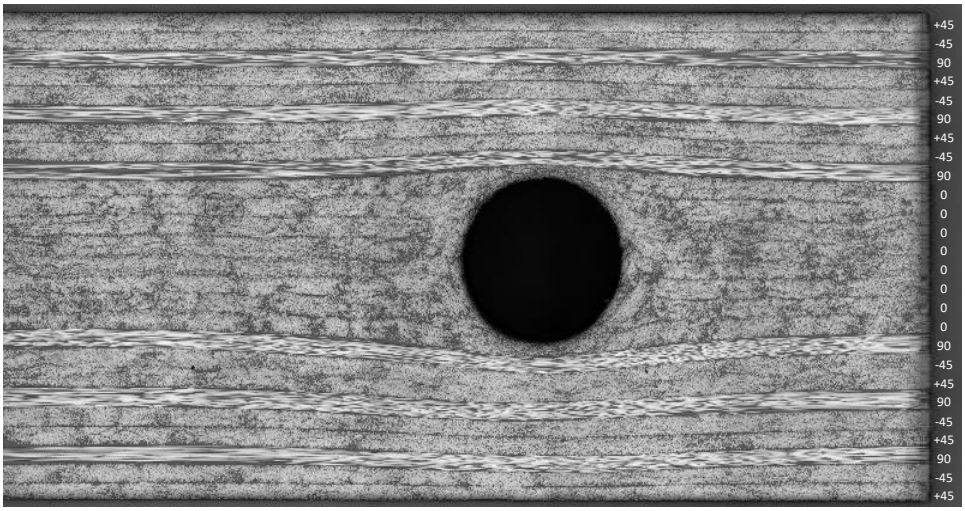

Figure 3.11: Optical micrograph of a cross-section through a vascular specimen, with ply orientations labelled.

as shown in Figure 3.11 and Figure 3.12. This, along with the slightly over-sized wire diameter, meant they were further from the specimen neutral axis than intended. Having high stiffness in the direction of bending stress, these displaced fibres increased the effective specimen second moment of area. This increased flexural modulus and reacted more of the direct bending stress in the stronger 0° plies, relieving some of the transverse stress from the surrounding off-axis plies.

The bands of trapped tows were typically around 90 µm thick each, and displaced by approximately 50 µm due to the larger wire diameter, causing undulations in the interface with the adjacent 90° plies. This resulted in transverse waves in the surrounding off-axis plies throughout the specimen,

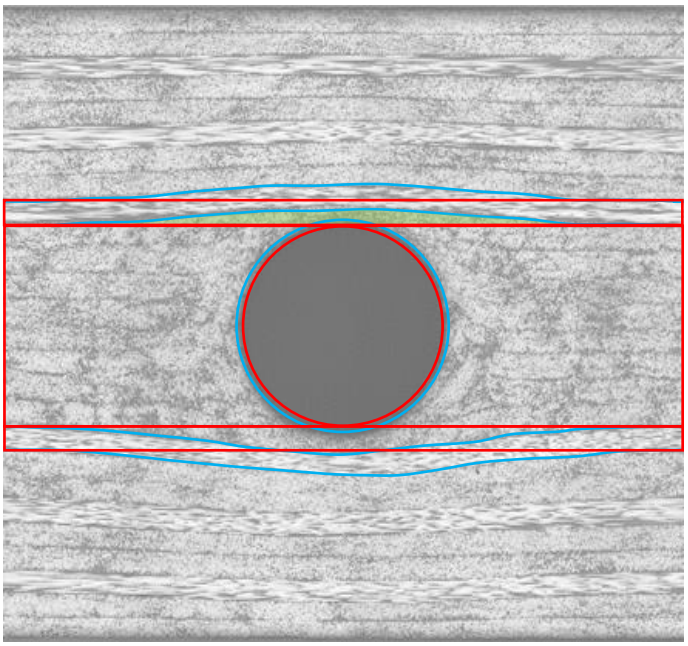

Figure 3.12: Expanded view of Figure 3.11 to emphasise fibre displacement. Red outlines representing the intended (red) and actual (blue) vascule diameter and boundaries between the 0° ply block and the surrounding 90° plies. The fibre waviness and vertically displaced 0° fibres (highlighted in green) caused by the larger wire diameter are clear.

with a maximum waviness angle of 5° and reducing amplitude toward the surfaces due to the flat constraint of the tool plates used during cure. It is possible that these waves caused a stiffening effect when the specimen was forced to bend longitudinally, much like a sheet of corrugated metal or cardboard. As flexural load was applied, in-plane stresses in the plies would reconfigure the strain responses in order to minimise the change in intrinsic curvature of each ply. This action would attempt to straighten the transverse waves, generating transverse and through-thickness stresses that contribute to flexural performance.

Table 3.1: Full in-situ thermo-mechanical testing results.

Temperature (°C)	Specimen type	Repeats	Coolant flow rate ($L \cdot min^{-1}$)	Flexural modulus (GPa)	CV (%)	Ultimate flexural strength (MPa)	CV (%)
23	Non-vascular	5	-	29.88	5.8	648.0	1.0
	Vascular	5	0	34.42	3.7	684.5	3.9
121	Non-vascular	3	-	28.62	0.9	574.2	0.6
170	Non-vascular	5	-	26.84	4.0	510.4	6.0
	Vascular	6	0	31.56	4.1	588.8	4.5
	Vascular	6	15	31.44	1.5	710.8	2.0
	Vascular (corr.)	as above		26.73	2.0	632.4	2.2

A correction was applied to the data for vascular specimens with 15 $L \cdot min^{-1}$ total coolant flow based on the average performance increase at 170 °C without coolant flow, due to the anomaly described above. Flexural modulus was not significantly changed, as shown in Figure 3.13, for the same reason that modulus was not largely decreased by elevated temperature; it is a fibre-dominated property that is highly temperature insensitive, so cooling has little influence also.

Flexural strength, however, was noticeably improved when coolant flow was active at 170 °C, with an increase of 20.7 % over the vascular specimens with zero flow, equating to an improvement of 23.9 % over the non-vascular specimens after correction (see Figure 3.13). Again, this was in line with expectation, as cooling improves the matrix and fibre-matrix properties which determine critical failure, though the magnitude of the performance retention was strikingly large.

Interestingly, despite the correction, the retained flexural strength at 170 °C with coolant flow exceeded that of the non-vascular specimens at 121 °C. Based on Figure 3.10, the performance was actually equivalent to that which might be expected at just 55 °C in a non-vascular specimen, a considerable margin of 115 °C from the environment temperature. This was a very significant finding; it demonstrated that the concept can retain a thermo-mechanical performance level that would occur within acceptable temperature limits in a non-vascular component, even when

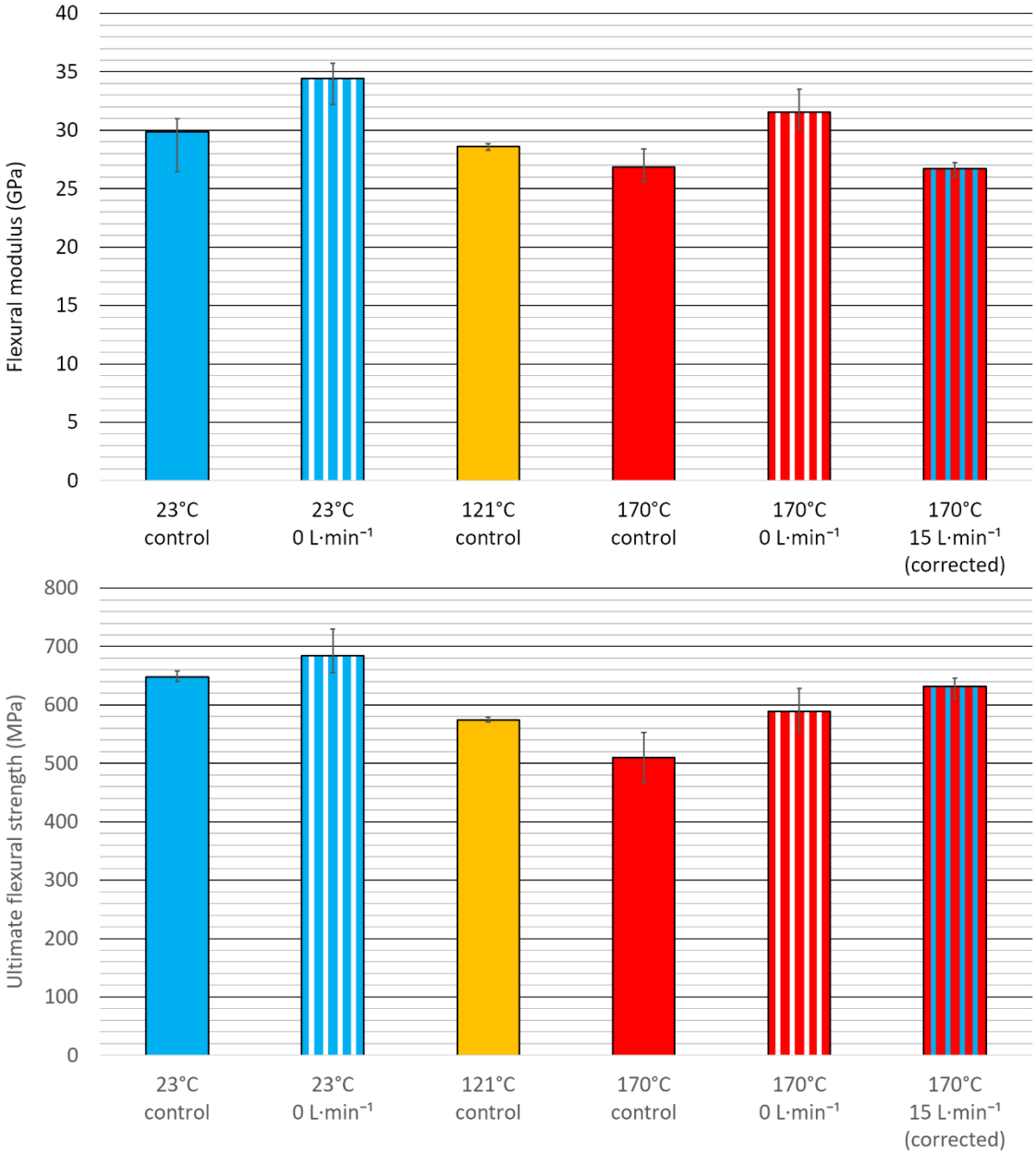

Figure 3.13: Flexural modulus and ultimate flexural strength at each test condition. Bars represent average values, with error bars showing the range of measured values. Data for 170 °C with 15 L·min^{-1} coolant flow is corrected to account for the manufacturing-induced performance increase.

operating at almost 50 °C above the maximum operating temperature, and just 30 °C below dry T_g. This finding proves that vascular cooling, even using air as the coolant fluid, can cool the surrounding matrix sufficiently to retain a significant portion of the ambient-temperature flexural thermo-mechanical performance.

3.3.2 Damage mode analysis

The fact that coolant flow only significantly improved flexural strength, and not modulus, provides some insight into the effects of cooling on the constituents of the composite. Carbon fibres retain virtually all of their ambient temperature performance up to 500 °C in air, or 1,500 °C in an inert

media [12]. As discussed in Chapter 2, the polymer matrix, and its interface with the fibres, are vastly more temperature sensitive. This implies that matrix and fibre-matrix interfacial properties and damage modes should be much more influenced by temperature than fibre-dominated ones. In the elastic deformation regime below T_g, flexural modulus is dominated by fibre modulus, and any change in matrix or fibre-matrix interfacial modulus has a minor effect on overall laminate performance.

Ultimate flexural strength, by contrast, is dominated by the critical failure mode of the specimen. In flexural testing of laminated FRP composites, this is highly dependent on the stacking sequence. In unidirectional specimens composed entirely of 0° plies, such as for ASTM D7264, failure may be manifested as tensile failure on the lower surface, and micro-fibre or ply-level buckling on the upper surface [6] due to direct tensile and compressive stresses. In multi-directional laminates such as those tested in this work, the stress state and failure mechanisms are more complex. Off-axis plies experience transverse direct stress components during flexure, exposing their weaker strength in this direction. The unusual stacking sequence in this case exposed the off-axis plies to the highest flexural strains, while the 0° plies experienced relatively low strains; a very unfavourable situation. The presence of defined ply interfaces in multi-directional laminates, and the step changes in stiffness across them, cause step changes in direct stresses. This generates large inter-laminar shear stresses which can easily exceed the corresponding interlaminar strengths, especially when these are reduced by elevated temperature. Hence inter-laminar cracking, or delamination, was the critical failure mode experienced in these experiments. Being dominated by matrix and fibre-matrix interfacial properties, delamination failure was highly sensitive to temperature changes due to environmental heating and vascular cooling, hence the larger variations in the data. This important observation implies that vascular cooling networks will be most beneficial in components where matrix or fibre-matrix interfacial property-dominated failure modes are critical. Their usefulness in components with fibre-dominated critical failure modes is likely to be much less, and it may not outweigh the added manufacturing complexity or additional coolant supply system mass.

As expected, failure of the outer off-axis plies was present in all tests, due to the high tensile and compressive strains and low transverse strengths. On the compression side, the outer ±45° plies experienced intra-laminar cracking which caused them to rupture at 45° to the bending direction. Outward buckling of these plies drove their delamination from the plies below. The 90° plies also exhibited intra-laminar cracking due to the through-thickness stresses caused by this outward buckling. These cracks appeared to travel in the bending direction, leaving parts of each 90° ply attached to the adjacent plies. On the tension side, the outer plies did not rupture, but a combination of plastic deformation and fibre scissoring caused a permanent strain, which led to

outward buckling when the specimen straightened upon unloading. Intra-laminar cracking of the 90° plies was also observed, as were subtle delaminations throughout the off-axis plies due to stiffness mismatches in the loading direction.

At 23 °C, non-vascular specimens exhibited the highest amount of intra-laminar cracking, indicating the brittle, rigid behaviour of the matrix in its glassy, sub-T_g state. Intra- and inter-laminar cracks were also found further inwards towards the 0° plies, but these were shorter in length and did not extend along the entire loading span (Figure 3.14a). The 0° plies were undamaged in all cases, and these provided residual stiffness that straightened the specimens upon unloading.

At 170 °C, delamination was much more prevalent than intra-laminar cracking, often extending along the full loading span (Figure 3.14b,c). This suggested that the elevated temperature, although below dry T_g, softened the matrix and improved its toughness, reducing intra-laminar failure. It also weakened the fibre-matrix interface, promoting inter-laminar failure. This ductile behaviour was also noted in the global failure behaviour of the specimen through the force-deflection curves. At 23 °C specimens failed abruptly from a peak load, typical of the brittle, stiff nature of FRP composites at ambient temperatures. At 170 °C, however, the failure occurred gradually in a 'rounding off' of the load-deflection curve, typical of a ductile material experiencing plastic deformation. In some cases, the extent of delamination in off-axis plies was sufficient that the remaining stress was directed through the 0° plies, causing them to fail via a shear crack (Figure 3.14c). This caused a permanent kink in the 0° ply block.

The vascular specimens at 23 °C and 170 °C without coolant flow exhibited much of the same failure mechanisms as pristine specimens at corresponding temperatures. However, an additional mechanism in the form of delamination of the 0°/90° ply interface on the tension side was noted (Figure 3.14d). It was suspected that the out-of-plane waviness of this interface increased its vulnerability to delamination under inter-laminar stress. This was significant because it risks rupture of the vascule wall, which was very close to this interface. The resulting coolant leak could severely impact on the downstream flow and cooling capacity. In a more connected, branched network this failure could disrupt the global flow distribution.

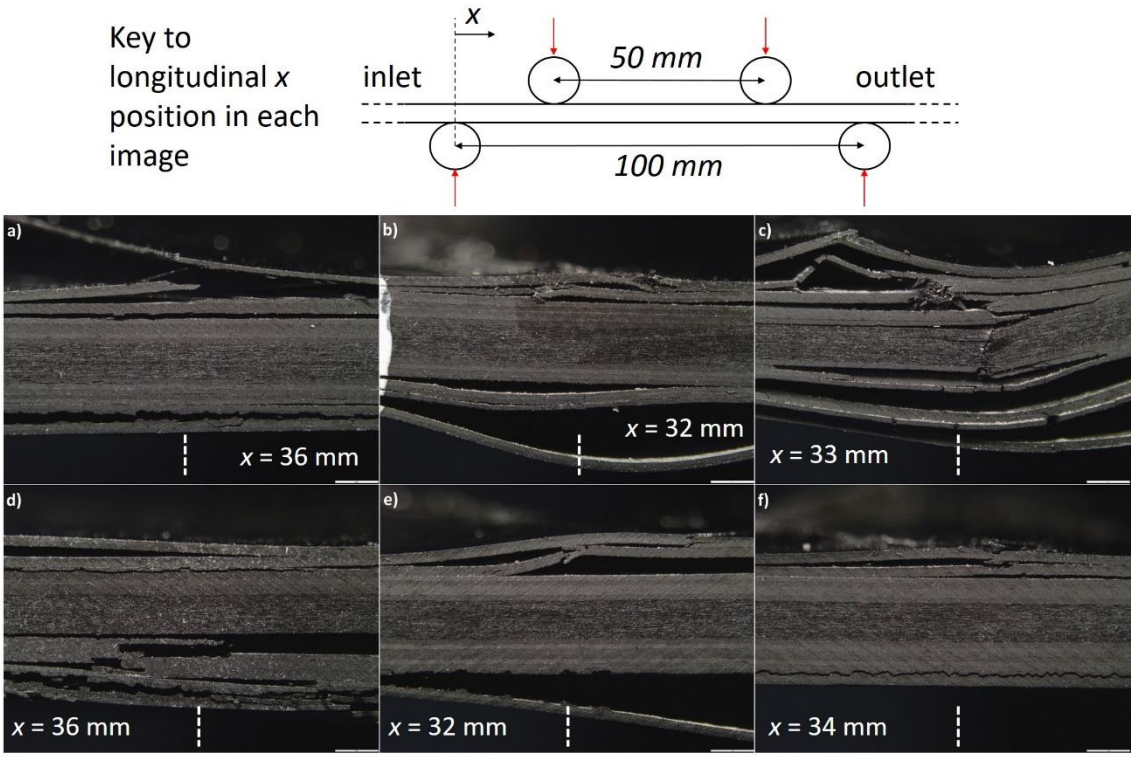

Figure 3.14: Optical micrographs of side view of failure zones; a): non-vascular, 23 °C. b) & c): non-vascular, 170 °C. d): vascular, 23 °C. e) & f): vascular, 170 °C, 15 L·min^{-1}. Intra-and inter-laminar cracks, splitting, buckling and shear cracking are all visible. Longitudinal positions, *x*, from the inlet-end support roller are given, marked by dashed vertical lines. Refer to the diagram above.

Some failure mechanisms in vascular specimens at 170 °C with maximum coolant flow closely resembled those in specimens at 23 °C (Figure 3.14e, f). The delamination and buckling of compression-side ±45° plies and intra-laminar cracking of tension-side 90° plies were both evident. Importantly, however, there was little to no delamination in the off-axis plies closer to the 0° ply block, and no failures of the 0°/90° ply interface on the tension side occurred. This was significant as it indicates that the temperature reduction achieved by the coolant flow was sufficient to preserve the integrity of these interfaces, where they would have otherwise failed due to temperature-related damage. This finding suggests that, despite the poor through-thickness thermal conductivity of the material, a large proportion of the thickness was cooled to a temperature where mechanical performance was improved.

3.3.3 Fluid dynamics considerations

While it was not possible to experimentally measure coolant velocity, at atmospheric pressure a coolant flow of 15 L·min^{-1} through four vascules of 1.1 mm diameter, D, should yield an average coolant velocity, V, of approximately 66 m·s^{-1}. Assuming a density, ρ, of 1.225 kg·m^{-3} and dynamic viscosity, μ, of 1.81×10^{-5} kg·(m·s)$^{-1}$, a Reynolds number, Re, of ≈4900 was determined:

$$\boldsymbol{Re} = \frac{\boldsymbol{\rho V D}}{\boldsymbol{\mu}} \tag{3.1}$$

Re ≥ 4000 indicates fully turbulent flow was present. As it produces more friction with the vascule walls, turbulent flow requires more pressure head to achieve a given flow rate compared to laminar flow, which would occur at *Re* < 2300 (less well-defined transitional flow occurs between these thresholds). Due to better mixing of the cooler fluid at the vascule centreline with the hotter fluid at the vascule wall, however, a greater mean temperature gradient occurs near the vascule wall, which drives greater heat transfer rates and better cooling performance than laminar flow.

The pressure differential between vascule inlet and outlet required to drive air at the selected flow rate was not measured. The total pressure head required to drive the flow through the supply system, including all pressure losses upstream of the vascules, was approximately 1.5 bar, which is not particularly high and should not pose significant barriers in terms of systems integration in any future applications.

3.3.4 Test apparatus limitations

The test apparatus and procedure in their current form have some limitations. As the chamber had only one hot air inlet, air currents may have occurred across the specimen which caused inconsistent heating. Any such currents are unavoidable with any external hot air supply, and the use of thermocouples to monitor the internal air temperature do not give good indication of any hot or cold spots. Hot air leakage past the flexible seals was also experienced, which was the primary factor limiting the upper temperature achievable. Only the total specimen coolant volumetric flow rate was measured, so any mismatch between individual vascule flows was not captured. This could have been caused by the internal flow pattern within the distribution manifold, slight differences in length of the supply tubing, imperfections in the vascules themselves or blockage due to foreign objects. The temperature and moisture content of the compressed air supply were not directly measured or controlled, both of which could have altered the cooling performance at a given volumetric flow rate. Any deformation in the fixture between the support noses and the base to which the potentiometer was attached would be measured as erroneous extra specimen deflection, though it is expected this was negligible. An improved setup would aim to measure and control these variables, which would help reduce errors that may be present in the current results.

3.4 Conclusions

The thermo-mechanical benefits of FRP composites with embedded vascules have been experimentally investigated. A moderate flow of air coolant at ambient temperature was supplied to flexural specimens containing four embedded vascules. While flexural modulus was relatively unaffected by environmental temperature or coolant flow, ultimate flexural strength showed greater sensitivity to these variables due to its dependence on matrix and fibre-matrix interfacial

properties. The experimentally tested coolant flow rate of 15 $L \cdot min^{-1}$ was sufficient to increase strength at elevated temperature by 23.9 % over non-vascular specimens, and retain a majority of the ambient temperature flexural strength, even when operating close to dry T_g. This confirms that air is a viable coolant choice for this concept, and useful performance gains can be realised in FRP composites exposed to elevated temperatures.

There is clearly a complex balance to be struck when designing FRP composite components containing vascular cooling networks. Thermo-mechanical performance should be maximised without introducing new critical failure modes, or prohibitively increasing cost or manufacturing complexity, and coolant demand minimised through considered network design. Damage or fault tolerance and serviceability are also important considerations for industrial applications. This novel concept has the potential to widen the scope of applicability for FRP composites in many different industrial applications, and there is much to be learned through future research to develop the technology to maturity for industrial adoption.

The original plan for this phase of experimental work included varying vascule diameter, pitch and coolant flow rate in addition to environmental temperature. However, the test methodology proved to be extremely time consuming, requiring around 3 to 4 hours per specimen, and the hot air supply equipment proved very unreliable at the highest temperatures. The scope of the work was scaled back to that presented in this Chapter, which nonetheless provided a qualitative validation of the potential of this technology in support of the relevant project Aims and Objectives. A more thorough exploration of the design space in future would require a more robust and efficient experimental setup, which itself would require considerable design and development effort.

Chapter 4: Thermal ageing

4.1 Introduction

While Chapter 3 investigated the immediate, short-term improvements in thermo-mechanical performance offered by vascular cooling networks, it is clear from the literature reviewed in Chapter 2 that the longer-term effects of elevated temperature must not be neglected. As discussed, polymers, and by extension FRP composites, can be subject to ageing by thermal exposure across several time scales. On medium time scales, incipient heat damage can permanently impair the fibre-matrix interfaces before visible damage develops. Over long periods, exposure to heat and atmospheric oxygen causes gradual degradation and decomposition, with the rate driven strongly by temperature. Thermal fatigue through temperature cycling can also cause damage if thermal expansion and contraction generate excessive internal stresses. All of these factors may impose service life limits on FRP composite components based on their thermal history, which must then be monitored. This burden may drive a decision to use a more thermally stable but heavier material, accepting the weight penalty.

A potential method to mitigate the medium and long-term effects could be to cool the material to a temperature at which thermal ageing occurs much more slowly. This may be achieved via embedded vascular networks based on the same principles as in-situ thermo-mechanical performance retention demonstrated in Chapter 3. Indeed, the results presented in Chapter 3 suggest temperatures can be lowered significantly using moderate flow rates of a cooling medium such as air through a basic network design, making longer-term testing a worthwhile endeavour.

The use of a variety of physical, chemical and mechanical analyses was planned in this phase of work to help better understand the thermal ageing process and the influence of vascular cooling, meeting Objectives 2D-E under Aim 2. The relevant damage mechanism(s) driven by thermal exposure over a range of durations were first stimulated, measured and analysed. Subsequent testing of residual mechanical performance then quantified the severity of ageing. The ability of an embedded vascular network to mitigate these thermal ageing effects was assessed, indicating how the time-temperature capabilities of FRP composites may be extended by such a technology.

The work presented in this chapter has also been reported in a journal paper currently under internal review and intended for publication in Composites Part A: Applied Science and Manufacturing. Some figures and text in this chapter are directly copied in that publication.

4.2 Experimental methodology

4.2.1 Thermal ageing process

Due to a variety of reasons including equipment availability, space restrictions and safety considerations raised by the experiments in Chapter 3, it was decided that any longer-term heating of specimens would need to take place in a discrete arrangement, with no applied load. The effects of thermal ageing and vascular cooling would be measured post-heat treatment via residual performance at ambient temperature. Dissociating the thermal exposure and mechanical testing aspects allowed much more scheduling flexibility and increased productivity through batch ageing. This section discusses the equipment and methods employed therein.

4.2.2 Environmental control

Due to the unreliability and excessive power demand of the Heatcon® Hot Air Curing System used in Chapter 3, an alternative heating method was sought. As the specimens in this experiment would not be simultaneously heated and mechanically loaded, heating via conduction through direct contact with a heated surface was now feasible. The maximum temperature of commercially available resistive heater mats is around 230 °C to 260 °C, in the range expected for this phase of work (ageing temperature choice is discussed in Section 4.2.3). The significantly lower thermal resistance of a conductive interface compared with a convective one yielded a much lower power demand, giving more flexibility in experimental setup, and better temperature control.

A pair of 150 mm by 150 mm silicone-based heater mats were powered via a controller based on the Watlow® EZ-ZONE® module operating at 110 V. According to Ohm's Law, operating the mats at half the rated voltage of 240 V also halved the current, reducing the nominal power of each 184 W mat by a factor of four to 46 W. Given that direct contact with the specimens was achieved, and the setup was well insulated, this was found to be sufficient. The mats each had a calculated power density of approximately 2 $kW \cdot m^{-2}$ at 110 V and 100 % duty cycle.

A sturdy platform was constructed from a thick aluminium plate, supported on clay bricks due to their low thermal conductivity, which limited conduction of heat down to the table surface below. Onto the plate was placed a layer of mineral wool thermal insulation material, and then the lower heater mat. The batch of three specimens was then placed on top of the heater mat, separated by around 30 mm, and the upper heater mat was placed over the specimens. Another stack of thermal insulation and an aluminium plate were placed on top. The entire stack was compressed by the weight of several house bricks placed on the upper plate to ensure good contact throughout. Both aluminium plates were electrically bonded to earth. The setup is depicted in Figure 4.1.

Figure 4.1: Photograph of heater mat apparatus, showing platform, aluminium plates, thermal insulation and heater mats (orange, protruding slightly from insulation material), feedback thermocouples and controller unit.

The heater controller was then programmed with the required settings including the desired ramp rate (5 °C·min^{-1} to 6 °C·min^{-1}) and target temperature or power (% duty cycle). Once the entire system reached thermal equilibrium, the time spent at the target temperature was recorded for each exposure.

4.2.3 Thermal exposure conditions

4.2.3.1 Exposure temperature

In order to design an experiment to investigate thermal ageing and its potential mitigation, an approximation of the temperature and duration of exposure required to cause a measurable mechanical performance reduction was needed. As this data is likely to vary between resin systems, information was sought for Hexcel® HexPly® IM7/8552, as used previously in this project, which was in ready supply and is mechanically well-characterised. Despite its widespread use in the aerospace industry and research community, there is very little experimental data quantifying the variation of mechanical properties as functions of environmental temperature or time. This is likely due to the conservative margins stipulated by the manufacturer for in-service conditions. A maximum service temperature of 121 °C is recommended [71] (well below the dry T_g of around 200 °C [72]), which may in part be to limit the actual ageing rate such that the performance reduction over a component's life remains negligible. Other factors are the large time commitment of performing such experiments, the requirement for specialised experimental apparatus, and the lack of standardised test methodologies.

Due to time constraints, ageing specimens for hundreds of days at 200 °C, as done by Wolfrum *et al*. [21], was deemed impractical. As the ageing process is accelerated by increasing temperature [23], a higher temperature was needed to obtain results in a reasonable time frame. The incipient heat damage mechanism investigated by Gaile [14] proves that a temperature of 250 °C can produce measurable thermal ageing within an hour.

Therefore, mirroring both the ageing temperature of 250 °C and the material system from Gaile's work, direct comparisons could potentially be made between the results collected. By extending the ageing duration further, the transition from medium-term incipient heat to long-term thermal ageing could be explored, and the ability of vascular cooling to slow, delay or inhibit these processes could also be investigated.

It should be emphasised that a temperature of 250 °C is an unrealistically harsh thermal environment in which to generate useful material characterisation data for this particular material system, as it was not designed for use above 121 °C. Concerns were raised that ageing above the final cure temperature (180 °C) and/or dry T_g (≈ 200 °C) would trigger residual cure, forming additional cross-links and possibly increasing mechanical performance initially. The findings of Chapter 3 and [14] dismissed these concerns; properties were not observed to improve in any case. Any residual cure phase would likely be very brief due to increased activation energy, and promptly masked by performance reductions caused by incipient heat damage and thermal ageing.

Also, it is understood that data from ageing above T_g can produce erroneous results in ageing calculations for below T_g, as the ageing rates are non-linear and the relative rates of different damage modes may be different [20], [73]. Again, the aim of this work was not to generate accurate quantitative material ageing data, but to make valid comparisons of relative performance between non-vascular specimens and vascular specimens with coolant flow under a range of ageing durations.

4.2.3.2 Thermodynamic boundary condition

The controller unit used to power the heater mats allowed for operation in two modes; varying power to maintain a set temperature, or maintaining power (via duty cycle) and allowing temperature to fluctuate. These represent the two ideal thermodynamic boundary conditions; constant temperature (Dirichlet) and constant heat flux (Neumann) respectively. In either case, to protect the heater mats from overheating, their temperature was measured directly, via thermocouples in direct contact with each mat.

If a constant surface temperature boundary was created, both non-vascular and vascular specimens could be heated to achieve the target 250 °C at the surface. When the vascular cooling system was activated however, it would draw heat energy away from the system, and the power supplied to the mats would increase accordingly to maintain temperature, due to the close conductive coupling between the specimen temperature and the feedback loop.

With a constant heat flux (power) boundary condition, the duty cycle of the heater mat controller would be fixed. This value was arbitrarily set by the user, with the thermocouple signal only used to prevent overheating of the heater mat. Heat energy would be input into the system at the same rate regardless of the rate of removal due to vascular cooling, and the specimen temperatures would find an equilibrium based on the ratio of these two rates.

The latter approach was deemed to better reveal the cooling power of the vascular network, and its ability to extract a certain proportion of a fixed heat flux into the specimen, thereby reducing its temperature and thermal ageing rate. While a constant *surface* temperature boundary condition is representative of some realistic scenarios, it would result in smaller differences in *internal* specimen temperatures between each coolant flow rate, and correspondingly smaller differences in thermal ageing and residual mechanical performance. To determine the correct heat flux value, a batch of non-vascular specimens were heated with a constant temperature target of 250 °C. Once the entire system was at thermal equilibrium, the duty cycle of each heater mat was noted at an average of 87.5 %, equating to a heat flux of 1.75 $kW \cdot m^{-2}$ per heater mat. Vascular specimens with coolant flow were then run with a constant power equal to this value. This yielded lower temperatures due to the cooling effect of the vascular network, always within the limits of the heater mat.

With respect to real-world applications, both boundary conditions are valid, and represent different situations and environments that FRP composite components may be exposed to. For example a constant temperature boundary condition may represent contact with an object whose temperature is held constant by some other heat source, such as equipment for chemical processing. A constant heat flux boundary condition could represent a fixed thermal radiation such as insolation or a nearby electrical device. It is rare in reality to achieve a pure boundary condition of either type, however, as there is often coupling between the two systems that share the boundary, and solid-fluid boundaries exchange heat via convection.

4.2.3.3 Exposure duration

Ageing duration was measured from when the specimen surface temperature stabilised, neglecting the time spent ramping up to this temperature, which was in the region of 45 minutes for non-vascular specimens to reach 250 °C. While this may have introduced error at the shorter ageing

durations, there was no practical way to avoid this. Ageing timing was stopped when the heater mats were deactivated, but the specimens were allowed to cool naturally inside the heater mats to ambient temperature before removal to reduce thermal shock. Ageing durations were 2 hours, 18 hours and 120 hours, in order to capture both the initial incipient heat damage and subsequent thermal ageing phases of the degradation process. Un-aged control specimens were set aside.

During the exposure the setup was inspected at intervals to assess the continuing safety of the test, but the specimens were not uncovered or removed. After cooling following the end of an exposure, specimens were removed, visually inspected, and stored for later mechanical testing.

4.2.4 Specimen design

For simplicity and comparability with Chapter 3, flexure remained the test method of choice. As heating and mechanical loading were no longer simultaneous, the thermal chamber and excessive specimen length requirement it drove were removed. Much shorter specimens of 140 mm length were manufactured, which increased specimen yield considerably, while maintaining compatibility with the same flexure fixture of 100 mm support span and 50 mm loading span.

The specimens used in Chapter 3 had very low flexural modulus for their thickness due to the stacking sequence, and they deflected to very high curvatures before failing, which is not a typical behaviour for an FRP composite component loaded in flexure. The curvature may also have exceeded the limit of validity of simple beam bending theory, whose small angle assumptions require a large radius of curvature compared to the beam thickness. To remedy this, the stacking sequence was modified to move 0° plies away from the neutral axis, increasing flexural modulus and strength, and reducing curvature at failure.

As the requirements of symmetry and locating vascules within 0° ply blocks remained, this necessitated two separate layers of 0° plies, and therefore two separate layers of vascules. In order to maintain good cooling performance, each layer retained the four vascule array from previous specimens, giving a total of eight vascules per specimen. Due to the risk of wire breakage during extraction, use of the 1.1 mm diameter wire was continued. A change in the wire manufacturer's insulation process resulted in a new wire diameter of 1.0 mm, matching the surrounding 0° ply block thickness. The wire had the same nichrome core diameter and so no greater risk of breakage on extraction. Due to the extra 0° plies, and the need to maintain a high support-span-to-thickness ratio, the number of +45°, -45° and 90° plies were reduced, with a final stacking sequence of $[+45/90/-45/0_8/+45/90/-45/90]_S$, and a nominal thickness of 3.75 mm. This new specimen design better represented a laminate designed for flexural loading, with high second moment of area by offsetting the 0° plies from the neutral axis, much like a sandwich panel. In all other respects the

specimen manufacturing method was identical to that used in Chapter 3, to which the reader is referred for details of aspects such as wire integration, lamination process and coolant supply tube interfacing. All specimen dimensions were recorded prior to ageing.

4.2.5 Coolant supply

Whereas supplying coolant at 15 $L \cdot min^{-1}$ to a single 4-vascule specimen was relatively simple, supplying similar flow rates to a batch of three 8-vascule specimens simultaneously presented a greater challenge. A large number of supply tubes were required, and there were no commercially available manifolds to split a single air source into this number of flows. Smaller manifolds arranged in several tiers of branching were considered, but space restraints required a more compact solution. A bespoke manifold was fabricated with a single inlet and 99 outlets (larger ageing batches inside wider heater mats were initially planned). A flowmeter was fitted to measure the total volume flow rate entering the manifold and, assuming well-distributed flow to the outlets, the flow rate per outlet could be assumed to be constant. This is shown in Figure 4.2.

Volumetric flow rate is commonly used to describe the rate of fluid flow through a system, hence most flowmeters measure this property. However, the mechanism of interest was the heat transfer between laminate and coolant within the specimen and, as discussed in Chapter 2, the capacity of a fluid to absorb heat energy is directly related to its mass flow rate, not volumetric flow rate. While volumetric flow rate may vary along a flow system due to temperature and pressure variations, mass

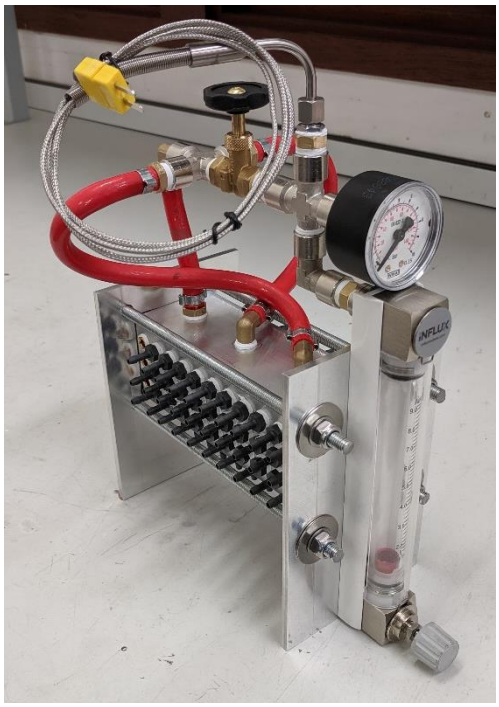

Figure 4.2: Photograph of coolant supply manifold, with flowmeter, control valves, pressure gauge and thermocouple visible.

flow is conserved as long as fluid is not lost or introduced anywhere. Volumetric and mass flow rates are related simply by the fluid density, which is proportional to absolute pressure and temperature at the point of measurement. Therefore, it was possible to determine the coolant mass flow rate through the flowmeter by measuring temperature and pressure, assuming 0 % relative humidity from the compressed air supply. This would equal the total mass flow rate through all specimens connected to the manifold, regardless of any changes in flow conditions throughout the system. Individual specimen and vascule mass flow rates could be calculated, assuming an equal split of mass flow between each manifold outlet. This was valid as the supply tubing for each vascule was of equal length, and the geometry and roughness of each vascule should also have been identical.

Coolant mass flow rates tested in vascular specimens were 0.00 $g \cdot s^{-1}$, 0.27 $g \cdot s^{-1}$, 0.53 $g \cdot s^{-1}$ and 1.00 $g \cdot s^{-1}$ per specimen. The zero and highest flow rates were tested first, and the flow approximately halved in stages until a significant reduction in residual flexural performance was experienced. Based on pressure measurements at the vascule inlets (discussed in Section 4.2.6), volume flow rates per vascule were calculated at around 1.6 – 6.3 $L \cdot min^{-1}$ (27 – 105 $cm^3 \cdot s^{-1}$), with velocities of around 35 – 129 $m \cdot s^{-1}$ and Reynolds numbers of approximately 2300 to 8500 (laminar-turbulent transitional flow to fully turbulent flow) [68].

In the interest of brevity, an identifier code is introduced here to indicate the specimen type, ageing duration and coolant flow rate, as per Table 4.1.

Table 4.1: Identifier code system for specimen types and experimental conditions.

Ageing duration (hours)	Non-vascular	Vascular at flow rate ($g \cdot s^{-1}$)			
		0.00	**0.27**	**0.53**	**1.00**
0	NV0	V0/0.00	-	-	-
2	NV2	-	V2/0.27	-	V2/1.00
18	NV18	V18/0.00	V18/0.27	V18/0.53	V18/1.00
120	NV120	V120/0.00	V120/0.27	V120/0.53	V120/1.00

4.2.6 Vascule pressure measurement

To calculate parameters such as coolant volumetric flow rate and pumping power, a vascular specimen was specially machined with a series of holes in one side at 14 mm intervals, intersecting with a vascule, and in the plastic section of the inlet hypodermic needle. Each pressure tap was either connected to a pressure sensor or plugged in turn to measure the vascule pressure profile. Flow characterisation was only performed at ambient temperature, and the specimen was not subsequently aged or mechanically tested. Fluid density, ρ, was calculated from measured absolute pressure, p, and assumed ambient temperature, which then allowed volumetric flow rate, $\dot{V}$, to be

calculated from the specimen's assumed equal share of the mass flow, $\dot{m}$, entering the distribution manifold. Pressure differential, Δp, and volumetric flow rate were then used to calculated ideal pumping power, P (assuming 100 % pump efficiency):

$$\boldsymbol{P = \Delta p \cdot \dot{V} = \frac{\Delta p \cdot \dot{m}}{\rho}} \quad (4.1)$$

4.2.7 Specimen surface thermography

While measurement of internal specimen temperatures would have provided very valuable insight into the vascular cooling effectiveness, it was not practical to perform experimentally. Instead, surface temperature profiles along the specimen length were captured, giving an indication of the general trends. As the outer surfaces were directly in contact with the heater mats they were assumed to represent the hottest temperature at each specific position, with the bulk material within experiencing temperatures no higher than this. To minimise lifting of the heater mats away from the surface, very fine K-type thermo-couples were attached with small patches of PTFE tape. Sensors were attached at regular longitudinal positions, on both upper and lower surfaces, to yield an averaged longitudinal temperature profile. A vascular specimen was exposed to a 2-hour ageing cycle at each coolant flow rate, sufficient to reach steady state temperatures, as was a non-vascular control specimen.

4.2.8 Mechanical testing

Flexural properties were measured at ambient temperature after ageing using the same custom-made four-point bend fixture as in Chapter 3, having a 100 mm support span and 50 mm loading span. The increased specimen thickness now gave a support-span-to-thickness ratio of 26.7:1. While below the recommended 32:1 given in ASTM D7264 [70], the standard is intended for UD specimens that experience direct stresses and fibre tensile failure in line with beam theory. Multi-directional laminates typically fail via delamination in flexure, and the objective here was not to generate accurate material flexural performance data, so this non-compliance was deemed acceptable. Centre-point deflection was measured on the specimen underside by a linear potentiometer, and applied load via the test machine load cell. Crosshead displacement rate was 1 mm·min^{-1}, and the test was stopped when a sharp load drop was detected (indicating failure) or the potentiometer travel limit was approached. Flexural stress and strain were calculated according to beam theory for comparative purposes, and modulus was derived from the gradient of the stress-strain plot from 0.1 % to 0.3 % flexural strain. Ultimate flexural strength was taken as the maximum value of flexural stress before the first major load drop. Six repeats were performed at each experimental condition.

4.2.9 Infrared spectroscopy

Chemical analysis of Hexcel® HexPly® IM7/8552 determined that the resin contains a blend of two epoxy monomers; tetraglycidyl-methylene-dianiline (TGMDA, also known as tetraglycidyl-diamino-diphenylmethane, TGDDM) and triglycidyl-p-aminophenole (TGPAP). These are cured by the amines 3,3'- or 4,4'-diaminodiphenylsulfone (DDS), and the resulting epoxy is toughened with the thermoplastic poly-ethersulfone (PES) [22]–[24]. Using Fourier Transform Infrared Spectroscopy (FTIR), two characteristic spectral peaks for the matrix correspond to the TGMDA epoxy component at 1510 cm^{-1}, and the PES toughener at 1486 cm^{-1} [74]. TGMDA has been found more susceptible to thermal decomposition than PES, so a reduction in the intensity ratio $R = I_{1510}/I_{1486}$ occurs with thermal ageing, which has been noted by several authors [21], [24]–[27], [75]. Samples from the inlet and outlet ends of various specimens were mounted, ground and polished to a depth within 100 µm of the outer surface. Spectra were captured using a Thermo Scientific™ Nicolet™ iN10 MX FTIR spectrometer with a Germanium tip ATR accessory. Spectra were obtained from an area of 80 µm x 80 µm at 4 cm^{-1} resolution, averaging over 128 scans. After baselining and normalising the spectra at the PES reference peak at 1486 cm^{-1}, the changes in R with ageing duration and coolant flow rate were calculated.

4.2.10 Fractographic analysis

Fractographic analysis of the failure surfaces of various specimens was performed via collaboration with Prof. Emile Greenhalgh and Dr. Tomas Katafiasz from the Department of Aeronautics, Imperial College London. NV0, NV2, NV18, NV120 and V18/1.00 specimens were analysed. A wider range was originally selected for analysis, but time constraints following lab closures due to COVID-19 required prioritisation

A Hitachi S-3700N scanning electron microscope (SEM) was used to image fracture surfaces of the specimens. Samples were mounted on aluminium stubs using a two-part epoxy, which was mixed with carbon black to provide a conductive path and permit charging of the sample. The sample surface was then coated with gold via sputtering under vacuum for 20 seconds.

4.3 Experimental results & discussion

4.3.1 Specimen surface thermographic analysis

Figure 4.3 shows the longitudinal surface temperature profile of a non-vascular specimen, and a vascular specimen at each coolant flow rate, along with thresholds at the material manufacturer's recommended maximum operating temperature (121 °C) [71], and the material dry T_g (207 °C) [72].

It is clear that even at the lowest coolant flow rate, the entire specimen surface is cooled significantly. All positions also remained below dry T_g with a significant margin, and the first 50 mm downstream from the coolant inlet end remains below the manufacturer's recommended operating temperature limit, further reinforcing the effectiveness of this method of thermal management for FRP composites. At the higher coolant flow rates, the entire specimen surface remains below the manufacturer's recommended operating temperature limit. The small reduction in temperature at each end of the non-vascular specimen was due to natural convective cooling with the lab atmosphere, and the fact that the heater mat element did not extend all the way to the mat edges.

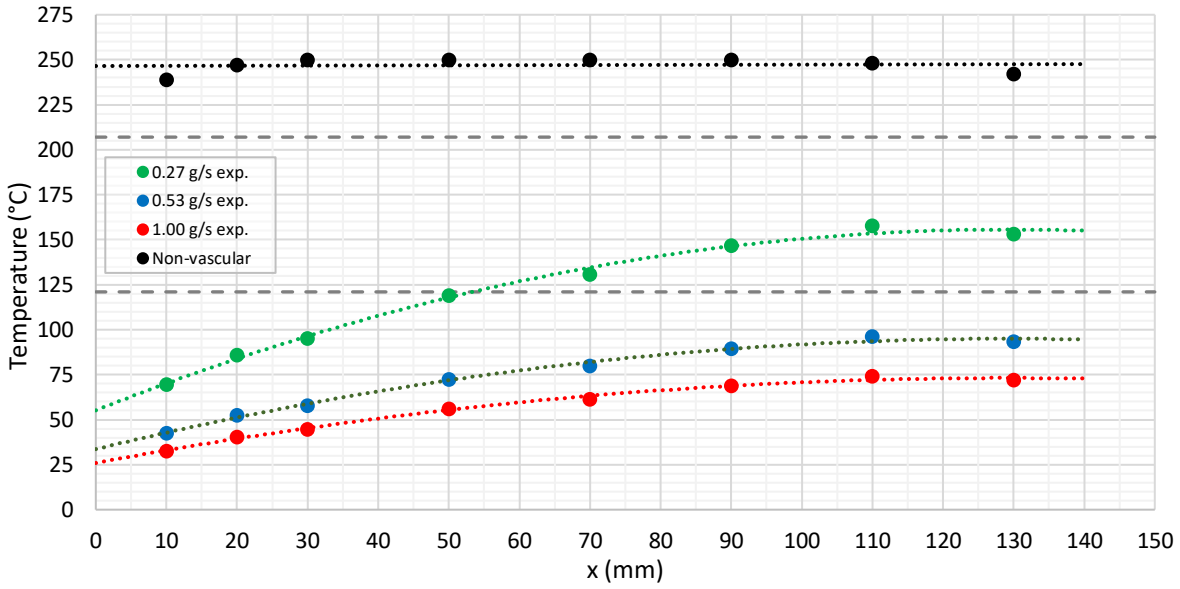

Figure 4.3: Vascular specimen longitudinal thermal profile at each coolant flow rate, compared to a non-vascular specimen at the same heat flux. Material maximum operating temperature and dry T_g thresholds are also indicated as dashed lines.

4.3.2 Visual inspection

4.3.2.1 Non-vascular specimens

Upon removal from the heater mats, NV0 and NV2 specimens exhibited no visible signs of degradation. The upper and lower surfaces of NV18 specimens exhibited a slight change in reflective properties that varied with orientation of the surface fibres with the light. In NV120 specimens this visual change was intensified, along with a change in surface texture from smooth to slightly rough. This indicated a thinning of the surface matrix layer due to thermal decomposition and volatilisation, with resulting exposure of the underlying fibres. At the specimen ends, small intra-laminar cracks could be seen within the 0° ply zones, as shown in Figure 4.4. It was also clear that their transverse distribution was very regular. In some cases, inter-laminar cracks also appeared at the interfaces between 0° and neighbouring 45° plies. Without regular checks during ageing it was impossible to

Figure 4.4: Photographs of the ends of an NV120 specimen, showing the intra- and inter-laminar cracks present.

determine exactly when these cracks began appearing, but this would be a useful observation to make in future work.

The micro-cracking was attributed to residual thermal stresses generated by the mismatch in thermal expansion coefficient between fibre and matrix, and at ply interfaces. All FRP composite laminates have a property known as stress-free temperature, the temperature at which the cross-linked network forms (vitrification) in thermo-setting matrices, and crystallisation occurs in thermo-plastic matrices. At this temperature thermal residual stresses are zero, and for IM7/8552 this is taken to be the final cure temperature of 180 °C. As discussed in Chapter 2, carbon fibre has almost zero CTE, but the polymer matrix would preferentially contract below the stress-free temperature, and expand above it. In multi-directional laminates this causes complex stress states on a constituent scale at the fibre-matrix interface, at the ply scale and the laminate scale. It is for this reason industrial layup guidelines recommend minimising the angular difference in orientation of adjacent plies, and avoiding continuous blocks of four or more of plies of the same orientation. This minimises thermal contraction stresses after curing, limiting inter-laminar stresses at ply interfaces, and limits the propagation of intra-laminar cracks through the laminate should they initiate.

Clearly, the laminate tested in this work breaches the latter recommendation, with continuous blocks of eight 0° plies. Heating through the stress-free temperature would cause thermal residual stresses to reduce, reverse in direction and increase again. However, the absolute temperature difference from the stress-free temperature is in the region of 160 °C at ambient conditions, but just 70 °C at the ageing temperature of 250 °C. This implies that thermal residual stresses should be less than half in magnitude and, therefore, unlikely to cause micro-cracking of their own accord. Also, transverse thermal expansion of the 0° ply blocks would be constrained by tension in the surrounding ±45° and 90° plies, generating transverse compression in the 0° plies that is not

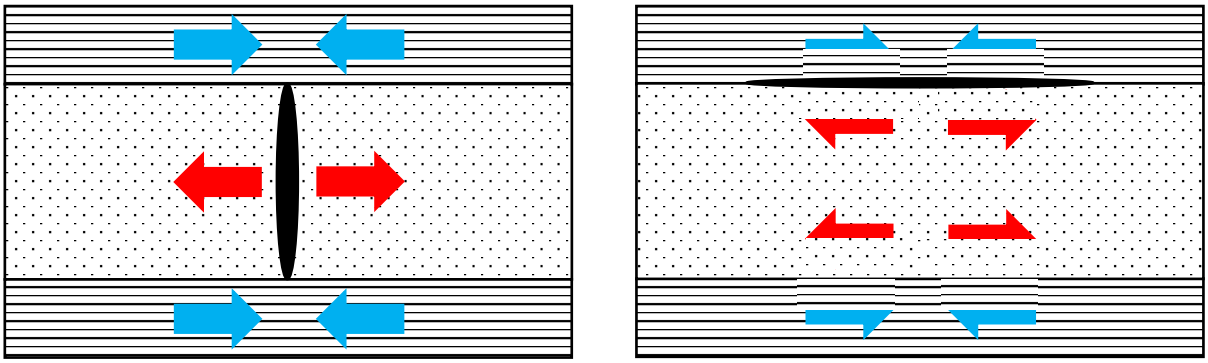

Figure 4.5: Diagrams of representative specimen cross-sections to illustrate thermal residual stresses. 0° plies are represented by dotted areas, and ±45° and 90° plies are represented by horizontal lined areas. Arrows depict residual thermal stresses caused by thermal contraction of 0° plies upon post-ageing cool-down, and constraint of surrounding ±45° and 90° plies.
Left: transverse tension (red arrows) in 0° plies and transverse compression in surrounding plies (blue arrows), leading to intra-laminar through-thickness cracking (black oval).
Right: inter-laminar shear stresses (red & blue half-arrows) across 0°/±45° ply interface, leading to inter-laminar cracking (black oval).

conducive to the intra-laminar through-thickness cracks observed, which must be the result of transverse tension as depicted in Figure 4.5.

Therefore, an alternative theory is proposed. It is conceivable that heating above T_g may have instead allowed thermal stresses to be slowly relaxed during ageing, due to matrix softening via secondary inter-molecular bond breakage, and visco-elastic stress relaxation as discussed in Chapter 2. This would effectively raise and 're-set' the stress-free temperature closer to the ageing temperature, with the thermally-expanded state being the new zero-stress state of the laminate. Cooling to ambient temperature following ageing would then result in a much larger absolute temperature difference of up to around 230 °C, greater than that experienced during normal post-cure cool-down, and more likely to cause micro-cracking. The residual stress in this scenario is transverse tension in the 0° ply blocks due to constrained thermal contraction, which better explains the observed damage. The raising of the stress free temperature would be a gradual process, and so the thermal residual stresses upon cool-down after 120 hours would be greater than after 2 hours. This, in combination with the increasing weakening of the matrix and fibre-matrix interfaces with continued thermal ageing, would cause fractures that increase in density with ageing duration.

This mechanism would rely on the inter-laminar cracks forming after the intra-laminar cracks, otherwise the inter-laminar constraint required to generate the transverse tensile stress would be lost. Specimens in this work were not directly monitored to during the heating/ageing/cooling cycle to verify this theory. However, in trials by the author of the heater mat setup used in this work, specimens were exposed to similar ageing conditions for up to 3 hours. Distinct 'popping' sounds were audible as specimens cooled, and similar matrix micro-cracking was later noted. This was likely due to rapid crack propagation during cooling, so it is considered likely that the proposed

mechanism was indeed at play in the presented work. Monitoring of crack formation via visual or audio recording would be an important feature of future experiments.

4.3.2.2 Vascular specimens

Vascular specimens showed none of the visual signs of degradation found in non-vascular specimens, including those with zero coolant flow. A minor exception were V120/0.27 specimens, which did exhibit some of the surface appearance changes noted above. This was an immediate indication that, with active cooling, their temperatures were generally lower, and the ageing processes had been slowed.

4.3.3 Residual flexural performance

4.3.3.1 Non-vascular specimens

Figure 4.6 clearly shows that ultimate flexural strength of non-vascular specimens suffers a substantial loss in the first 2 hours of ageing, dropping to approximately 64 % the un-aged value. This is consistent with the process of incipient heat damage, which has been found to cause significant degradation within a matter of hours at this ageing temperature range [14], [26]. The residual strength decrease continues following a power law, reaching 37 % at 18 hours and 18 % at 120 hours. Another important feature is the scatter; this is low in un-aged specimens as expected, giving confidence in the experimental repeatability. A significant increase in scatter occurs from 1 to 18 hours, further indicating a damage accumulation process active in this time frame whose progression in each specimen is somewhat localised and stochastic. This leads to wider variations in strength at these ageing durations, as some specimens have a more critical accumulation of damage than others at the point of testing, as noted by Tsotsis *et al*. [73]. This variation could be due to a

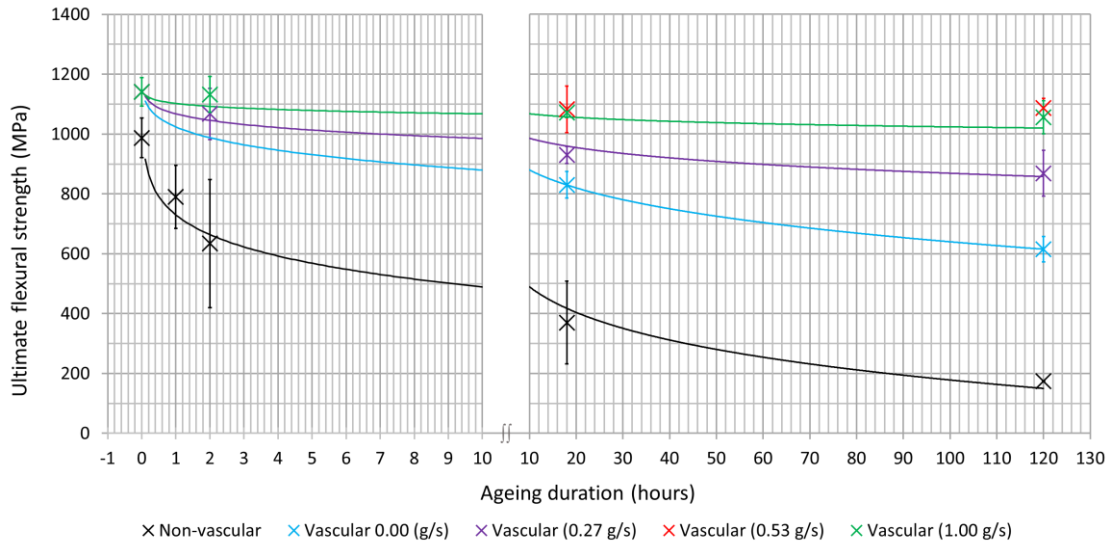

Figure 4.6: Variation of ultimate flexural strength with ageing duration for various coolant flow rates. The trend line for 0.53 g·s^{-1} is not shown for clarity. Error bars represent one standard deviation from the mean.

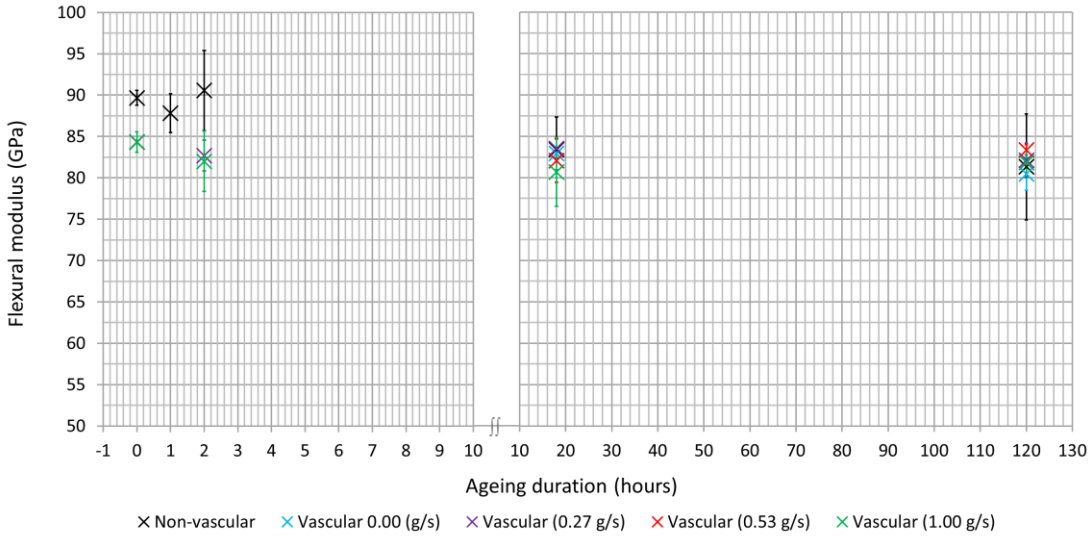

Figure 4.7: Variation of flexural modulus with ageing duration for various coolant flow rates. Trend lines are not shown due to inconsistent trends and large scatter. Error bars represent one standard deviation from the mean.

wide range of minute differences between specimens and their individual thermal histories, and the chaotic, unpredictable processes of crack initiation and propagation. After 120 hours of ageing the scatter is once again low, suggesting that the damage accumulation is nearly complete or saturated (supported by the visual signs of damage), and the dominant mechanism has transitioned to the much slower process of thermal ageing of the polymer matrix.

By contrast, flexural modulus, shown in Figure 4.7, appears to be maintained at the un-aged level up to 2 hours ageing duration, with scatter increasing with time. Only after 18 hours does flexural modulus reduce more significantly to 93 %, but even after 120 hours the reduction remains comparatively low at just 91 %. This is as expected; modulus is calculated in the linear elastic region of the stress-strain curve well before any bending-induced damage occurs. The fibre-matrix interfaces, despite being weakened by incipient heat damage, are not stressed beyond their remaining strength, and so remain intact and able to transfer load to the fibres as effectively as in an un-aged specimen. As the fibre performance is not degraded at the temperatures tested, and the specimen bending properties are dominated by the two 0° ply blocks, flexural modulus is greatly less affected. The gradual reduction in modulus at longer ageing durations is attributed to the greater levels of ageing-induced cracking present, which prevented effective load transfer within the specimen, and also the minor contribution of matrix property degradation due to thermal ageing.

4.3.3.2 Vascular specimens

Firstly, vascular specimens were tested after ageing at all durations with zero coolant flow, to reveal any influence of the presence of vascules on performance. The results presented in Chapter 3 indicated that laminate structure disturbances caused by the presence of the vascule pre-form wires

during cure can artificially increase flexural properties, in particular strength. This would suggest that simply embedding vascules can boost flexural performance, without the need to actually flow coolant. This increase was also noted in the current strength results, and is illustrated in Figure 4.6, ranging from 15 % in un-aged specimens to 253 % at 120 hours. As in Chapter 3, this increase was attributed to displacement of 0° fibres away from the specimen neutral axis, caused by trapping of fibres situated above and below the wires after the lamination process. With two vascular planes themselves displaced from the neutral axis, rather than one vascular plane centred on the neutral axis, the increase in flexural performance was compounded. It was found that these trapped fibres yielded an increase in specimen thickness by around 7 % to 4.00 mm, and the reduction in support span-to-thickness ration from 26.7:1 to 25:1 may have slightly altered the stress state within the specimens in a manner that increased their strength. The reason for the greater increase in strength with ageing duration is not fully understood, but would be of limited value as these anomalies were purely artefacts of the vascule fabrication process chosen, and specimens manufactured by an alternative method that had less impact on laminate structure would likely not show such an increase in flexural performance at zero coolant flow. It is also conceivable that a small amount of passive cooling took place due to natural buoyancy-driven flow through the vascules, though this effect was not expected to be significant as specimens were not significantly tilted from horizontal.

Flexural modulus for all vascular specimens was almost constant for all ageing durations and coolant flow rates, as shown in Figure 4.7, which is as expected due to reasons discussed previously for non-vascular specimens.

A noteworthy result is that the ultimate flexural strength values shown in Figure 4.6 for 1.00 $g \cdot s^{-1}$ and 0.53 $g \cdot s^{-1}$ coolant flow are almost identical. Strength is virtually unaffected after 2 hours at 1.00 $g \cdot s^{-1}$ coolant flow (data for 0.53 $g \cdot s^{-1}$ coolant flow was not collected at this duration), and reductions of approximately 5 % to 7 % followed over 18 hours, after which the residual strength is effectively constant up to 120 hours at around 93 % to 95 %. This suggests that both of these coolant flow rates were equally, though not totally, effective at preserving residual flexural strength, and coolant flow rates met or exceeded the minimum required to maintain residual strength in the long term. This is supported by the thermography results presented in Section 4.3.1, which show specimen temperatures entirely below the manufacturer's recommended maximum operating temperature for both coolant flow rates. The lack of any significant performance reduction within the first two hours of ageing precludes the incipient heat damage mechanism that occurred in non-vascular specimens, with visual inspection, fractography, thermography and IR spectroscopy (discussed later) all supporting this. Instead, the more gradual reduction over the first 18 hours is attributed to possible post-cure reactions in the matrix triggered by heat input, or damage due to vaporisation of

absorbed moisture from storage, both of which would not sustain over longer periods. These theories require further investigation, however.

The similarity in results for these two higher coolant flow rates reveals an important limitation and non-linearity in cooling capacity of the specimen design. Increasing coolant flow beyond 1.00 $g \cdot s^{-1}$ would yield a relatively small thermal ageing reduction with a large penalty in pumping power. A different coolant fluid, vascule morphology or flow configuration such as alternating-flow, would be required to fully retain performance.

A further reduction of coolant flow rate to 0.27 $g \cdot s^{-1}$ was made, in an attempt to further investigate the critical minimum flow rate required for long-term preservation of flexural performance. A clear divergence from the trends for higher coolant flow rates is shown, indicating that this flow rate is below the critical minimum. Residual strength was 94 % after 2 hours, 82 % after 18 hours and 76 % after 120 hours. The cooling influence of the vascules was clearly reduced sufficiently to cause more global thermal ageing, including damage to the fibre-matrix interfaces closer to the mid-plane, which are critical to the flexural stress at failure for this specimen design and loading.

Scatter was consistently lower in vascular specimens than non-vascular specimens, indicating a reduced rate of damage accumulation due to the reduced matrix temperatures.

Table 4.2: Residual flexural performance of specimens at each ageing duration and coolant flow rate (in $g \cdot s^{-1}$), with Coefficient of Variation (CV) percentage in parentheses.

Ageing duration (hours)	Residual flexural modulus (GPa)					Residual ultimate flexural strength (MPa)				
	NV	**0.00**	**0.27**	**0.53**	**1.00**	**NV**	**0.00**	**0.27**	**0.53**	**1.00**
0	89.68 *(1.0)*	84.33 *(1.5)*	-	-	-	988 *(5.3)*	1141 *(3.9)*	-	-	-
2	90.55 *(5.3)*	-	82.68 *(2.2)*	-	82.00 *(4.4)*	634 *(33.8)*	-	1067 *(8.0)*	-	1133 *(5.3)*
18	83.40 *(4.7)*	82.92 *(2.4)*	83.55 *(1.4)*	82.07 *(3.2)*	80.70 *(5.2)*	370 *(37.2)*	830 *(5.4)*	930 *(3.1)*	1082 *(7.1)*	1071 *(1.5)*
120	81.32 *(11.5)*	80.48 *(2.5)*	82.11 *(2.5)*	83.36 *(0.7)*	81.83 *(2.0)*	174 *(1.8)*	615 *(6.8)*	869 *(8.8)*	1086 *(3.0)*	1056 *(5.2)*

4.3.4 IR spectroscopic analysis

The measured peak intensities for each IR spectra were determined, yielding a set of *R* ratios for each sample that were then averaged and normalised by the un-aged specimen value. Table 4.3 shows that over 18 hours of ageing in the non-vascular specimen, a drop in the intensity ratio to 0.90 occurred, indicating thermal degradation of the TGMDA epoxy monomer near the specimen surface. After 120 hours, the ratio reached 0.78. By contrast, at the maximum coolant flow rate of 1.00 $g \cdot s^{-1}$

the intensity ratios at the inlet and outlet ends were 0.99 and 0.98 at 18 hours, and 1.01 and 0.93 at 120 hours, respectively. Due to the inherent variability in FTIR analysis caused by noise and spectral resolution, ratios around 1.00 ± 0.02 can be considered unchanged. The latter result is interesting, as it indicates thermal decomposition due to the higher matrix temperatures experienced at the outlet end, even when the inlet end is apparently free from thermal decomposition.

The results at the inlet end of the specimen with the lowest coolant flow rate of 0.27 $g \cdot s^{-1}$ are also essentially unaffected at 0.99 and 1.00 after 18 hours and 120 hours respectively. At the outlet end the evidence of chemical decomposition did occur, with residual intensity ratios of 0.94 and 0.96 at 18 hours and 120 hours respectively. This indicates that specimen temperatures at this flow rate were sufficiently high to increase the decomposition rate, causing a similar magnitude of decomposition to the higher coolant flow rates at 120 hours in just 15 % the duration. It also follows that decomposition-inducing temperatures were experienced over a greater length of the specimen, as confirmed by the thermography results in Section 4.3.1, which would cause more widespread thermal damage corresponding with the reduced residual mechanical performance.

Table 4.3: Effect of ageing duration and coolant flow rate on relative intensity ratio, *R*. Values are given at the coolant inlets and outlets for vascular specimens.

Ageing duration (hours)	Relative intensity ratio, *R*				
	Non-vascular	Vascular			
		1.00 $g \cdot s^{-1}$		0.27 $g \cdot s^{-1}$	
		inlet	outlet	inlet	outlet
0	1.00	1.00	1.00	1.00	1.00
18	0.90	0.99	0.98	0.99	0.94
120	0.78	1.01	0.93	1.00	0.96

The observed reductions in *R* ratio for non-vascular specimens are small in comparison to those observed in the literature; Eibl & Wolfrum [26] saw ratios of around 0.1 after 5 days at 240 °C, and around 0.25 after just 5 hours at 260 °C in the same material system. Differences may lie in the heating method; those authors used convection ovens which would have exposed more of the specimen surface to a constantly circulating supply of air. The direct contact between heater mats and the largest specimen surfaces in the present experiment may have limited oxygen diffusion and slowed the decomposition process. All vascular specimen readings at all coolant flow rates exceeded the non-vascular *R* value after just 18 hours, even at durations over 550 % longer. It is clear that, despite a small initial decomposition, vascular cooling has the ability to maintain the chemical integrity of the matrix for much longer periods than would otherwise be possible.

These findings prove that thermally-induced chemical decomposition mechanisms of the matrix can be slowed significantly via vascular cooling. While only a single oxidation mechanism was explored in this work, a similar effect might be expected in other epoxy-based resin systems. They also reinforce the importance of accurately predicting the magnitude *and* location of temperature maxima in a vascular FRP composite component, and understanding the influence of network topology on them, as localised thermal ageing can progress rapidly if hotspots are allowed to exist. For example, simply having coolant ingress shared between each end of the specimen, creating an alternating-flow network, would likely improve the cooling efficiency of this specimen design, and provide more uniform cooling along the entire length that would avoid zones with excessive/deficient cooling.

4.3.5 Fractographic analysis

Analysis of the fracture surfaces of non-vascular specimens revealed a significant change in fracture behaviour with ageing duration, which was largely based on the appearance of cusp features. A full description of cusp formation and their use in fractographic analysis is given in [76], but in summary they are platelet-shaped formations of resin material caused by shear stress between plies and the propagation of micro-cracks. The angle of cusps to the fracture plane is related to the mode of interlaminar failure; steep cusps at a high angle form under Mode II-dominated failure, whereas shallow cusps form under Mode I-dominated failure. While typical interlaminar failures occur under a mix of the two modes analysing the cusps can provide an insight into the dominant mode, and behaviour of the matrix and fibre-matrix interface.

The un-aged specimen (Figure 4.8a) showed uniform cusp formation, with a relatively high cusp tilt angle indicative of a Mode II-dominated interlaminar failure, where the matrix failed cohesively under shear stress. After 2 hours of ageing, cusps were still present and uniform, but the tilt angle was relatively shallow, a sign that Mode II interlaminar failure was less dominant (in other words the failure became more mixed-mode). This was a result of the degraded fibre-matrix interface, which caused greater fibre-matrix interfacial adhesive failure, and therefore lower shear stresses to be generated in the matrix between plies.

This trend continued to 18 hours (Figure 4.8b), with even lower levels of Mode II failure evidenced by fewer, shallower cusps. At this duration poor fibre-matrix interfacial bonding was also indicated by smooth fibres and complementary imprints. This is another sign of a shift from matrix cohesive failure, which tends to leave matrix material on fibres, to fibre-matrix interfacial adhesive failure, where the fibre-matrix bond is severed cleanly. This is consistent with the findings of other authors [14], [21] following thermal exposure. After 120 hours of ageing (Figure 4.8c), cusp tilt angles were

very shallow, and smooth fibres and imprints were widely observed, due to further fibre-matrix interfacial degradation and reduced Mode II interlaminar failure.

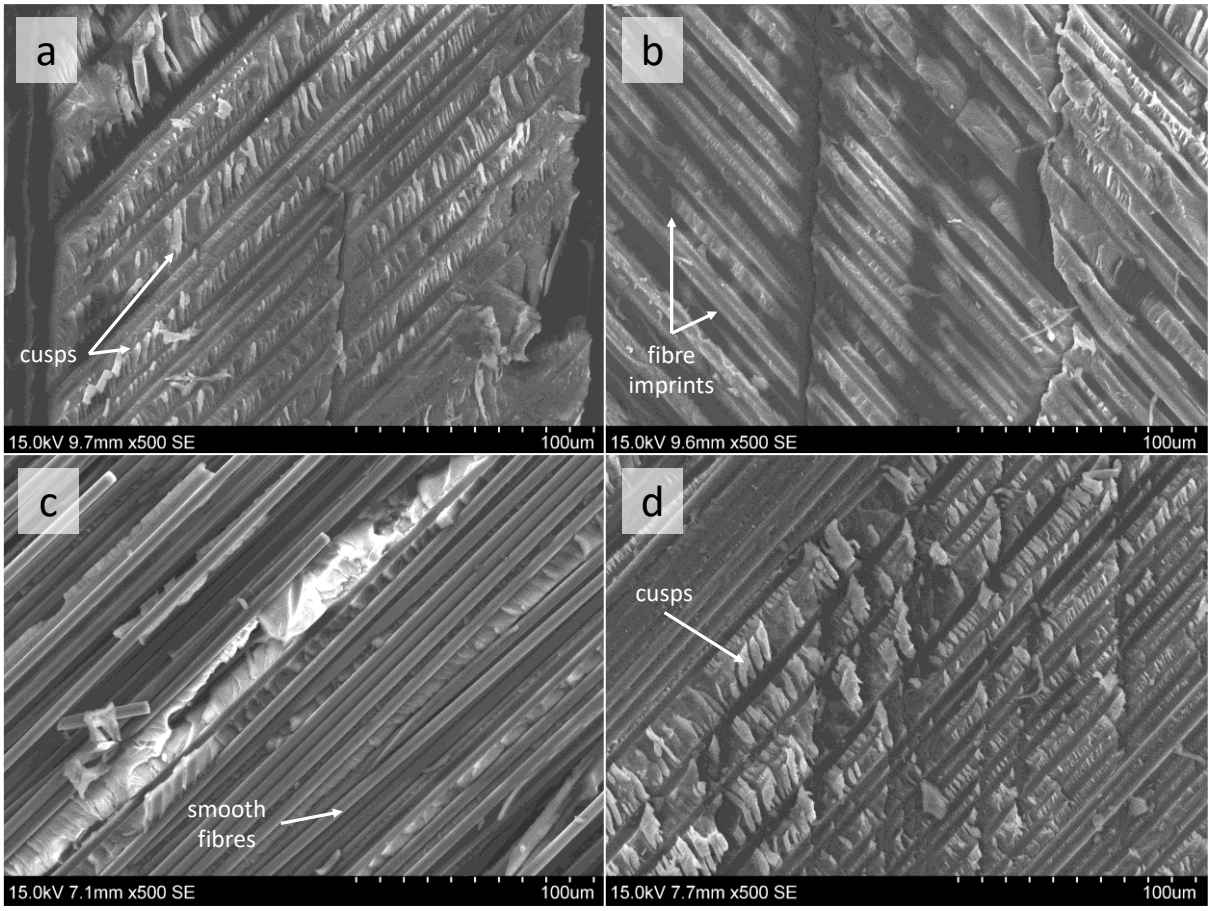

Figure 4.8: Typical SEM images of fracture surfaces from flexural specimens. NV0 (a), NV18 (b), NV120 (c) and V18/1.00 (d). All magnifications x500. Cusps, smooth fibres and imprints are annotated.

By comparison, the V18/1.00 specimen (Figure 4.8d) showed fracture surface morphology more typical of lower ageing durations. Cusp tilt angles were relatively high, similar to non-vascular specimens aged for 0 to 2 hours, indicating Mode II-dominated interlaminar failure. Smooth fibres and imprints were not prevalent either, suggesting the lower temperatures yielded by vascular cooling preserved the fibre-matrix interfacial properties.

This fractographic data is micro-scale evidence of a shift in critical failure mode during post-ageing mechanical testing, which was directly responsible for, and complementary to, the macro-scale strength reductions. Non-vascular specimens suffered continuous reductions in residual ultimate flexural strength and the IR intensity ratio *R* with ageing duration. Taking 18 hours ageing duration as a comparison point, ultimate flexural strength was reduced to just 37 % of the un-aged value, and the value of *R* was 0.90, indicating physical and chemical ageing had occurred. The observed post-ageing matrix cracking, and post-flexure fractography provide visual signs of this. In vascular

specimens with coolant flow active at 1.00 $g \cdot s^{-1}$, however, residual ultimate flexural strength was substantially improved at 94 %, *R* was essentially unchanged at approximately 0.98 to 0.99, and visual inspection and fractography both closer resemble an un-aged specimen, further proving the performance retention capability of this vascular cooling concept.

4.3.6 Thermal damage susceptibility of fibre-matrix interphase region

The fractography data also suggests a thermal damage process occurring at the fibre-matrix interface that is either unique to this region and inactive in the bulk matrix, or active in both regions but much more rapid in the former, driving the failure mode transition. Possible explanations for this phenomenon are explored in the following sections, based on current understanding of the fibre-matrix interface and interphase formation.

4.3.6.1 Interphase formation

It is understood that direct chemical reaction between the reinforcement fibre surface and the matrix, or modification of the local matrix chemistry in the vicinity of the fibre, can lead to a region around each fibre where the matrix properties differ from the bulk resin further away. Various fibre sizings (coatings applied to fibres for protection, better handling and improved interfacial properties) and surface treatments (processes that alter the fibre surface itself to promote bonding with the matrix) can also influence this process. The proposed so-called 'interphase' region is very thin at several hundreds of nanometres from the fibre surface, and on the molecular scale a transition from the fibre surface to the bulk matrix polymer exists. Despite the increasing maturity of FRP composites in many industrial sectors, however, understanding of the fibre-matrix interphase is not complete, due to difficulty in its analysis, commercial sensitivity regarding manufacturing processes, and a tendency to focus on the macroscopic view of material behaviour and characterisation.

While the FTIR-ATR equipment used in this work allowed spectra to be collected from the intra-fibre matrix, it did not have the spatial resolution necessary to analyse the much smaller fibre-matrix interphase zone. Therefore, while it was clear from the existing literature and fractographic evidence that this region undergoes a significant weakening upon thermal exposure, identification of the exact mechanisms of this transition, be they chemical, physical or both, was beyond the current experimental capability. What follows is a discussion of the potential mechanisms at play in the context of the experimental observations and results discussed above.

4.3.6.2 Chemical mechanisms

There is good reason to suspect this weakening is partially of a chemical nature, involving the mixture, or stoichiometry, of different molecular components of the matrix system at the

fibre/matrix interphase. In the case of an amine-cured epoxy such as the Hexcel® HexPly® 8552 resin used in this work, these components are epoxy monomers and the amine hardener agent. There exists an ideal stoichiometric ratio of the epoxy and amine components that causes full consumption of both during cure, and theoretically yields the maximum cross-link density. Cross-link density is important to thermo-mechanical performance and thermal ageing, as cross-links restrict polymer chain mobility as temperature rises and secondary inter-molecular bonds begin to break. Where cross-links bond the fibre and matrix at an interface, their density is related to how the interface responds to thermal exposure. Any mechanism that causes a stoichiometric imbalance in this region has the potential impact the interfacial thermo-mechanical properties. It is theorised that this imbalance exists as an interphase region around the fibres as discussed, which may be locally more susceptible to thermal damage, with a corresponding penalty in global laminate residual performance following thermal exposure.

Glass transition temperature is a primary indicator of cross-link density in polymers, as it depends on the degree of polymer chain mobility at a given temperature. Several authors have measured T_g of amine-cured epoxy resins with a range of stoichiometric ratios [77]–[80]. All found that it was reduced when sufficiently far from the ideal ratio of amine to epoxy, in both the epoxy-rich and amine-rich directions. This is a result of reduced cross-link density polymer chain rigidity due to the imbalance of reaction components [80]. In theory a corresponding increase in unreacted components should also occur, and these may be highly susceptible to the chemical decomposition and oxidation reactions that are accelerated by thermal exposure. However, literature regarding the influence of fibre-matrix interphase stoichiometry on susceptibility to thermal ageing in FRP composites is non-existent, so this topic needs much further attention.

4.3.6.3 Physical mechanisms

Glass transition is, by definition, a transition in mechanical properties of a polymer. A reduced T_g in the fibre-matrix interphase will, therefore, cause it to undergo glass transition to the rubbery state at a lower temperature than the bulk matrix. This means that operation of FRP composites below the bulk matrix T_g may still lead to changes in thermo-mechanical performance over various time scales. It also means that once the bulk matrix T_g is reached, glass transition and any associated thermal ageing of the fibre-matrix interphase has already begun and will proceed at a faster rate than in the bulk matrix as temperature is maintained or increased further.

The effects of CTE mismatch between reinforcement fibres and matrix was discussed in Chapter 2. This is certainly a likely candidate for the visible physical degradation via micro-cracking observed in non-vascular specimens, as discussed in Section 4.3.2.1. Several authors found that CTE is minimum

at the stoichiometric ratio of epoxy:amine [78], [80]. This suggests that any imbalance in components in the interphase region would further increase the CTE mismatch between fibre and matrix, potentially causing residual thermal stresses sufficient to initiate matrix micro-cracking and fibre-matrix de-bonding. This pre-existing damage present in non-vascular specimens likely created stress concentrations and damage initiation sites during subsequent flexural testing, and helped give rise to the fibre-matrix interfacial adhesive failure evidenced by the current fractographic evidence, and that from the literature discussed in Chapter 2.

4.3.6.4 Summary

The current theoretical models of the fibre-matrix interphase composition are inadequate, and experimental techniques to analyse this incredibly narrow region are not fully developed. The matter is further complicated by the nature of proprietary fibre sizings and surface treatments applied by manufacturers to gain commercial advantage.

Details of the exact fibre surface treatment and sizing applied to the fibres used in the current experiments were unavailable. Despite this, considering the aerospace quality of the material system, it is likely they have been subjected to both processes with improvement of mechanical properties in mind. Thus, there is clearly potential for non-stoichiometric matrix compositions existing close to the fibre surface in these specimens. Through the reasoning discussed above, this may lead to performance reductions even when operating below the accepted maximum operating temperature of the bulk resin. The fibre-matrix interface will also degrade or decompose more rapidly at a given ageing temperature, with corresponding trends in mechanical performance and fracture behaviour as noted in this work and the literature. This further explains the conservative margins stipulated between T_g and maximum operating temperature for commercial resin systems.

4.3.7 Coolant pumping power

Based on flow pressure measurements made on the specially machined specimen described in Section 4.2.6, the inlet pressure differential and calculated pumping power required to induce each of the tested coolant mass flow rates was found, and is presented in Table 4.4.

Table 4.4: Vascular specimen pressure differential and pumping power requirements at each coolant mass flow rate.

Specimen mass flow rate ($g \cdot s^{-1}$)	Inlet pressure delta before needle (Pa)	Required ideal pumping power (W)	Pumping power areal density ($W \cdot m^{-2}$)
0.27	1500	0.32	77.2
0.53	3900	1.65	392.3
1.00	8400	6.38	1519.3

Clearly, the power required to achieve higher mass flow rates was highly non-linear; a factor of 4 increase between the lowest and highest mass flow rates required approximately 20 times more power. Given that both 0.53 $g \cdot s^{-1}$ and 1.00 $g \cdot s^{-1}$ flow rates performed equally well in preserving residual flexural performance, the almost 300 % increase in power demand demonstrates the need to accurately characterise the flow-thermal-mechanical performance relationships of any vascular component. Precise flow regulation will also be vital to avoid excess pumping power, which has implications on the mass, physical size and fuel consumption of the required pumping system.

4.4 Conclusions

4.4.1 Effect of thermal ageing on non-vascular specimens

Thermal ageing of non-vascular IM7/8552 specimens at 250 °C drove both physical and chemical ageing mechanisms which reduced the residual ambient-temperature mechanical performance in flexure. Non-vascular specimens retained 64 %, 37 % and 18 % of their initial flexural strength after 2 hours, 18 hours and 120 hours of exposure respectively. The primary physical ageing mechanism was matrix micro-cracking, with both inter- and intra-laminar cracks appearing and increasing in density with ageing duration, providing sites for stress concentrations and crack propagation during subsequent flexural testing. These were most likely caused by the CTE mismatch between the carbon reinforcement fibres and polymer matrix, which led to residual stress at the fibre-matrix interface that tended to separate the two by initiating and propagating a crack. A possible visco-elastic mechanism resulting in raising of the stress-free temperature may also lead to abnormally large residual stresses in non-vascular specimens that were exposed to temperatures above T_g. The effect may well be exacerbated by the presence of an interphase regions in the matrix around the fibres, comprising a non-stoichiometric ratio of epoxy to amine hardener, which has been proven to reduce T_g and increase the CTE mismatch between the two constituents.

The susceptibility of the matrix and fibre-matrix interface to such physical thermal degradation was likely aided by continuing chemical thermal decomposition over time. Evidence of oxidation of the TGMDA epoxy component was provided via IR spectroscopic analysis of the matrix near the specimen surfaces. A significant level oxidation of an epoxy component occurred in non-vascular specimens, with the characteristic R ratio reducing by as much as 22 % after 120 hours of ageing. These decompositions may have lowered the strength of the matrix and fibre-matrix interfaces below the thermal residual stress levels during ageing, causing physical degradation via cracking as discussed, and also directly lowered the overall laminate strength upon flexural testing.

Fractographic analysis of specimen failure surfaces via SEM was revealing. Un-aged non-vascular specimens displayed a high concentration of upright cusp features, indicative of a strong,

uncompromised fibre-matrix interface forcing matrix cohesive failure in Mode II interlaminar shear. As ageing duration increased, cusp concentration decreased, and they became shallower, a Mode I-dominated feature and an artefact of the reduced interlaminar shear forces developed by a weakening fibre-matrix interface. This was accompanied by an increase in smooth fibres and corresponding fibre imprints, a result of fibre de-bonding due to weakening of the fibre-matrix interface by thermal exposure.

4.4.2 Thermal ageing mitigation via vascular cooling

Direct comparison between vascular and non-vascular strengths at each condition are complicated by an artificial performance increase (localised variation in fibre volume fraction and displacement from neutral axis) caused by embedding vascules within the laminate; this was likely a geometric effect resulting from laminate structure disturbance by the vascule pre-forming wires. However, under the equivalent heat flux of 3500 $W \cdot m^{-2}$, laminate surface temperature measurements indicated that, at coolant flow rates of 0.53 $g \cdot s^{-1}$ and 1.00 $g \cdot s^{-1}$, specimens remained fully below the manufacturer's recommended maximum service temperature of 121 °C. This corresponds well with the flexural strength data, where performance was essentially steady at around 94 % of the un-aged vascular baseline, following a small initial reduction. Only at 0.27 $g \cdot s^{-1}$ coolant flow did specimen temperatures exceed this threshold, although they remained well below the material dry T_g of 207 °C. A corresponding gradual decrease in flexural strength occurred, reaching 76 % of the un-aged vascular baseline value after 120 hours.

The cooler specimen temperatures reduced the magnitude of thermal residual stresses generated during thermal exposure due to the CTE mismatch between fibre and matrix, and potentially via the stress free temperature reset mechanism proposed in Section 4.3.2.1. Reducing these stresses (combined with improved fibre-matrix interfacial properties as discussed below) prevented the initiation and propagation of the inter- and intra-laminar cracks observed in non-vascular specimens following thermal ageing.

Vascular cooling was found to substantially limit the level of chemical decomposition; at the highest coolant flow rate of 1.00 $g \cdot s^{-1}$ the *R* ratio was unchanged at the coolant inlet end of the specimen, and reduced by just 7 % at the coolant outlet end after 120 hours due to lower temperatures in the matrix material. Some evidence of minor localised decomposition after just 18 hours of ageing at the lowest coolant flow rate of 0.27 $g \cdot s^{-1}$ was observed, supported by specimen surface temperature profiles. This, in agreement with the mechanical testing results, suggests that the critical coolant flow rate for long-term residual flexural strength retention and chemical decomposition mitigation

lies somewhere in the range of 0.27 $g \cdot s^{-1}$ to 0.53 $g \cdot s^{-1}$, for this specific specimen design and thermal environment.

Fractographic analysis of vascular specimens was limited to a single example aged for 18 hours with 1.00 $g \cdot s^{-1}$ coolant flow, due to lab closures following the COVID-19 lockdown. Compared with a non-vascular specimen aged for the same duration, cusps were observed at a higher concentration and more upright angle, indicating a greater level of matrix Mode II cohesive failure, due to larger interlaminar shear forces resulting from a stronger fibre-matrix interface. This significant finding physically proves that vascular cooling can preserve the fibre-matrix interfacial properties under harsh thermal environments. This was manifested in the lack of matrix micro-cracking following ageing of vascular specimens (in combination with the reduction in thermal residual stresses as already discussed), and the higher level of residual flexural strength upon mechanical testing.

The thermal, mechanical, physical and chemical data all verify that the 121 °C limit on operating temperature limit is well-selected to mitigate thermal ageing with a comfortable safety margin. It also exposes the risk in treating T_g as a maximum operating temperature in the absence of any other recommendation, just because this is where the short-term effects of elevated temperature become noticeable. Permanent thermal ageing and performance reduction can occur over time even when the entire component remains well below T_g, as proved by specimens with 0.27 $g \cdot s^{-1}$ coolant flow, and this is an important consideration for designers of vascular and non-vascular FRP composite components alike.

While the sample sizes were low in all analyses, scatter was sufficiently low to identify the trends in the data and make valid comparative conclusions as discussed above. The work presented here successfully met Objectives 2D-E, fully satisfying the scope of Aims 1 and 2. Refer to Chapter 6 for conclusions and discussion of potential future experimental work.

Chapter 5: Numerical modelling

5.1 Introduction

The experimental results presented in this work, building on the existing knowledge, highlight the complex interdependencies between mechanical properties, thermodynamic performance, fluid flow, network topology and manufacturing method. Designing, developing and optimising a vascular FRP composite component for an industrial application purely through experimentation, especially regarding long-term thermal ageing, would be would a prohibitively intensive task. A numerical model can be used to predict the performance of a large variety of designs, validated by a smaller number of physical experiments later in the process. This chapter details the development and validation of a numerical model to predict the thermal performance of an arbitrary vascular network, followed by its utilisation in a basic genetic algorithm optimisation.

5.1.1 Modelling approaches and techniques

The modelling of an FRP composite component with fluid flow through embedded vascules, internal and external heat transfers, and thermo-mechanical responses over various time scales clearly involves multiple physical processes. Hence this can be classified as a multi-physical problem, with the three main physical processes involved in the problem being;

1. The fluid dynamics of the coolant flow, given inlet and outlet conditions and fluid properties.
2. The heat transfers via conduction and convection through the various media and boundaries of the component, both external and internal, and the resulting temperature profile.
3. The thermo-mechanical responses throughout the material, from short-term stiffness and strength to long-term thermal ageing.

In reality, all are incredibly complex, with phenomena such as fluid compressibility and viscosity, laminate anisotropy and non-linear thermo-mechanical mechanisms involved. They could be modelled in fine detail using advanced commercial software running on high performance computers. However, the computing power and time commitment required were all beyond the scope and aims of this project.

Alternatively, the problem can be simplified, and broken down into smaller fragments that can be solved more easily. For example, there are reliable empirical results and relationships to describe how fluid properties change along a circular pipe. Similar simplifications can be made for the thermodynamic aspect of the problem, for example using empirical results for convection from flat plates and within circular ducts.

5.1.2 Prior work

Vascular FRP composite *thermal* performance has been evaluated by a number of authors, both via commercially-available multi-physics software [9], [43], [52], [53], [81], [82] and bespoke user-developed routines [46], [83], [84]. Several methods of optimisation have also been employed, from gradient-descent [46], [82], [83] to genetic algorithms [85]. At the time of writing, the author was unaware of any thermo-mechanical models that predict the temperature profile and expected thermo-mechanical performance or thermal ageing behaviours.

5.1.3 Modelling objectives

The literature and experimental work presented in Chapters 2, 3 and 4 evidenced several physical and chemical processes whose rate were temperature and time dependant, so a prediction of the 3D temperature profile within a component would be vital in the thermo-mechanical design and development of components in industry. Objectives 3A and 3B required a means to simulate the thermal response of a basic vascular FRP composite component, given its geometry, network topology and environment thermal conditions. A reasonably accurate, validated solution was desired in a timely manner, having sufficient fidelity to assess the relative performance of different configurations, and not based on a specific commercial software package.

Objective 3C was to embed the above numerical model into a basic tool to optimise the vascular network, for a given geometry, thermal environment and set of design constraints. Without such a tool, finding the network with the highest performance would be a process of trial and error, as the adjustments to be made to the large number of design variables would likely not be intuitive given the complex interactions between them.

Attempting to couple this thermal response with a prediction of thermo-mechanical performance or thermal ageing was outside the scope of this project. As will be discussed further in Chapter 6, meeting this goal would require intimate knowledge of the changes in modulus, strength and toughness with temperature in a wide range of stress states. This information would most likely be input into an advanced FEA simulation to correctly model damage processes, or a purely statistical model to predict certain material properties based on existing experimental data. Such data is rarely available for FRP composite material systems, so significant effort would first be required in characterising the material of choice and tuning the model to obtain valid results.

5.2 Thermodynamic model development

5.2.1 Software

In order to accelerate development, MathWorks® MATLAB® was chosen to develop the model. MATLAB is a both a proprietary user interface application and programming language that is widely compatible across platforms. It is a so-called 'higher' programming language, meaning it has an additional layer of abstraction that makes its syntax more user-friendly, though slower to execute. The MATLAB code is interpreted and executed by the computer, returning the results in an intuitive, interactive manner to the user.

Contrary to the above objectives, MATLAB *is* a commercial software package, and several built-in functions were used for efficiency. The majority of the code, however, was written to enable easy translation into another programming language that could be compiled and executed with non-commercial software.

5.2.2 Thermodynamic theory

In order to predict the performance of a vascular thermal management system within an FRP composite component, it is necessary to understand how heat energy is transferred across both internal and external boundaries, and within the material itself.

5.2.2.1 Thermodynamic boundary conditions

In any numerical analysis of a system with a large number of unknowns, such as temperatures in 3D space, some set of known physical conditions must be prescribed at the system boundaries, known as boundary conditions. These constrain the problem so that a valid solution may be achieved for the unknown variables, in this case temperatures.

For thermodynamic analyses there exist three common types of boundary condition [68]. In the first, temperature is prescribed along the boundary and remains constant, known as a constant temperature, or Dirichlet, boundary condition. This could represent contact with another component that is in some way temperature-regulated.

The second type is the constant heat flux, or Neumann, boundary condition, in which a prescribed rate of heat flux is set along the boundary and remains constant. This may be relevant for surfaces exposed to electromagnetic radiation of a specific intensity. A special case of this condition is the insulated, or adiabatic, boundary, where heat flux is zero along the boundary.

The third boundary condition is convective, which occurs at a solid-fluid interface. The rate of heat flux through the boundary is determined by a coefficient capturing aspects of the fluid behaviour,

and the temperature difference between the surface and the fluid far away from it. Examples may be fluid impingement on a surface from a nozzle or motion through a fluid media.

5.2.2.2 Internal and external boundary heat transfers

The heat transfer across a boundary is typically stated in terms of heat flux, φ_q; the heat energy passing through a unit area of the boundary surface per unit time, with the units $W \cdot m^{-2}$. For constant temperature boundaries φ_q is irrelevant, as it is not explicitly needed and assumes whatever value is required to maintain the boundary temperature. For constant heat flux boundaries the value of φ_q is set as a constant. Convective boundaries are described by Newton's Law of Cooling:

$$\dot{\boldsymbol{Q}} = \boldsymbol{hA}(\boldsymbol{T} - \boldsymbol{T}_{\infty}) \tag{5.1}$$

where $\dot{Q} = \varphi_q \cdot A$ and is the rate of heat transfer in Watts, W (1 W = 1 $J \cdot s^{-1}$), h is the convective heat transfer coefficient in $W \cdot m^{-2} \cdot K^{-1}$, A is the surface area through which heat is being transferred in m^2, T is the temperature at the surface in K, and T_∞ is the temperature of the fluid well away from the surface in K. For a given surface area and thermal conditions, the rate of heat transfer is governed by h, which depends on many aspects of the fluid flow.

Convection can either be described as free, where the fluid moves solely due to buoyancy forces, or forced, where it is caused to flow over a surface, for example by a fan (also known as advection). The value of h can vary by many orders of magnitude between the two cases, with forced convection yielding much higher values. Other factors such as surface orientation and the development of velocity and thermal boundary layers influence the value of h along a forced convection boundary.

An FRP composite component with an embedded vascular cooling network will have a convective boundary at the vascule wall, but the external boundary conditions will depend on the surrounding environment and structure.

5.2.2.3 Internal laminate heat transfers

Inside the solid laminate, heat energy is transferred solely by conduction, which is the transfer of energy between vibrating atoms. Conduction is described by Fourier's Law:

$$\dot{\boldsymbol{Q}} = -\boldsymbol{kA}\frac{\boldsymbol{dT}}{\boldsymbol{dx}} \tag{5.2}$$

Where $\dot{Q}$ again is the rate of heat transfer in W, k is the material thermal conductivity in $W \cdot m^{-1} \cdot K^{-1}$, A is the surface area through which heat is being transferred in m^2, and dT/dx is the thermal gradient normal to that surface in $K \cdot m^{-1}$.

Isotropic materials have one value for *k* which is valid in all positions and directions. Inhomogeneous, anisotropic materials such as FRP composites, however, have different conductivities in different locations and directions due to their structure of reinforcement and matrix. Polymers typically have very low thermal conductivities, while the reinforcement fibres can vary considerably depending on material. Homogenised, orthotropic thermal conductivities at a ply- or laminate-level can be calculated based on constituent conductivities, volume fractions and stacking sequence, or experimentally-derived values used.

5.2.3 Fluid sub-model

The ultimate aim in the development of this model was to be able to simulate any arbitrary network configuration that may be embedded within an FRP composite material, and potentially find the optimal network configuration given a range of constraints and objectives. The flow along each vascule influences the thermal performance of the network, and may also be an aspect of its optimality, so it must be calculated.

A further simplification can be made if the network is restricted to a rectangular grid pattern; straight lines connecting two known points. This allows the vascular network to be represented as a graph; a concept in discrete mathematics that concerns a group of objects and some information about how they are connected to each other. The known points are called vertices, and the basic information required is the position of each vertex. Vertices can represent inlets and outlets to the vascular network, points at which single vascules change direction (splitting them into two vascules in series) or branches when multiple vascules converge or diverge. Vertices can also be completely disconnected. Restricting the simulation to a 3D rectangular domain with vascules lying on a 2D plane within it, a regular, rectangular grid of vertices can be defined, with different network topologies represented by different vertex connectivity.

Vertices connections are called edges, and the graph connectivity is given in the adjacency matrix *A*, where a value of 1 in position $A_{i,j}$ represents a connection between vertices *i* and *j*:

$$\boldsymbol{A} = \begin{bmatrix} \mathbf{0} & \mathbf{1} & \mathbf{1} \\ \mathbf{1} & \mathbf{0} & \mathbf{0} \\ \mathbf{1} & \mathbf{0} & \mathbf{0} \end{bmatrix} \tag{5.3}$$

For a vascular network, the edges represent the vascules themselves, and diameter must be set either globally or for each vascule individually. Vascule length is determined from its start and end vertex positions. Only connections defined above the main diagonal of the adjacency matrix are required; the values below represent the reciprocal connection between the same vertex pair, but the actual direction of fluid flow is determined separately in the fluids sub-model. With the inlet and

outlet conditions to the network known, the flow that results can be calculated. The model developed in this work made a number of assumptions about the fluid flow:

- The fluid was incompressible, meaning that the volume (and therefore density) of a unit mass did not vary with pressure.
- The fluid properties such as viscosity did not vary with temperature.
- The formation of velocity and thermal boundary layers was ignored.
- Fluid flow is assumed to be in the laminar regime at all times.
- Inlets, outlets, changes in vascule diameter, corners and branches do not cause a pressure drop in the coolant fluid.

Based on these assumptions, the laminar Darcy-Weisbach equation was used to assign a 'stiffness', or resistance to flow, to each vascule:

$$\frac{\Delta \boldsymbol{p}}{\boldsymbol{L}} = \frac{\boldsymbol{128}}{\boldsymbol{\pi}} \cdot \frac{\boldsymbol{\mu \cdot Q}}{\boldsymbol{D^4}} \tag{5.4}$$

where Δp is the pressure differential between inlet and outlet in Pa, L is the vascule length in m, μ is the fluid dynamic viscosity in Pa·s, Q is the volumetric flow rate in $m^3 \cdot s^{-1}$ and D is the hydraulic diameter in m. A global stiffness matrix was assembled for the network, which, along with a vector of known and unknown vertex pressures, forms a system of simultaneous equations. This was solved by inverting the stiffness matrix and multiplying by the pressure vector (achieved by the backslash '\' operator in MATLAB), yielding a vector of known pressures for every vertex. The Darcy-Weisbach equation was used a second time to calculate flow rates and velocities from the differential pressure between each pair of connected vertices.

5.2.4 Thermal sub-model

The thermal sub-model used the finite volume approach to solve the heat transfer problem. The domain was discretised into a mesh of finite rectangular volumes, or cells, inside which the solution, in this case the temperature, was constant. This gave an average solution over the entire cell, but with small enough cells the approximation was valid. In this method a solution exists for the entire domain as it is fully permeated with cells, distinguishing it from the otherwise similar finite difference method, where the domain is discretised into a mesh nodes at which the exact solution is known, but between which must be estimated by interpolation.

The use of finite volumes allowed a system of partial differential equations, subject to the conservation law, to be solved iteratively. Heat energy is transported through a medium via diffusion (flow of heat energy via conduction or convection) or advection (movement of heat energy due to fluid flow), and the portion of this flow that travels through each surface of a cell is known as a flux.

The conservation law states that, in a steady-state thermal equilibrium, the flux leaving a cell through a surface must equal the flux entering the adjacent cell that shares that surface. The magnitude and direction of heat flux between cells was simply calculated based on the heat transfer equations stated in Section 5.2.2, using the thermal gradient and heat transfer coefficient between each cell. A net heat flux into a cell caused a temperature rise in the next iteration of the solution, while a net heat flux out caused a temperature loss.

To allow the true solution to be found, these fluxes were constrained at the domain boundaries. These conditions are often stipulated by the wider context of the problem being simulated, and were set accordingly as discussed in Section 5.2.2.1. An initial guess solution was also provided for the process to iterate from.

This method was employed relatedly by a code that scanned through every cell, calculating the heat flux to or from each of the adjacent cells and updating the cell temperature accordingly. This process sought to reduce all imbalances of heat flux across the domain as much as possible, and when the desired level of reduction was achieved (known as convergence), the resulting stable temperature field represented the steady-state solution.

5.2.5 Description of model operation

5.2.5.1 Pre-processor

A pre-processor function was called once at the start of the code in order to set up the model for the solver. Within this function were a number of sub-functions that handled aspects such as network topology, material and fluid properties, cell mesh construction, heat transfer coefficients, boundary conditions and fluid flow.

5.2.5.2 Advection sub-solver

The advection sub-solver used a backward-difference, or ‘upwind’ finite volume method, solved by Jacobi iteration based on the cell temperatures from the previous iteration. This was necessary to maintain stability, as the advection process concerns the transport of heat energy by a moving fluid from an upstream location to a downstream location. The heat flux into a cell was determined only by the temperature of the cell directly upstream and the flow velocity through the cell.

The only boundary conditions for this process were the vascule inlet temperatures. A new temperature solution was output, with updated vascule fluid cell temperatures.

5.2.5.3 Diffusion sub-solver

The diffusion sub-solver used a centre-difference finite volume method utilising Gauss-Seidel iteration to account for conduction within the laminate and coolant fluid, convection at the laminate-vascule boundaries, and all imposed boundary conditions. Each cell temperature was influenced by all of its neighbouring cells, weighted based on the heat transfer coefficient and the interface area between cells. The laminate cell temperatures from the previous iteration, the updated temperatures from the current iteration and the newly updated fluid cell temperatures from the advection sub-solver were used to compute a new temperature solution for the entire domain, cell by cell.

5.2.5.4 Convergence criterion

The advection and conduction sub-solvers were called continuously until a convergence criterion was met. This required that the spatial average of the error between the current and previous iteration, when normalised by the error between the first two iterations, reduced to a specified tolerance.

5.2.5.5 Post-processor

The post-processor performed calculations on the solution to help quantify its performance, and graphically presented the solution to the user. An example output plot is shown in Figure 5.1.

5.2.6 Model performance

The model ran on a desktop PC without using excessive CPU or memory resources, because the calculations were not computationally intensive being no more than basic arithmetic. The challenge was that these calculations must be performed an enormous amount of times to reach a solution. As a dynamic analysis, the rate of convergence was highly dependent on the time step used between iterations. This was limited by stability criteria for both advection and diffusion processes, limiting the maximum time step to prevent the solution diverging. These criteria were related to the fluid velocity and the laminate thermal diffusivity respectively. Using a low-density gaseous coolant such as air resulted in high velocities to achieve the mass flow rates necessary to provide cooling, and FRP composites typically have low thermal diffusivity due to the polymer matrix, with both resulting in very small maximum time steps. This severely slowed convergence when using representative material properties, requiring in the region of 24 hours to converge for the experimental specimen simulation shown in Figure 5.1.

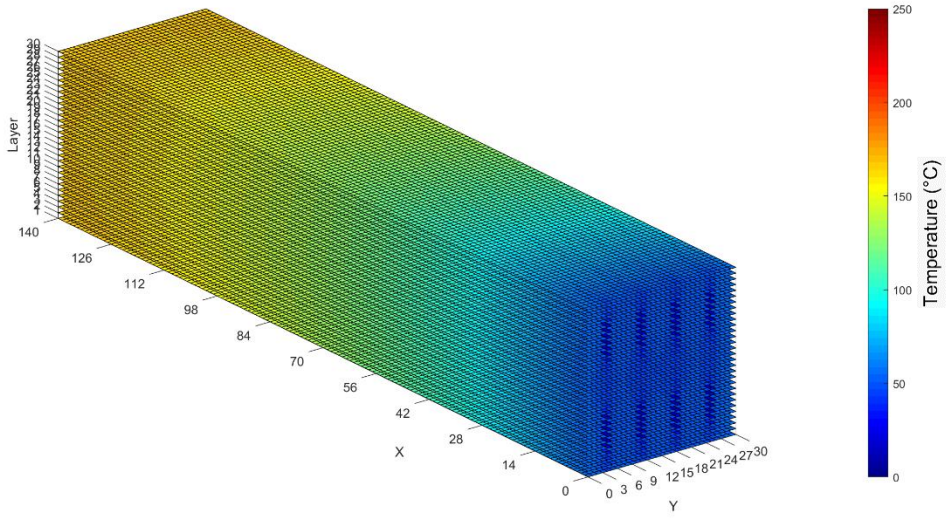

Figure 5.1: Example output of the thermal model when simulating an 8-vascule specimen as tested in Chapter 4. In the MATLAB plot window each ply layer could be removed by clicking on it to reveal the ply layer beneath.

5.2.7 Model validation

5.2.7.1 Experimental dataset

To validate the numerical model, a set of experimental data was required for comparison. One-dimensional thermal profiles were captured along the upper surface of a vascular specimen tested in Chapter 4, at all coolant flow rates. While this was far short of a full three-dimensional thermal profile as output by the model, it was the best validation data available with the current equipment, so it was decided to replicate this experiment within the numerical model. All input conditions were known; specimen geometry, coolant inlet conditions, applied heat flux and material properties.

5.2.7.2 Model input parameters

The nominal specimen geometry of 140 mm × 30 mm × 3.75 mm was input, with a mesh cell size of 1 mm × 1 mm × 0.125 mm yielding a domain of 142 × 32 × 32 cells including the ghost cell layer. This gave a total of 145,408 cells. The stacking sequence was $(+45/90/-45/0_8/+45/90/-45/90)_S$, with each layer assigned properties of IM7/8552 as defined in Table 5.2. Vertices were designated at the nominal inlet and outlet positions of the specimen design, with a vascule diameter of 1.0 mm throughout. A convective boundary condition was applied to the inlet and outlet end surfaces and the side surfaces, with a convection coefficient of 10 $W \cdot m^{-2} \cdot K^{-1}$, a reasonable value for a solid-gas free convection boundary [68]. The upper and lower surfaces were assigned a constant heat flux boundary condition representing the heater mats, each with 1750 $W \cdot m^{-2}$ heat flux into the surface. The coolant inlet temperature was constant at 293 K (20 °C), and the convergence criteria tolerance was 10^{-6}. The initial guess temperature and coolant inlet pressure were altered for each coolant flow rate simulated. Physical properties of air are given in Table 5.3.

5.2.7.3 Results & discussion

When coolant mass flow rates were matched to the experimental values, very good agreement was observed between the experimental and numerical data, as shown in Figure 5.2. Slight discrepancies were observed near the specimen ends, likely due to the fact that the internal heater element wires of the heater mat did no extend right to the heater mat edge, which was not captured in the model, but could be easily accounted for. This result provided confidence that the model could output valid temperature results for different coolant inlet conditions, and that the assumed material and fluid properties were close to the true values. Of course a more comprehensive validation study would be necessary to assess the versatility of the model with different coolant flow regimes and thermal boundary conditions. The current progress represents a good first step that can be taken forwards, with its limitations understood and considered.

Mesh convergence was tested to ensure the current mesh density produced sufficiently accurate results. At the 0.27 $g \cdot s^{-1}$ condition, cell size was halved in the *X* and *Y* directions for a 282 × 62 × 32 mesh with a total of 559,488 cells. The solution was not significantly changed, as illustrated in Figure 5.3, apart from a slight divergence toward the coolant outlet end, with the finer mesh predicting lower peak temperature closer to the experimental data point. This suggested the coarser mesh was adequate to reach an accurate solution, and was conservative in over-predicting peak temperatures.

The thermal model would be no match for the speed, accuracy and certification-level validity of a commercial multi-physics software package. It was, however, a demonstration that useable results can be obtained via a much simpler computational method, one which could easily be re-written in

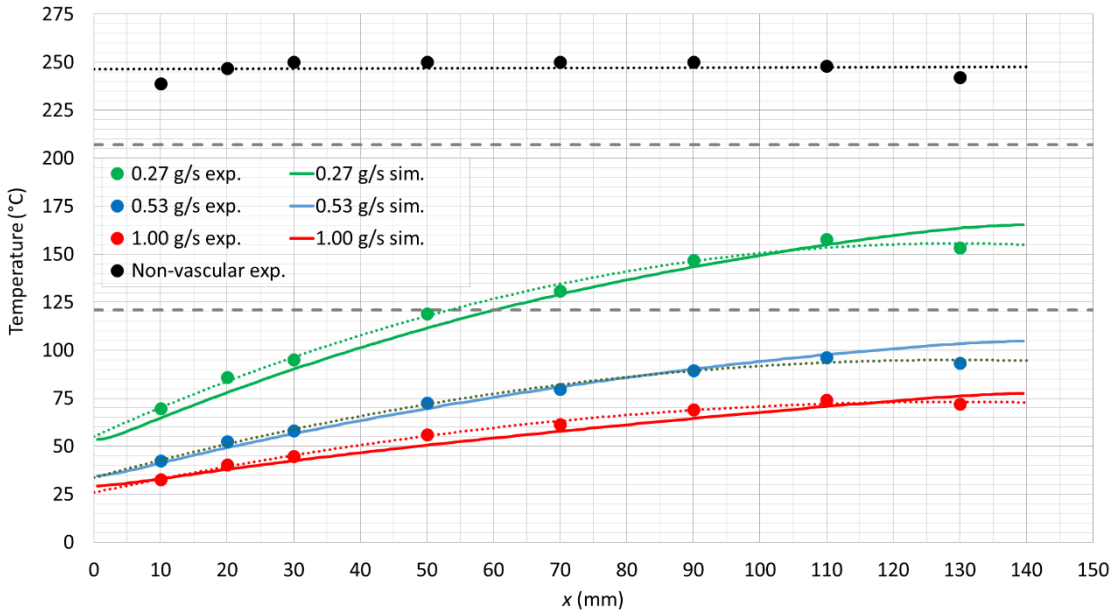

Figure 5.2: Experimental (exp.) and simulation (sim.) surface temperature results for vascular specimens at each coolant flow rate. Material T_g and maximum operating temperatures are denoted by horizontal dashed lines.

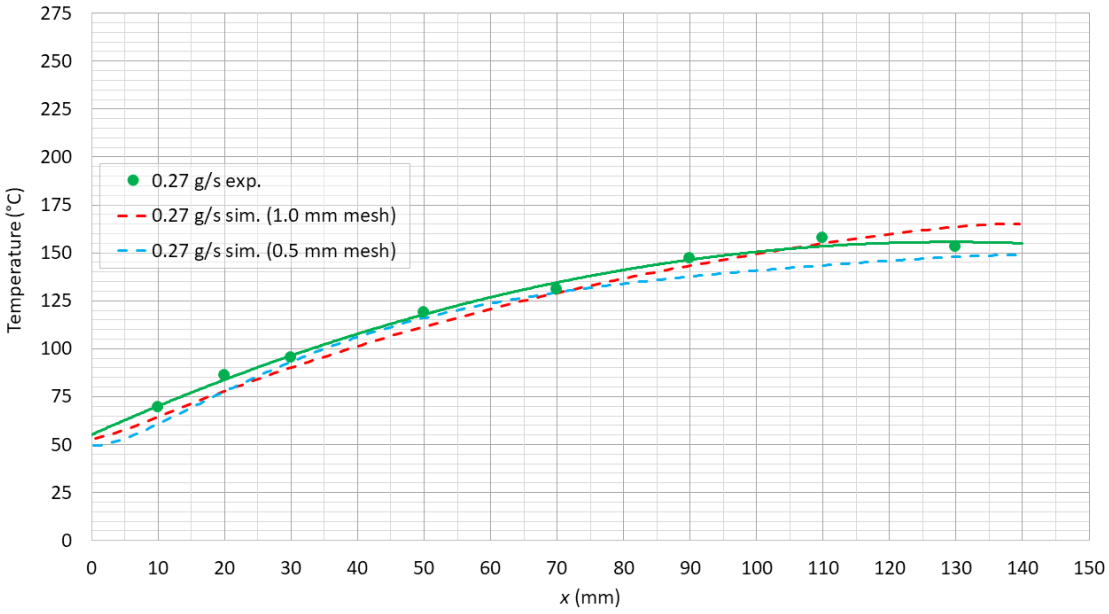

Figure 5.3: Results of mesh convergence study at 0.27 g·s^{-1} coolant flow, compared with experimental results.

any non-commercial programming language. It would be useful for initial comparative design studies, where high accuracy is less important than ease of altering and re-evaluating the design. The design space could thereby be efficiently reduced before committing resources to a more accurate simulation approach or experimentation in the later stages of design.

5.3 Optimiser development

Traditionally, optimisation is the process of seeking the maximum or minimum value of a mathematical function, exploring the design space by varying a number of parameters that represent different features of the system being optimised. In simple problems, the objective function can be expressed as a mathematical equation which is trivial to solve for any combination of optimisation variable values. The objective function of more complex systems, while they may have simple optimisation variables, cannot be easily described by simple equations. In many cases, a numerical simulation must be performed, using some type of model, to generate a result, representing the 'fitness' of the design, which is then maximised.

The aim of the current work was to find, subject to a set of constraints, the network design that yielded the 'best' overall thermal performance. This cannot be calculated via a simple mathematical equation, so the optimiser made use of the thermal simulation code as described in Section 5.2 to evaluate the fitness of each network design.

5.3.1 Network topology genetic algorithm

As previously discussed, networks within a domain are best represented mathematically as matrices where elements represent the existence of a connection between two vertices having defined

locations. There are only two possible states for each connection; connected or disconnected, hence the adjacency matrix is binary.

For this reason, it is not possible to use a gradient-descent approach to optimise vascular network topology; the connection between a pair of vertices cannot be incrementally increased or decreased to ascertain the local gradient of the design space. In other words, the function that describes the performance of a design in terms of the optimisation variables in not differentiable; the concept of a continuous design space is not applicable with discrete optimisation variables such as these.

An alternative approach is the use of a genetic algorithm. This metaheuristic method is based on the representation of the optimisation variables as characteristic genetic information 'bits', in this case elements of an adjacency matrix representing the existence or absence of a vascular connection between a pair of vertices. 'Populations' of individual network topologies, when analysed via the model presented in Section 5.2, would yield a range of thermal profiles. Metrics based on these profiles would provide a measure of the fitness of each network in the context of the optimisation problem. The populations could then be mathematically manipulated via a range of genetic operators to refine the best network designs and produce a set of optimal networks.

5.3.1.1 Initialisation

The first step was to create an initial population of networks, formed by randomly generating binary adjacency matrices. The adjacency matrix represented the connections between vertices arranged in a regular rectangular grid on a square domain, the size and grid spacing of which could be adjusted. This aimed to simulate, on a basic level, some form of flat panel component.

With a considerable number of possible individual network combinations, a series of validity checks were necessary to remove networks that were physically impossible or contained unwanted features. Valid networks required at least one inlet and one outlet, and no disconnected sub-graphs, outlets with no connection to an inlet, self-loops, or vestibular vascules through which no coolant could flow. Networks that passed these checks were assembled into the initial population.

5.3.1.2 Selection

Once the fitness of each solution in the initial population was determined, a sample of these was selected for the following stage of recombination. In order to improve the fitness of each successive generation, the fittest solutions were preferentially picked via roulette-wheel, or fitness proportionate selection. Parent design pairs were randomly sampled from the current generation, weighted by their fitness score, until a pool of parents of the desired size was generated. While this method does have a small probability of selecting poorer designs and missing fitter designs, this is

beneficial as it can allow characteristics to propagate that may contribute to a high fitness design in future.

5.3.1.3 Recombination

Recombination seeks to generate new, high-fitness designs by combining characteristics of parent designs from the previous generation. For the purposes of this optimisation, the genetic 'fingerprint' of each design was the adjacency matrix itself, with the entire matrix reshaped into a vector to form one single 'chromosome', each matrix value providing one 'gene'. A child chromosome was formed by aligning the two parent chromosomes and duplicating genetic information 'bits' sequentially from one. So-called 'crossover', where genetic information duplication is swapped to the other parent chromosome, can occur at any number of points along the chromosome. Single-point crossover was employed in this case, with the crossover point along the chromosome selected randomly for each recombination event. Generated networks were subject to the same validity check as found in the initialisation step.

5.3.1.4 Elitism

In generations containing a relatively small number of high fitness individuals, their beneficial characteristics could be lost during the recombination phase, either due to recombination with a lower fitness design, or not being selected for recombination at all. For this reason, elitist selection was used to clone a small percentage of the highest-performing individuals directly to the next generation, preserving their characteristics.

5.3.1.5 Mutation

Diversity in each generation was maintained by mutating the genetic information of child designs, helping to avoid local minima and stagnation caused by the individuals in the population becoming too similar to one another. A very small probability of mutation was assigned to each genetic information 'bit' after recombination, occasionally producing a slightly different child design that was still mostly representative of its two parents.

5.4 Optimisation case study

5.4.1 Domain geometry and network topology

The case study domain was 120 mm × 60 mm × 3 mm, containing a single mid-plane vascular network with a grid spacing of 30 mm × 15 mm, illustrated in Figure 5.4. For the purposes of this design case, available inlets existed at any of the vertices along the bottom edge of the domain, while available outlets existed at any vertex on the three remaining edges.

A full list of input parameters for the component geometry, network topology constraints and optimisation process is provided in Table 5.3.

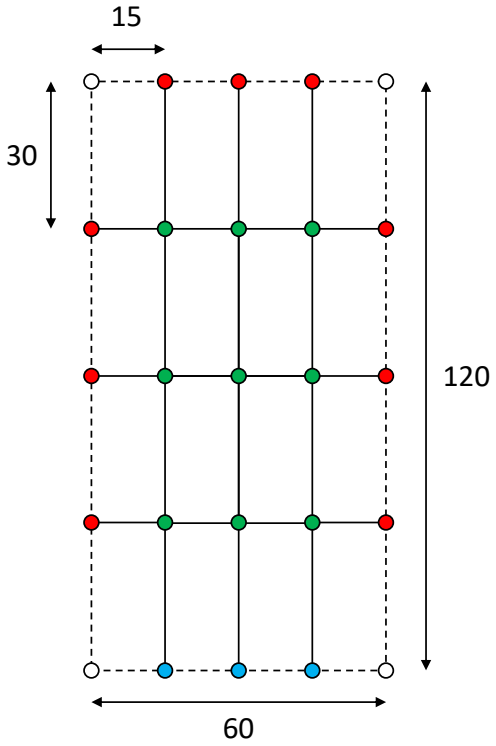

Figure 5.4: Optimisation case study domain and vascular network grid. Solid lines represent valid edges (vascules), dashed lines are invalid edges. Valid coolant inlet vertex (blue), valid coolant outlet vertices (red), valid interior vertices (green) and invalid vertices (white) are marked.

5.4.2 Fitness calculation

At the end of each stage of the optimisation discussed in the following sections, the thermal performance of the generated network designs was evaluated in a parallel loop, utilising the MATLAB Parallel Computing Toolbox to evaluate multiple designs simultaneously across the available processors, reducing the time needed to evaluate the whole population.

Three metrics obtained via the thermal model were selected to represent the fitness of the design in the context of this case study, relating to important system requirements:

A. *Maximum temperature*: The proportion of the domain cells whose temperature was below a specified maximum operating temperature. This related to the probable in-situ short-term thermo-mechanical performance and risk of local incipient heat damage. Ideally all networks that failed to meet this criteria would be rejected, but there was no way to know the result before committing to the thermal simulation. This also highlighted an inherent limitation of genetic algorithm optimisations; they cannot handle objective functions where a pass/fail decision forms part of the fitness score. Instead, it was accepted that any design that scored

less than 1 in this metric would fail the requirement at the specified coolant pumping power level, but networks scoring very close to 1 may meet the requirement with a small increase in pumping power, so these still received a favourable overall fitness.

B. *Average temperature*: The margin between the mean cell temperature across the domain and the specified maximum operating temperature. The results of Chapter 4 indicated that long-term thermal ageing via physical degradation and chemical decomposition can occur even below what many might consider a safe short-term maximum operating temperature. The lower the average component temperature, the longer the service life at that operating condition is likely to be. Designs where the average temperature exceeded this maximum received a negative fitness, virtually disqualifying them in the selection process.

C. *Vascule volume fraction*: The final factor was the proportion of the component volume that was occupied by vascules. This was assumed to relate to residual performance, as components containing a greater volume of vascules would contain less reinforcement fibres, greater stress concentrations and more laminate structure disturbances. This is a gross simplification, as the relationship between mechanical performance and the vascular network topology is complex, depending on vascule orientation with respect to the surrounding fibres and the applied stress state. Nevertheless, vascule volume fraction must be either constrained by rejecting designs above a certain threshold, or low volume fractions must be favoured in the performance calculation.

Optimising each of these three metrics simultaneously would require a multi-objective optimisation approach with decision-making or preference algorithms. Instead, these metrics *A*, *B* and *C*, were combined into a mathematical equation to produce a single fitness score value, reducing the problem to a single-objective optimisation. A network thermal score, *S*, was calculated as follows:

$$\boldsymbol{S} = \left(\frac{\boldsymbol{N_{T \le T_{oper(max)}}}}{\boldsymbol{N_{total}}}\right)^{\boldsymbol{u}} \cdot \left(\boldsymbol{T_{oper(max)} - T_{mean}}\right)^{\boldsymbol{v}} \cdot \left(\frac{\sum_{i=1}^{n}(A_i \cdot l_i)}{l_x \cdot l_y \cdot l_z}\right)^{-\boldsymbol{w}} = \boldsymbol{A^u \cdot B^v \cdot C^{-w}} \qquad (5.5)$$

where $N_{T \le Toper(max)}$ is the number of cells at or below the specified maximum operating temperature $T_{oper(max)}$, N_{total} is the total number of cells, T_{mean} is the mean cell temperature in K, n is the number of vascules, A_i is the cross-sectional area of vascule i in m^2, l_i is the length of vascule i in m, l_x, l_y and l_z are the dimensions of the component in m, and u, v and w are weighting factors applied to each metric to alter their influence on the overall score. Clearly, designs that kept all cells well below the maximum operating temperature with the minimum length of vascules would score the highest. The value of the score was physically meaningless, but networks analysed under the same set of constraints could be directly compared.

5.4.3 Computational efficiency

Obtaining the thermal performance of any network simulated with true FRP composite material properties was time consuming, due to the relative inefficiency of the MATLAB code and the slow convergence rate, as discussed. Analysing hundreds or thousands of candidate network topologies in this way would be a severe bottleneck on the optimisation process. It was found during development of the finite volume code that simulating a material with specific heat capacity, density and thermal conductivity equal to unity significantly accelerated convergence. This hugely increased thermal diffusivity, allowing faster propagation of temperature information through the domain, increasing the maximum time strep and reaching the solution in far fewer iterations. For the purposes of this case study, this adjustment was deemed acceptable, as it would allow a proof of the optimisation approach. There was no temperature-related non-linearity in the simulation due to phenomena such as coolant fluid boiling or polymer melting, so even though the predicted temperatures would be different, the relative performance of each design could be assumed to be the same for this specific problem definition and constraints.

5.4.4 Coolant pumping power constraint

As coolant pumping power was neither an optimisation variable nor part of the fitness score equation, it was constrained. A value of 10 W was selected through a number of thermal model runs to find a value that produced marginal thermal performance in random, un-optimised network designs. The network fluid flow was initially calculated with an inlet pressure of 10 kPa. Due to the linear relationships between coolant inlet pressure, flow rate and pumping power, the characteristic power demand per unit inlet pressure could for that network could then be calculated and used to find the exact inlet pressure that would demand 10 W. This was then substituted as the new inlet pressure, the network fluid flow calculated a second time, and the finite volume thermal simulation initiated to calculate the thermal profile and fitness score. A broad assumption would suggest the networks that exceed the thermal requirements by the largest margin at 10 W pumping power demand would also require the least pumping power to just meet the thermal requirements, if available pumping power was more critical than the need for lowest possible temperatures in the overall system.

5.4.5 Fitness metric weighting

In order to strongly discourage designs with all possible vascules present, which would yield excellent cooling performance but be detrimental to mechanical performance, the weighting factor w was set to 3. Weighting factors u and v were left at 1.

5.4.6 Termination criterion

The termination criterion in genetic algorithms is often unclear, especially with discrete optimisation variables, and is often left to the judgement of the user. Local optimality of the highest-fitness solution could not be proven by incrementally varying the optimisation variables and observing the change in fitness, due to the discrete, binary nature of the genetic information. Longer periods of constant maximum fitness would suggest a local optimum, but again there was no feasible test for global optimality. The only way to be certain that a new, fitter design would not be generated in the very next generation would be to catalogue each generation and terminate the optimisation when every permutation has been analysed. Analysing every permutation in this case study would have been prohibitively time consuming, and no more effective than a simple random or systematic search of the design space. A more suitable approach would be multiple repetitions of a potentially truncated optimisation as performed here, with multiple occurrences of the same fittest solution building confidence in its global optimality.

The process was terminated in this case after 144 generations and not repeated due to the time available, acknowledging this limitation whilst still successfully demonstrating the approach. Nevertheless, the behaviour was as expected, and the average and highest fitness scores of each generation are plotted in Figure 5.5. Occasional increases in maximum fitness occurred when a new more optimal design was generated, between plateaus where elitist selection ensured this design propagated through the subsequent generations. Average fitness showed a general increasing trend as new beneficial characteristics spread through the populations, the gradient reducing after long plateaus in maximum fitness due to the inherent lag of this process.

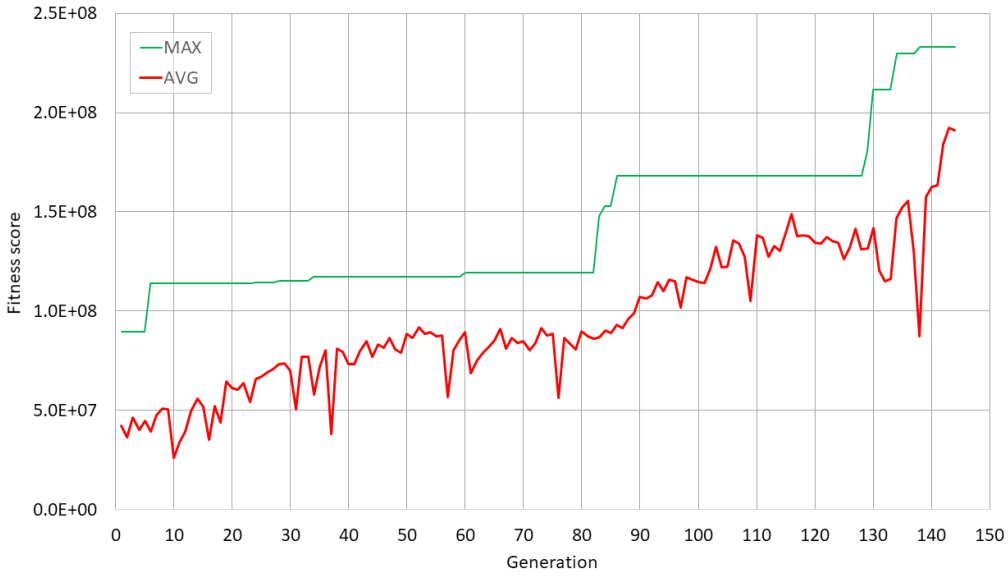

Figure 5.5: Maximum and mean fitness of each generation throughout the optimisation run.

5.4.7 Results and discussion

5.4.7.1 Optimal network designs

The design of maximum fitness in generation 144 is illustrated in Figure 5.6 (#1), with the four next highest fitness designs shown in Figure 5.6 (#2 to #5). Values of *S*, *A*, *B* and *C* for these five fittest network designs are given in Table 5.1. Design #1 scored well due to its low vascule volume fraction and therefore high metric *C*, using only one inlet and few longer longitudinal vascules in favour of shorter transverse vascules to cover the domain. The heavy weighting of metric *C* in the overall fitness score *S* amplified this advantage. The scores in metrics *A* and *B* were middling, but of much lesser influence due to their lower weighting. In fact metric B was only 0.9095, indicating that around 9 % of the domain volume exceeded the defined maximum temperature, failing to meet this temperature requirement at the 10 W pumping power level. Optimality of this design in the problem context would be justified by the small extra pumping power likely required to reach $B = 1$, a worthwhile compromise given the extremely low vascule volume fraction of the design. Compared to the average fitness score of the initial population, which was generated randomly, this design represents an improvement by a factor of 5.53.

The extremely strong influence of metric C, vascule volume fraction, to the overall score can be visualised by plotting the *A*, *B* and *C* metrics of every individual design in three dimensions, as the blue dots in Figure 5.7. Two-dimensional plots of each metric combination are shown with black dots to illustrate the relationships forged by the fitness score equation. The ideal, but physically unattainable, score is marked by a green dot, while the optimal network #1 is represented by the red dot in both the 3D and 2D plots. It is clear that there are a considerable number of designs that out-performed the optimal design in both metrics A and B, yet their lower metric C value limited their overall fitness. The plots show that the optimal design had one of the lowest values of C (these

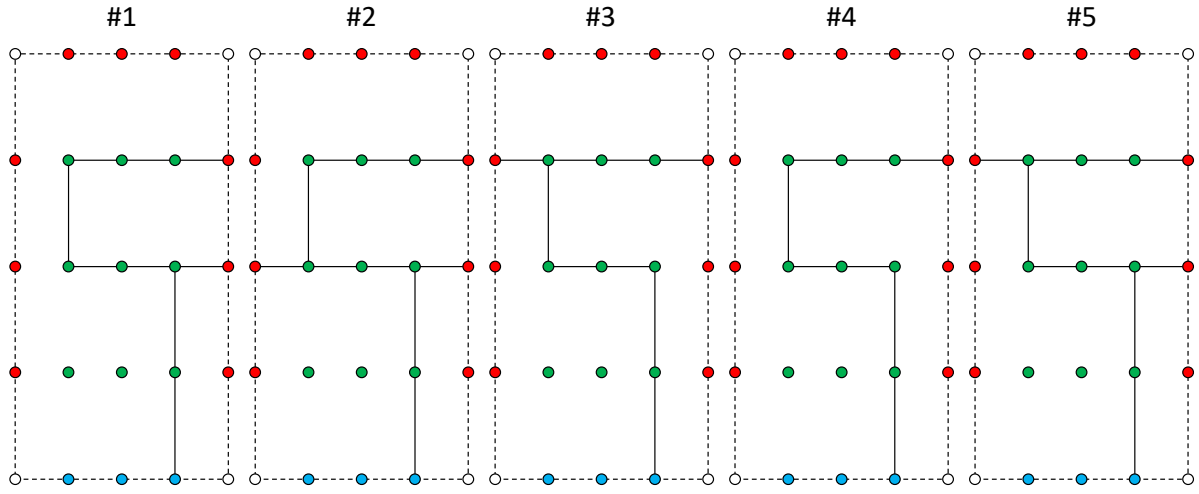

Figure 5.6: Grid diagrams of the five fittest unique network designs at the end of the optimisation run.

appear banded because of the discrete network length possibilities of the grid-based design), hence its dominant overall fitness in this problem context.

Table 5.1: Overall fitness and metrics for the five fittest unique network designs.

Design rank	Overall fitness, *S*	Metric *A*	Metric *B*	Metric *C*
#1	2.3319×10^8	71.886	0.9095	0.0065
#2	2.1326×10^8	80.972	0.9388	0.0071
#3	2.1146×10^8	64.351	0.9213	0.0065
#4	2.0714×10^8	54.092	0.8270	0.0060
#5	2.0667×10^8	78.839	0.9344	0.0071

Figure 5.7 also provides some interesting insights into the relationships between each of the three performance metrics. As was expected, designs with low *B* values also scored poorly in *A*, as the greater proportion of the domain above the maximum temperature limit, the higher the average temperature is likely to be. The cap at $B = 1$ is very evident, but *A* varied widely along the line $B = 1$, showing how the maximum temperature requirement can be met by designs that result in both very high and very low average temperatures. The networks with the highest *A* values exclusively scored $B = 1$, which is also intuitive.

There appears to no particular relationship between *B* and *C*; the lowest *C* scores were obtained with designs scoring both highly and poorly in *B*, and designs achieving $B = 1$ had a wide range of C scores. This proves that cooling the entire domain below the maximum temperature limit can be achieved with relatively low vascule volume fraction if the configuration is optimal. The distribution of points shows how networks with very high and very low vascule volume fractions were less common than those with moderate values around 0.0012, as might be expected.

Comparing metrics *A* and *C* reveals a more interesting relationship. These two metrics are directly conflicting; low average temperature cannot be achieved with a low vascule volume fraction as it will lead to large hotspots, and *vice versa*. This caused an optimal front, where the 'ideal' design cannot be approached any closer because improving one metric comes at the detriment to the other.

It should be noted that the 'ideal' design indicated by the green markers in Figure 5.7 and Figure 5.9 would not be physically possible with a vascule volume fraction of zero. The marker simply indicates the direction within the design space that increases optimality in all aspects.

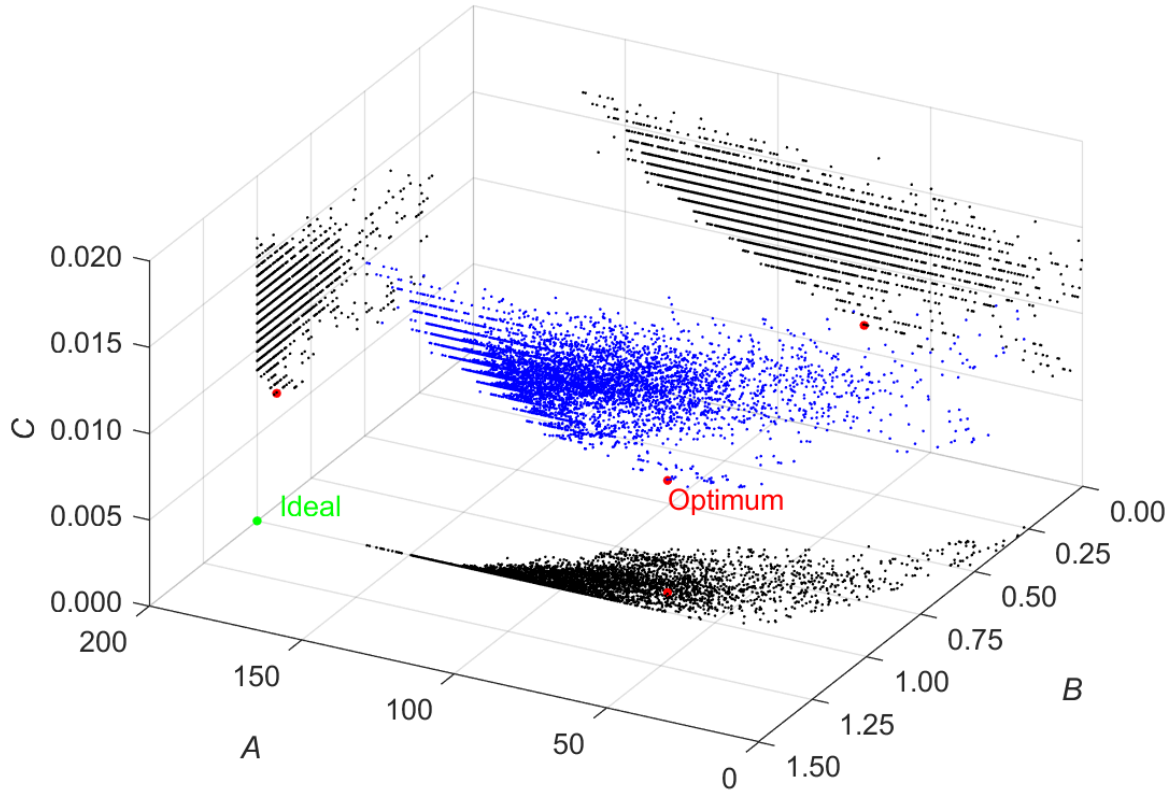

Figure 5.7: 3D scatter plot of all unique network designs showing performance in each of the three metrics within the fitness score equation. 2D plots show performance in each metric combination (black dots). The optimal design (#1) at the end of the optimisation run is marked by a red dot in each plot, and the 'ideal' design by a green dot.

It may seem an invalid conclusion that, in fact, the 15 highest-fitness designs found in this optimisation all failed to score $B = 1$, with a small portion of the domain exceeding the defined maximum temperature at the 10 W pumping power level. If increasing pumping power further were unfeasible, setting this requirement as a criteria for selection of parent designs and/or rejection of child designs during the optimisation would likely have yielded significantly different results. However, repeating the above analysis and plot on the current dataset, with all designs scoring $B < 1$ omitted, the five fittest designs are shown in Figure 5.8 (#1a to #5a), and metrics *A* and *C* of all generated networks are plotted in Figure 5.9. It is clear that these networks fulfil the maximum temperature requirement by adding additional vascules from the central inlet, suggesting that the non-compliant hotspot was previously in the lower left part of the domain, but otherwise they contain similar features and subtle variations found in designs #1 to #5. The optimal front is clear in Figure 5.9, with the design #1a lying on this front, but scoring fairly poorly in metric *A* in order to achieve a very low metric *C* and overall fitness *S*.

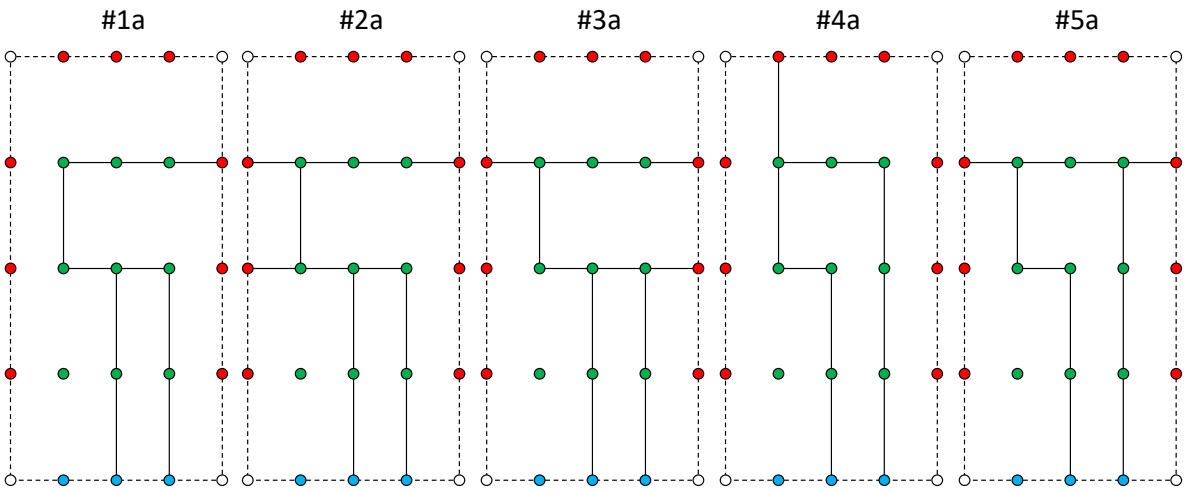

Figure 5.8: Grid diagrams of the five alternative fittest unique network designs achieving *B* = 1 at the end of the optimisation run.

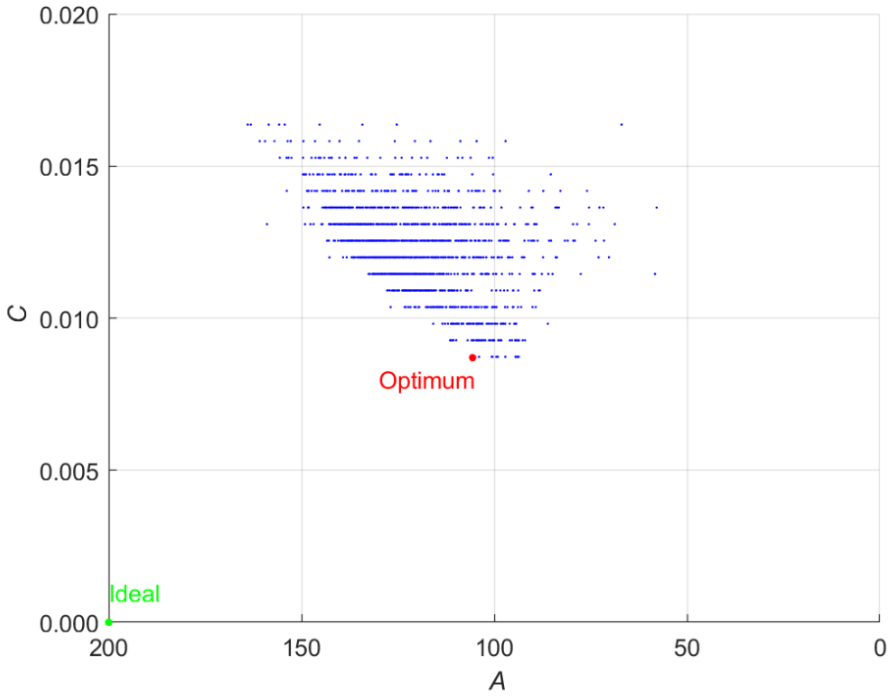

Figure 5.9: 2D scatter plot of all network designs achieving *B* = 1, showing performance in metrics *A* and *C* within the fitness score equation. The alternative optimal design (#1a) at the end of the optimisation run is marked by a red dot, and the 'ideal' design by a green dot.

5.4.7.2 Population diversity

The generation population size of 150 individuals was considered low, as it limited diversity in the initial population and the recombination permutations possible throughout, potentially causing convergence to a local optimum rather than the global optimum of the very large design space. This was considered a necessary compromise with the number of generations processed in the available

time, as processing too few generations could prematurely interrupt the process before an optimum solution was found, local or global.

Diversity was improved via mutation, which randomly altered genetic information as discussed in Section 5.3.1.5. While each genetic chromosome constructed from the adjacency matrix contained 25 × 25 = 625 'bits' available for mutation, the vast majority of these represented invalid vertex connections or impossible vascules. As discussed in Section 5.3.1.1, there are only 24 valid vascules allowed by the problem constraints, each with mutation probability of 0.005 as detailed in Table 5.3, giving a probability of 0.12 that any particular child design would experience mutation. This may be considered too high; there is risk of randomising genetic information faster than recombination can converge on optimal characteristics, known as error catastrophe. Mutation rate could potentially be lowered significantly with a larger generation population, but it produced favourable results in this case study, as average population fitness showed a global increasing trend, recovering quickly from locally poor generations that were likely the result of particularly poor mutated characteristics.

5.4.7.3 Thermal performance verification

It should be stressed that the optimal designs found in this case study are very specific to the problem definition and its constraints. Significantly different results may be obtained by even slight alteration of either, emphasising the importance of careful definition when using this approach. As discussed in Section 5.4.3, linearity of the problem suggests that the optimal designs found above would also provide the relatively best performance in an identical component made of FRP composite, all other parameters being equal. With respect to the thermal requirements of the case study, however, the thermal performance would be completely unacceptable, and this was verified by running design #1 in the thermal model with representative FRP composite material properties. The resulting thermal profile is shown in Figure 5.10, and proves that this network design is nowhere near effective enough to meet the maximum or average thermal requirements.

Clearly the vast majority of the domain is at a temperature well above 300 °C, the defined maximum material limit, with just a small region around the vascules comprising 8 % of the cells experiencing any significant temperature reduction. This is due to the poor thermal diffusivity of the FRP composite material compared to the artificial material used previously, restricting heat transfer within the material resulting in high temperatures. Experience gained from Chapter 4 would suggest that raising vascule inlet pressure, thereby increasing pumping power above 10 W, would provide some additional cooling capacity, but the corresponding gains in performance would become exponentially lower.

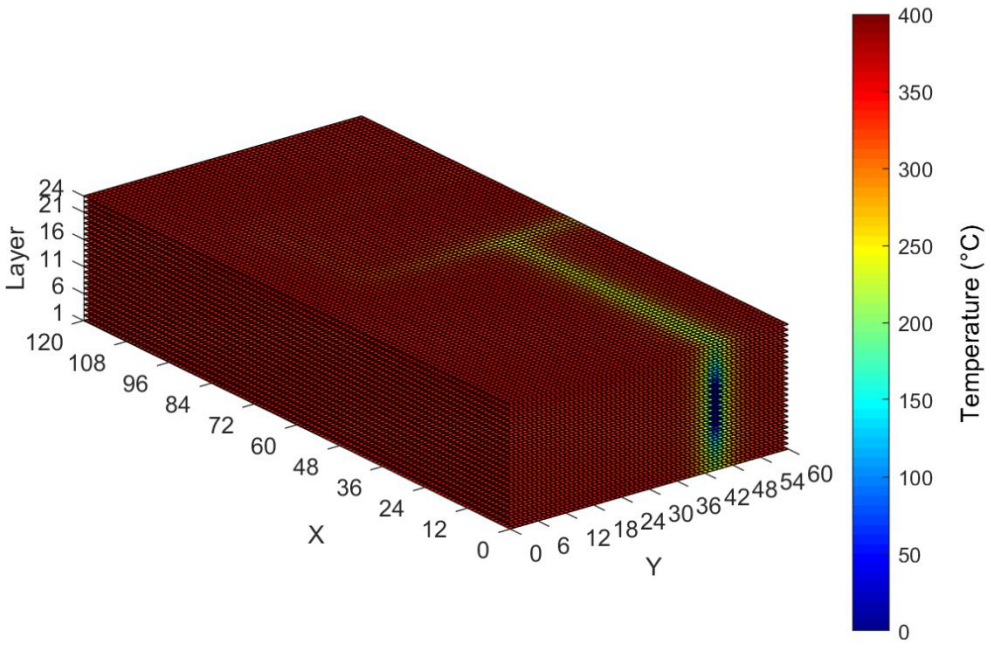

Figure 5.10: Output of the thermal model simulating the optimal design #1 in conditions identical to the optimisation case study, but with material properties representative of an FRP composite laminate.

This means that a different, denser vascular network topology would be required to meet the thermal requirements, something that was strongly discouraged in the optimisation case study by the fitness metric weighting factors, resulting in the relatively sparse optimal networks. If this optimisation were to be repeated with representative material properties, changes to the fitness score weighting would be required, permitting denser network topologies to achieve higher fitness scores and survive through the optimisation process. The pumping power limit may have to be raised substantially, possibly calling into question the viability of the overall system from a mass and energy consumption standpoint. Changes to the grid spacing to permit even denser network topologies, or a shift to a more effective coolant fluid, may then be required. It is this research and understanding that is currently out of practical reach with such slow convergence of the thermal model when using FRP composite material properties. Solving this issue would allow faster thermal performance analyses, and more relevant optimisations that produce viable network topologies for the particular requirements of a representative problem.

5.5 Conclusions

The finite volume thermal model written in MATLAB proved to be a sufficiently accurate method to generate thermal profiles for simple vascular FRP composite panels, as validated against experimental data from Chapter 4. A mesh convergence study confirmed the validity of the simulations. A versatile input format should make this model a useful tool in reducing experimental burden during research and product development activities, especially with further software

development. The main drawbacks were computation speed and convergence rate, requiring around 24 hours to produce a solutions for the flexural specimens as used in Chapter 4. Minimal reliance on proprietary MATLAB functions, however, should enable easy translation into an alternative programming language with better computational efficiency.

The genetic algorithm optimiser approach proved to be an effective method to handle the discrete optimisation variables of a graph-based vascular network topology definition. A case study was constructed, and the developed optimiser and finite volume thermal model worked in unison to generate network designs up to 5.5 times 'fitter' than those that might be expected from a random search. With more available time and improved computing performance, confidence in the global optimality of the results would be increased, but the basic approach is highly versatile and could be of great use in the design and development of vascular FRP composite components. The strong connection between the results and the exact problem definition, requirements and constraints was highlighted, with the 'optimal' network providing very poor performance when simulated with representative material properties. Thermal model convergence improvements would permit better understanding of the practical limits of different network designs, and the influence of performance metrics and weightings, yielding more relevant optimisation results.

Table 5.2: Assumed material properties of IM7/8552 for model validation simulations.

Property		Value
Thermal conductivity	Fibre direction, k_1	6.0 $W \cdot m^{-1} \cdot K^{-1}$
	Transverse direction, $k_2 = k_3$	0.6 $W \cdot m^{-1} \cdot K^{-1}$
Density, ρ		1400 $kg \cdot m^{-3}$
Specific heat capacity, C_p		1250 $J \cdot kg^{-1} \cdot K^{-1}$
Ply thickness, t_{ply}		0.125 mm

Table 5.3: Optimisation case study input parameters. An asterisk * indicates artificial parameters used to accelerate thermal model convergence as discussed.

Component geometry		
Component dimensions		120 mm × 60 mm × 3 mm
Ply thickness		1 mm
Mesh cell dimensions		1 mm × 1 mm × 1 mm
Vascular network topology		
Vertex grid dimensions		30 mm × 15 mm
Vascule diameter		1 mm
Material properties		
Thermal conductivity, k_{lam} (isotropic)*		1.00 $W \cdot m^{-1} \cdot K^{-1}$
Density, ρ_{lam} (isotropic)*		1.00 $kg \cdot m^{-3}$
Specific heat capacity, $C_{p,\,lam}$ (isotropic)*		1.00 $J \cdot kg^{-1} \cdot K^{-1}$
Maximum operating temperature, $T_{oper(max)}$		300 °C
Coolant fluid properties (dry air at 20 °C)		
Thermal conductivity, k_{fluid}		0.02 $W \cdot m^{-1} \cdot K^{-1}$
Density, ρ_{fluid}		1.225 $kg \cdot m^{-3}$
Specific heat capacity, $C_{p,\,fluid}$		1005 $J \cdot kg^{-1} \cdot K^{-1}$
Dynamic viscosity, μ_{fluid}		1.81 × 10^{-5} Pa·s
Inlet temperature, T_{inlet}		20 °C
Thermal environment		
Boundary condition type	upper, lower	Constant heat flux, 1750 W input each
	sides	Convective
Environmental temperature, T_{env}		350 °C
Surface convective heat transfer coefficient, h		10 $W \cdot m^{-2} \cdot K^{-1}$
Optimisation parameters		
Generation population		150
Selected parent pool population		75
Elitist selection rate		0.02 (3 per generation)
Mutation probability rate		0.005 per bit
Fitness metric weight factors	u	1
	v	1
	w	3
Maximum available pumping power, P_{max}		10 W

Chapter 6: Conclusions and Future Work

6.1 Conclusions

6.1.1 Short-term thermo-mechanical performance retention

Specimens of Hexcel® HexPly® IM7/8552 carbon/epoxy were simultaneously heated and tested in four-point bending inside a bespoke thermal test chamber. The maximum environmental temperature of 170 °C was less than desired due to practical limitations of the experimental arrangements, being at the lower end of the matrix glass transition range (dry T_g = 207 °C). This temperature was, however, sufficient to cause 10 % and 21 % reductions in flexural modulus and ultimate flexural strength respectively, in non-vascular specimens, compared to behaviour at 23 °C. Interestingly, even at the material manufacturer's maximum recommended operating temperature of 121 °C, non-vascular specimen performance was reduced by 4 % and 11 % in flexural modulus and strength, indicating that the stated datasheet ambient temperature performance values must not be assumed constant within the material's operating temperature range.

To create vascular specimens, four parallel vascules of 1 mm diameter were embedded at the mid-plane via sandwiching of PTFE-coated wires during lamination, which were manually extracted after cure. This was found to artificially increase both flexural modulus and strength, by 15 % and 6 % respectively at 23 °C. Optical microscopy of sectioned specimens revealed this was likely due to displacement of 0° fibres further from the neutral axis, a by-product of sandwiching the vascule pre-form wire between plies during laminate manufacture.

With environmental temperature at 170 °C, ambient temperature coolant air flowing at 15 $L \cdot min^{-1}$ and taking account of the aforementioned sandwich effect, flexural modulus was not significantly altered, being relatively insensitive to temperature changes. However, flexural strength showed a substantial improvement of 24 % greater than comparative non-vascular specimens at this temperature. In fact, based on the non-vascular specimens, corrected strength was estimated to be equivalent to non-vascular specimens at just 55 °C, a surprising result suggesting that almost full flexural strength retention may be possible with some optimisation. Given that this 'equivalent performance temperature' was below the material maximum operating temperature of 121 °C, cooling capacity was clearly sufficient to yield performance that would be expected well inside the material's normal operating temperature envelope, even when conditions were almost 50 °C above this limit.

6.1.2 Medium- to long-term thermal ageing mitigation

To investigate the effects of medium- to long-term thermal ageing, similar specimens were subjected to thermal exposures at 3500 $W \cdot m^{-2}$ heat input, sufficient to heat non-vascular specimens to 250 °C (T_g + 43 °C), for up to 120 hours. Four-point bending testing at 23 °C followed, and residual ultimate flexural strength reductions of up to 86 % were observed in non-vascular specimens, with visible matrix micro-cracking. Fractographic analysis via SEM revealed incipient heat damage to the fibre-matrix interface increasing with ageing duration, indicated by changes in fracture-induced cusp features. Infrared spectroscopic analysis revealed a thermo-oxidative chemical decomposition mechanism consistent with previous literature.

A two-layer array of eight parallel, 1 mm diameter vascules was embedded in vascular specimens, employing the same wire extraction manufacturing method. Un-aged, zero-flow residual performance was found to be increased by 15 % over non-vascular specimens, again attributed to laminate structure disturbances and fibre displacement from the neutral axis due to the embedded vascule pre-forming wires. This increase rose with ageing duration, for reasons not yet fully understood. Ambient temperature air at mass flow rates of 0.53 $g \cdot s^{-1}$ and 1.00 $g \cdot s^{-1}$ was found to provide maximal cooling performance, with flexural strength initially dropping by around 6 % during the first few hours of ageing, then maintained at a constant level to 120 hours. At 0.27 $g \cdot s^{-1}$ coolant mass flow rate, a continuous gradual reduction in performance occurred with ageing duration, reaching 76 % of the un-aged value after 120 hours. This suggested a non-linearity in cooling capacity with mass flow rate, with the critical point somewhere in the range 0.27 $g \cdot s^{-1}$ to 0.53 $g \cdot s^{-1}$ for this specimen design and thermal environment. Fractographic and IR spectroscopic comparisons showed reductions in both fibre-matrix interfacial incipient heat damage and thermo-oxidative ageing processes in cooled specimens, in accordance with their residual mechanical performance.

6.1.3 Suitability of air as a coolant fluid

It is no surprise that, compared to previous studies where water coolant was used, greater volumetric flow rates were required for measureable performance retention or ageing mitigation when using air. The maximum cooling capacity, however, was deemed to be respectable; peak specimen surface temperatures were between 90 °C and 175 °C lower with active vascular cooling under the thermal ageing conditions discussed above. Due to the low density and viscosity of air, pumping power and parasitic losses are likely to be lower, and with its numerous practical, systems-level benefits, air arguably makes a competitive choice of coolant fluid for industrial applications of the technology.

6.1.4 Numerical modelling and optimisation

The objectives to develop and validate a numerical model were met, with the finite volume thermal model implemented in MATLAB having good agreement with experimental data. The model had a good level of versatility, permitting analysis of arbitrary vascular networks based on a rectangular two-dimensional grid within a rectangular three-dimensional domain. Material and fluid properties, vascule diameter and inlet conditions were all user-definable in order to closely represent the component and conditions desired.

The main issue encountered was slow convergence when using material properties associated with typical FRP composites; the low thermal diffusivity of these materials, mainly due to their low thermal conductivity, forced very small time steps in the dynamic analysis in order to maintain stability of the solution at the model dimensions simulated. This was further exacerbated by the relatively high fluid velocities associated with a gaseous coolant, also enforcing small time steps and consequently more iterations and computation time to converge on a solution. This could be addressed through future software development, as will be discussed in Section 6.2.8 below, but was temporarily mitigated for development purposes by substituting material properties to raise thermal diffusivity and accelerate convergence.

The optimisation case study successfully demonstrated the application of a rudimentary genetic algorithm to the network topology optimisation problem. The network was constrained to a regular rectangular grid for simplicity and compatibility with realistic manufacturing processes, whilst still offering a large number of possible combinations. The allocation of 10 W of pumping power to each design was somewhat arbitrary given the artificial material properties used, but is of the right order of magnitude for the component size concerned based on the previous experimental and numerical results. The small generation size was a necessary compromise with population diversity, but the use of mutation helped avoid stagnation due to self-similarity. Processing more generations in the time available was deemed more important, providing more opportunities for optimisation. Fitness was represented by an equation comprising three performance metrics calculated by the finite volume thermal model, capturing peak and average temperatures and vascule volume fraction. This effectively converted a multi-objective problem into a single-objective optimisation.

After 144 generations an optimum solution was obtained whose fitness was improved over the randomly-generated initial population average fitness by a factor of 5.53. It was impossible to ascertain if this represented a global or local optimum due to the complex problem and discrete optimisation variables, something that multiple optimisation runs would help confirm. Due to mechanical performance concerns, achieving low vascule volume fraction was weighted heavily

compared to meeting peak and average temperature requirements, resulting in optimum designs that fell slightly short of the maximum temperature requirement in order to achieve the lowest vascule volume fraction. Simulating the optimal design with representative material properties yielded very poor thermal performance, suggesting that the fitness metric weightings and pumping power constraint would require adjustment in an optimisation using these material properties.

While the results obtained were very specific to the case study problem and the exact parameters chosen, the methodology followed is generally applicable to the optimisation of any vascular FRP composite component in a harsh thermal environment.

6.1.5 Summary

Overall this project has been successful in satisfying the aims and objectives defined in Chapter 1. While the scope of some experimental elements was reduced due to various challenges, the results gathered make a good case for the viability of this novel concept. Embedded vascules carrying air coolant can, indeed, provide a thermal management functionality to FRP composite materials. Operation was demonstrated near T_g, and under heat flux capable of inducing temperatures above T_g, with almost full in-situ and residual mechanical performance retention. Physical and chemical signs of thermal ageing were also significantly reduced. It is likely that components based on this concept could operate well outside of their recommended thermal envelope, whilst continuing to meet structural requirements over a useful service life. This represents a solid step towards addressing the operating temperature limitation of this material group discussed at the start of this thesis. Valuable additions have been made to the current understanding in a number of fields, including embedding of vascules in FRP composites, physical and chemical behaviour of epoxy-based polymer matrices under thermal exposure (in particular incipient heat damage) and of course performance retention and thermal ageing mitigation via vascular cooling.

6.2 Future Work

6.2.1 Repeats, test matrix resolution & expansion

The present work coarsely varied a few experimental variables; coolant mass flow rate, environmental temperature and ageing duration, and the number of repeats was at the lower end for statistical significance. A logical first step would be repeats of the test conditions from this work, perhaps using more robust heating apparatus to test repeatability. The specimens tested in Chapter 3 could also benefit from the chemical and fractographic analyses employed in Chapter 4, perhaps revealing different behaviours caused by failure after exposure to elevated temperature compared to at ambient.

Following this, a finer and wider variation of the two experimental variables would help complete understanding. In the case of in-situ thermo-mechanical testing, as per Chapter 3, a more versatile and reliable thermal chamber would permit testing at more temperature conditions, including those above T_g and well into the region of incipient heat damage. Finer variation of thermal ageing duration as per Chapter 4 would help define ageing curves at different coolant flow rates, and longer durations may be more representative of true component service life. Further increasing the heat flux applied to vascular specimens of IM7/8552 may be of interest to stress the vascular cooling system, but of little added value in comparison with non-vascular specimens, as the latter would experience temperatures even further beyond the maximum operating point. For valid, useful material data, non-vascular specimens should be limited to temperatures up to T_g, and a correspondingly lower limit on heat flux or a fixed surface temperature boundary condition applied for direct comparison with vascular specimens.

6.2.2 Combination with high-temperature resin system

To truly extend the thermal performance envelope of FRP composites as a material group, it would be far more sensible to select a resin system that already possesses excellent high temperature performance, both in terms of higher T_g and resistance to thermal ageing mechanisms. Polyimides and bismaleimides are two such thermo-setting polymers, which can be safely used at temperatures exceeding 200 °C. There are also high-temperature thermo-plastic resins such as poly-etheretherketone (PEEK) or poly-etherketoneketone (PEKK) which melt at over 300 °C. Composites based on these resins may have new or different responses to high temperature operation over the different time scales, due to their precise physical and chemical natures, which must be understood. In particular, chemical and fractographic analyses may reveal specific understanding about the fibre-matrix interface/interphase behaviour and fracture mechanisms. The thermal envelope and service life improvements yielded by vascular cooling may then be properly evaluated.

6.2.3 Transient performance

The present experiments have all considered steady-state thermal conditions only, but many applications of this technology may involve more rapid temperature changes. The ability of the vascular cooling system and any control logic to react to these effectively must be assessed.

6.2.4 Coolant fluid trials

While air proved to be a reasonably effective coolant fluid in this work, more thermally demanding applications may necessitate a switch to a liquid coolant. The practical, system-level limitations of water based coolants have already been discussed, so liquids that mitigate these issues should be

investigated. Freezing point can be lowered by mixing with glycols, as is done in internal combustion engine coolant, while an oil-based liquid may avoid electrical shorts in the event of leakage. Fluid absorption into the matrix is an important issue, and a separate research on fluid thermodynamic properties and compatibility with different polymers will be required. The concept of multi-functionality within the coolant fluid itself may also be worth exploring; a coolant that also performs some other function within the wider system or vehicle. In modern gas turbine engines, pre-heating of cold fuel from aircraft wing tanks prior to combustion is achieved by simultaneously cooling the lubricating oil via a heat exchanger. One could envisage an FRP component exposed to a hot environment, cooled by circulating fuel through vascules on its way to a combustion system. With the move away from hydrocarbon based fuels to alternatives such as hydrogen, new possibilities beckon for active thermal management of structural components.

6.2.5 Manufacturing route investigation

As already stated, the manual wire extraction vascular manufacturing method used in this work was sufficient for small-scale experiments, but would be inadequate in a production environment, being reliant on manual exertion and unable to produce complex network topologies. It also produced geometrical laminate disturbances that artificially influenced mechanical performance. An ideal process should be fully automatable, removing human effort and error, and consistently produce high quality parts with minimal defects. While the VaSC technique detailed in Chapter 2 has been demonstrated to create much more complex network topologies, and is compatible with the 3D weaving/resin infusion process, further improvements are necessary. In particular damage caused by the long, high temperature post-cure step to vaporise the PLA filament must be investigated, and mitigated if possible. It is also only compatible with material systems where the peak cure or processing temperature is below the filament vaporisation temperature. There is clearly much further work to be done in this area, and efforts would benefit from co-ordination with the largely parallel technology of vascular self-healing, which utilises the same basic manufacturing concepts.

6.2.6 Industrially-focussed demonstrator

Once more of the above investigations have been completed, the specific applications of the technology with the highest feasibility would be clearer. At this point, proof of concept studies should be undertaken by fabricating component-level demonstrators. More representative operating conditions can be introduced, and the integration with the coolant supply system can be developed. For true ‘active’ thermal management, some level of temperature sensing, feedback and coolant flow control could also be incorporated, perhaps with some level of blockage or damage tolerance logic. The manufacturing process can then also be scaled up from one-off components to small batches via development of specific tooling and automation.

6.2.7 Vascular heating

The present work has considered cooling of FRP composite exposed to *hot* environments, due to the deleterious effects elevated temperature has on a polymer itself and its performance as a composite matrix. The effects of moderate sub-ambient temperatures on FRP composites are generally of less concern; the matrix simply moves further into the glassy region, with modulus increasing and toughness decreasing gradually. Extremely low cryogenic temperatures can, however, cause issues via the same thermal expansion coefficient mismatch and micro-cracking mechanisms discussed in Chapter 4. In addition, FRP composites may be employed in components that must be kept warm for other reasons. Ice formation is probably chief amongst these; it can severely disturb the aerodynamics of aircraft wings and the blades of turbofan engines and wind turbines. There is no physical reason why vascular *heating* could not be employed by circulating a warm fluid through the network, dissipating its heat into the laminate and thereby raising temperature, limiting thermal residual stresses or melting accumulated ice. Finding a source for this heat in a mechanical system or vehicle should be simple, as heat engines, transmissions, batteries and electronics all produce waste heat. Pumps and compressors undesirably heat their working fluid, so a vascular composite component may also function as a structural heat exchanger.

6.2.8 Numerical modelling

The slow convergence rate of the numerical thermal model would likely be improved by further specialised software development. It is possible that there are advanced mathematical and coding techniques that could significantly reduce both the time taken to compute each iteration of the solution, but also require fewer iterations to reach convergence. The basic finite volume method is simple, but involves extremely high numbers of repetitive calculations. Methods to perform these in parallel, such as red-black ordering, the built-in vectorisation capabilities within MATLAB and better variable management are a few potential examples. By far the biggest improvement in speed, however, would likely come from replicating the algorithm in a coding language that does not use the speed-limiting layer of abstraction that makes MATLAB code so intuitive to write and de-bug. A model directly coded in C, for example, would circumvent the code interpretation process and likely yield significant performance improvements, enabling the efficient simulation of models with realistic material properties.

Another task for the numerical model will be the important analysis of fault tolerance. Vascules are susceptible to blockage from foreign debris or leakage due to damage to the surrounding laminate, with the possible scenarios being incredibly complex and numerous. Investigating the ability of the cooling network to tolerate these situations would be a simple simulation task, but the results would be vital in developing reliable components that can be certified in safety-critical applications.

Developing a full thermo-mechanical material model to predict laminate performance and ageing behaviour at elevated temperature would require extensive material characterisation work. Over-simplifying the strength properties and damage behaviour of FRP composites through statistical models or linear analyses would fail to capture the high level of complexity involved. The modelling process is probably best approached, therefore, through advanced non-linear finite element analysis, with damage prediction capabilities such as cohesive zones.

Regarding the genetic algorithm optimiser, the basic approach could easily be applied to future optimisation problems with little to no extra development. The fitness score equation devised was basic but captured thermal and vascule volume fraction aspects well, and missing metrics relating to manufacturing complexity, thermo-mechanical performance or other measures of optimality could be included easily in future. While slight tuning of some aspects of the genetic operations could improve performance in specific problems, the physical validity of the result is based on the validity of the thermal model, or indeed whatever method is used to calculate fitness score. Development of the thermal model could take place relatively independently, simply ensuring the input/output formats remains compatible. Likewise, greater versatility in the thermal model to handle more complex geometries, fluid flow regimes and network topologies could easily be supported in the optimiser code. As with the thermal model, computational efficiency could be improved by translating the code to an alternative programming language, but making use of parallel computing in this case may require more advanced software development. These steps, along with use of more powerful computing hardware, would allow the larger population sizes, generation counts and repeats required to be sufficiently confident of global optimality.

References

[1] United Nations, “The Sustainable Development Goals Report 2020,” 2020.

[2] N. . Hancox, “Thermal effects on polymer matrix composites: Part 2. Thermal degradation,” *Mater. Des.*, vol. 19, no. 3, pp. 93–97, Jun. 1998.

[3] V. V. Vasiliev and E. V. Morozov, *Mechanics and Analysis of Composite Materials*. Elsevier Science Ltd, 2001.

[4] Y. Tanabe *et al.*, “The strength of pitch-based carbon fibre at high temperature,” *J. Mater. Sci.*, vol. 26, no. 6, pp. 1601–1604, 1991.

[5] E. U. Chowdhury *et al.*, “Mechanical Characterization of Fibre Reinforced Polymers Materials at High Temperature,” *Fire Technol.*, vol. 47, pp. 1063–1080, 2011.

[6] S. Cao *et al.*, “Tensile Properties of CFRP and Hybrid FRP Composites at Elevated Temperatures,” *J. Compos. Mater.*, vol. 43, no. 4, pp. 315–330, Feb. 2009.

[7] Y. Bai and T. Keller, “Modeling of strength degradation for Fiber-reinforced polymer composites in fire,” *J. Compos. Mater.*, vol. 43, no. 21, pp. 2371–2385, 2009.

[8] J. R. Correia *et al.*, “Mechanical behaviour of pultruded glass fibre reinforced polymer composites at elevated temperature: Experiments and model assessment,” *Compos. Struct.*, vol. 98, pp. 303–313, 2013.

[9] A. M. Coppola *et al.*, “Retention of mechanical performance of polymer matrix composites above the glass transition temperature by vascular cooling,” *Compos. Part A*, vol. 78, pp. 412–423, 2015.

[10] E. Kandare *et al.*, “Thermo-mechanical responses of fiber-reinforced epoxy composites exposed to high temperature environments. Part I: Experimental data acquisition,” *J. Compos. Mater.*, vol. 44, no. 26, pp. 3093–3114, 2010.

[11] D. K. Rathore *et al.*, “In-situ elevated temperature flexural and creep response of inter-ply glass/carbon hybrid FRP composites,” *Mech. Mater.*, vol. 105, pp. 99–111, 2017.

[12] L. E. Asp, “The effects of moisture and temperature on the interlaminar delamination toughness of a carbon/epoxy composite,” *Compos. Sci. Technol.*, vol. 58, no. 6, pp. 967–977, 1998.

[13] G. Charalambous *et al.*, “Temperature effects on mixed mode I/II delamination under quasi-

static and fatigue loading of a carbon/epoxy composite," *Compos. Part A*, vol. 77, pp. 75–86, 2015.

[14] T. Gaile, "Effect of Thermal Shocks on Mode II Fracture Toughness of Fibre Reinforced Polymer Composites," Masters Thesis, Imperial College London, 2016.

[15] S. J. Ng *et al.*, "Charaterization of IM7/8552 Polymer Composites Subjected to Heat Damage," in *29th International SAMPE Technical Conference*, 1997, pp. 776–786.

[16] R. Ong and C. H. Wang, "Effect of Incipient Heat Damage on the Fatigue Properties of Aircraft Composites," in *8th Structural Integrity and Fracture*, 2013.

[17] D. E. Bowles and S. S. Tompkins, "Prediction of Coefficients of Thermal Expansion for Unidirectional Composites," *J. Compos. Mater.*, vol. 23, no. 4, pp. 370–388, Apr. 1989.

[18] T. K. Tsotsis, "Thermo-Oxidative Aging of Composite Materials," *J. Compos. Mater.*, vol. 29, no. 3, pp. 410–422, 1995.

[19] T. K. Tsotsis, "Long-term thermo-oxidative aging in composite materials: Experimental methods," *J. Compos. Mater.*, vol. 32, no. 11, pp. 1115–1135, 1998.

[20] T. K. Tsotsis and S. M. Lee, "Long-term thermo-oxidative aging in composite materials: failure mechanisms," *Compos. Sci. Technol.*, vol. 58, pp. 355–368, 1998.

[21] J. Wolfrum *et al.*, "Rapid evaluation of long-term thermal degradation of carbon fibre epoxy composites," *Compos. Sci. Technol.*, vol. 69, no. 3–4, pp. 523–530, 2009.

[22] S. Bondzic *et al.*, "Chemistry of thermal ageing in aerospace epoxy composites," *J. Appl. Polym. Sci.*, vol. 100, no. 3, pp. 2210–2219, 2006.

[23] B. Dao *et al.*, "Accelerated aging versus realistic aging in aerospace composite materials. II. Chemistry of thermal aging in a structural composite," *J. Appl. Polym. Sci.*, vol. 102, no. 4, pp. 3221–3232, 2006.

[24] S. Eibl, "Observing inhomogeneity of plastic components in carbon fiber reinforced polymer materials by ATR-FTIR spectroscopy in the micrometer scale," *J. Compos. Mater.*, vol. 42, no. 12, pp. 1231–1246, 2008.

[25] J. Wolfrum *et al.*, "Damage initiation of thermally degraded carbon composites in tension," *J. Compos. Mater.*, vol. 52, no. 24, pp. 3399–3409, 2018.

[26] S. Eibl and J. Wolfrum, "Prospects to separately estimate temperature and duration of a

thermal pre-load on a polymer matrix composite," *J. Compos. Mater.*, vol. 47, no. 24, pp. 3011–3025, 2013.

[27] S. Eibl, "Reliable and universally applicable chemometric techniques based on infrared spectroscopy to non-destructively quantify thermal damage of carbon fibre reinforced epoxy matrix composites," *Polym. Test.*, vol. 76, no. March, pp. 396–410, Jul. 2019.

[28] Y. M. Pei *et al.*, "Thermal-oxidative aging of DGEBA/EPN/LMPA epoxy system: Chemical structure and thermal-mechanical properties," *Polym. Degrad. Stab.*, vol. 96, no. 7, pp. 1179–1186, 2011.

[29] K. Boba, "Development of Vascular Networks for Thermal Management in FRP Composites," Ph.D Thesis, University of Bristol, 2016.

[30] K. Boba *et al.*, "Development of Embedded Vascular Networks in FRP for Active / Passive Thermal Management," University of Bristol, 2015.

[31] N. . Hancox, "Thermal effects on polymer matrix composites: Part 1. Thermal cycling," *Mater. Des.*, vol. 19, no. 3, pp. 85–91, Jun. 1998.

[32] W. K. Goertzen and M. R. Kessler, "Creep behavior of carbon fiber/epoxy matrix composites," *Mater. Sci. Eng. A*, vol. 421, no. 1–2, pp. 217–225, 2006.

[33] P. K. Dutta and D. Hui, "Creep rupture of a GFRP composite at elevated temperatures," *Comput. Struct.*, vol. 76, no. 1, pp. 153–161, 2000.

[34] M.-U. Saeed *et al.*, "Manufacturing strategies for microvascular polymeric composites: A review," *Compos. Part A*, vol. 78, pp. 327–340, 2015.

[35] J. C. Watson, "Hollow Glass Fibres in Aerospace," Ph.D Thesis, University of Bristol, 1997.

[36] M. Hucker *et al.*, "Optimisation of hollow glass fibres and their composites," *Adv. Compos. Lett.*, vol. 8, no. 4, pp. 181–189, 1999.

[37] S. M. Bleay *et al.*, "A smart repair system for polymer matrix composites," *Compos. Part A*, vol. 32, no. 12, pp. 1767–1776, 2001.

[38] A. Kousourakis *et al.*, "Interlaminar properties of polymer laminates containing internal sensor cavities," *Compos. Struct.*, vol. 75, pp. 610–618, 2006.

[39] A. Kousourakis *et al.*, "Tensile and compressive properties of polymer laminates containing internal sensor cavities," *Compos. Part A*, vol. 39, pp. 1394–1403, 2008.

[40] A. Kousourakis and A. P. Mouritz, “The effect of self-healing hollow fibres on the mechanical properties of polymer composites,” *Smart Mater. Struct.*, vol. 19, no. 8, p. 085021, 2010.

[41] D. M. Phillips *et al.*, “Mechanical and thermal analysis of microvascular networks in structural composite panels,” *Compos. Part A*, vol. 42, pp. 1609–1619, 2011.

[42] M. R. Pierce, “Microvascular Heat Transfer Analysis in Carbon Fiber Composite Materials,” M.Sc Thesis, University of Dayton, 2010.

[43] S. J. Pety *et al.*, “Active cooling of microvascular composites for battery packaging,” *Smart Mater. Struct.*, vol. 26, no. 10, p. 105004, 2017.

[44] H.-W. Huang *et al.*, “Predicting effects of blood flow rate and size of vessels in a vasculature on hyperthermia treatments using computer simulation,” *Biomed. Eng. Online*, vol. 9, no. 1, p. 18, 2010.

[45] C. J. Norris *et al.*, “Interactions between propagating cracks and bioinspired self-healing vascules embedded in glass fibre reinforced composites,” *Compos. Sci. Technol.*, vol. 71, pp. 847–853, 2011.

[46] M. W. McElroy *et al.*, “Optimisation of an air film cooled CFRP panel with an embedded vascular network,” *Int. J. Heat Mass Transf.*, vol. 88, pp. 284–296, 2015.

[47] R. S. Trask and I. P. Bond, “Bioinspired engineering study of Plantae vascules for self-healing composite structures,” *J. R. Soc. Interface*, vol. 7, pp. 921–931, 2010.

[48] C. J. Norris *et al.*, “The role of embedded bioinspired vasculature on damage formation in self-healing carbon fibre reinforced composites,” *Compos. Part A*, vol. 42, no. 6, pp. 639–648, 2011.

[49] A. P. Esser-Kahn *et al.*, “Three-dimensional microvascular fiber-reinforced composites,” *Adv. Mater.*, vol. 23, pp. 3654–3658, 2011.

[50] A. M. Coppola *et al.*, “Survival of actively cooled microvascular polymer matrix composites under sustained thermomechanical loading,” *Compos. Part A*, vol. 82, pp. 170–179, 2016.

[51] A. M. Coppola *et al.*, “Active Cooling of a Microvascular Shape Memory Alloy-Polymer Matrix Composite Hybrid Material,” *Adv. Eng. Mater.*, vol. 18, no. 7, pp. 1145–1153, 2016.

[52] S. J. Pety, “Microvascular Composites As a Multifunctional Material for Electric Vehicles,” Ph.D Thesis, University of Illinois, 2017.

[53] S. J. Pety *et al.*, “Carbon fiber composites with 2D microvascular networks for battery cooling,” *Int. J. Heat Mass Transf.*, vol. 115, pp. 513–522, 2017.

[54] S. J. Pety *et al.*, “Effect of microchannels on the crashworthiness of fiber-reinforced composites,” *Compos. Struct.*, vol. 184, pp. 428–436, 2018.

[55] J. F. Patrick *et al.*, “Robust sacrificial polymer templates for 3D interconnected microvasculature in fiber-reinforced composites,” *Compos. Part A*, vol. 100, pp. 361–370, 2017.

[56] A. R. Najafi *et al.*, “Microvascular composite skin panels for hypersonic aircraft,” in *55th AIAA/ASME/ASCE/AHS/ASC Structures, Structural Dynamics, and Materials Conference*, 2014.

[57] K. Boba *et al.*, “Novel Manufacturing Method for FRP Composites With a Multifunctional Vascular Network,” in *4th International Conference on Self-Healing Materials*, 2013, pp. 388–391.

[58] C. Huang, “Preliminary study on embedded vasculatures in self-healing FRP composite laminates,” Ph.D Thesis, Univeristy of Bristol, 2010.

[59] C. Huang *et al.*, “Characterization and analysis of carbon fibre-reinforced polymer composite laminates with embedded circular vasculature,” *J. R. Soc.*, pp. 1229–1241, 2010.

[60] M.-U. Saeed *et al.*, “Mechanical effects of microchannels on fiber-reinforced composite structure,” *Compos. Struct.*, vol. 154, pp. 129–141, 2016.

[61] A. T. T. Nguyen and A. C. Orifici, “Structural assessment of microvascular self-healing laminates using progressive damage finite element analysis,” *Compos. Part A*, vol. 43, no. 11, pp. 1886–1894, 2012.

[62] D. J. Hartl *et al.*, “Effects of microchannels on the mechanical performance of multifunctional composite laminates with unidirectional laminae,” *Compos. Struct.*, vol. 143, pp. 242–254, 2016.

[63] A. M. Coppola *et al.*, “Tensile properties and damage evolution in vascular 3D woven glass/epoxy composites,” *Compos. Part A Appl. Sci. Manuf.*, vol. 59, pp. 9–17, 2014.

[64] R. S. Trask *et al.*, “Bioinspired self-healing of advanced composite structures using hollow glass fibres,” *J. R. Soc. Interface*, vol. 4, no. 13, pp. 363–371, 2007.

[65] R. Luterbacher *et al.*, “Static and fatigue tensile properties of cross-ply laminates containing vascules for self-healing applications,” *Smart Mater. Struct.*, vol. 25, no. 1, 2015.

[66] G. J. Williams *et al.*, “Compression after impact assessment of self-healing CFRP,” *Compos. Part A Appl. Sci. Manuf.*, vol. 40, no. 9, pp. 1399–1406, 2009.

[67] B. D. Kozola *et al.*, “Characterization of active cooling and flow distribution in microvascular polymers,” *J. Intell. Mater. Syst. Struct.*, vol. 21, no. 12, pp. 1147–1156, 2010.

[68] F. P. Incropera *et al.*, *Fundamentals of Heat and Mass Transfer*, 6th ed. Wiley, 2007.

[69] J. Cole *et al.*, “Active Thermal Management of FRP Composites via Embedded Vascular Networks,” in *ASME 2019 Conference on Smart Materials, Adaptive Structures and Intelligent Systems*, 2019.

[70] ASTM International, “ASTM D7264/D7264M-15 Standard Test Method for Flexural Properties of Polymer Matrix Composite Materials,” ASTM International, West Conshohocken, PA, 2015.

[71] Hexcel Corporation, “HexPly 8552 Data Sheet,” Hexcel Corporation.

[72] K. Marlett, “Hexcel 8552 IM7 unidirectional prepreg qualification material property data report,” National Institution for Aviation Research, Wichita, KS, 2011.

[73] T. K. Tsotsis *et al.*, “Aging of polymeric composite specimens for 5000 hours at elevated pressure and temperature,” *Compos. Sci. Technol.*, vol. 61, pp. 75–86, 2001.

[74] P. Musto *et al.*, “Thermal-oxidative degradation of epoxy and epoxy-bismaleimide networks: Kinetics and mechanism,” *Macromol. Chem. Phys.*, vol. 202, no. 18, pp. 3445–3458, 2001.

[75] J. Wolfrum *et al.*, “Approaches to understand and predict the influence of rapid heat-up on degradation and strength of carbon fibre polymer matrix composites,” *J. Compos. Mater.*, vol. 51, no. 17, pp. 2435–2447, 2017.

[76] E. Greenhalgh, *Failure Analysis and Fractography of Polymer Composites*. Elsevier, 2009.

[77] T. P. Skourlis and R. L. McCullough, “The effect of temperature on the behavior of the interphase in polymeric composites,” *Compos. Sci. Technol.*, vol. 49, no. 4, pp. 363–368, 1993.

[78] R. F. Minty *et al.*, “The influence of hardener-to-epoxy ratio on the interfacial strength in glass fibre reinforced epoxy composites,” *Compos. Part A Appl. Sci. Manuf.*, vol. 112, pp. 64–70, Sep. 2018.

[79] F. Meyer *et al.*, “The effect of stoichiometry and thermal history during cure on structure and properties of epoxy networks,” *Polymer (Guildf).*, vol. 36, no. 7, pp. 1407–1414, 1995.

[80] G. R. Palmese and R. L. McCullough, “Effect of epoxy–amine stoichiometry on cured resin

material properties," *J. Appl. Polym. Sci.*, vol. 46, no. 10, pp. 1863–1873, 1992.

[81] S. Pety, S; Tan, M; Najafi, A; Gendusa, A; Barnett, P; Geubelle, P; White, "Design of redundant microvascular cooling networks for blockage tolerance," *Appl. Therm. Eng.*, 2017.

[82] M. H. Y. Tan *et al.*, "Gradient-based design of actively-cooled microvascular composite panels," *Int. J. Heat Mass Transf.*, vol. 103, pp. 594–606, 2016.

[83] M. H. Y. Tan *et al.*, "Multi-objective design of microvascular panels for battery cooling applications," *Appl. Therm. Eng.*, vol. 135, no. November 2017, pp. 145–157, 2018.

[84] S. Soghrati *et al.*, "Computational modeling and design of actively-cooled microvascular materials," *Int. J. Heat Mass Transf.*, vol. 55, pp. 5309–5321, 2012.

[85] A. M. Aragón *et al.*, "Multi-physics design of microvascular materials for active cooling applications," *J. Comput. Phys.*, vol. 230, pp. 5178–5198, 2011.